

Sergiy Sukhorukov

# Ice-Ice and Ice-Steel Friction in Field and in Laboratory

Thesis for the degree of Philosophiae Doctor

Trondheim, November 2013

Norwegian University of Science and Technology  
Faculty of Natural Sciences and Technology  
Department of Civil and Transport Engineering



**NTNU – Trondheim**  
Norwegian University of  
Science and Technology



**NTNU**

Norwegian University of Science and Technology

Thesis for the degree of Philosophiae Doctor

Faculty of Natural Sciences and Technology  
Department of Civil and Transport Engineering

© Sergiy Sukhorukov

ISBN 978-82-471-4733-7 (printed ver.)  
ISBN 978-82-471-4734-4 (electronic ver.)  
ISSN 1503-8181

Doctoral theses at NTNU, 2013:300

Printed by NTNU-trykk

*To my parents*



## Abstract

Friction is one of the key phenomena during the interaction of ice with offshore structures and ships, ice rafting and ridging processes, and the brittle compressive failure of ice. Therefore, knowledge of the ice friction laws and a better understanding of this phenomenon are needed for the design of safe and reliable offshore structures and successful operations in ice-infested waters. This thesis presents experimental studies on ice friction in the field and in the laboratory and can be divided into three parts:

- field study of ice friction and the effects of different parameters on the kinetic and static friction coefficients;
- investigation of geometrical stick-slip interaction between ice and stainless steel in small-scale laboratory tests;
- field investigation of the vertical ice forces exerted on isolated vertical piles frozen in a level sea due to changes in the water level.

The first version of the experimental setup for the field tests to study ice friction was relatively simple and was used only in 2010. Significant modifications and improvements were made to the setup in 2011 that allowed us to better control the test conditions (i.e., velocity, normal load). The available range of sliding velocities (between  $6 \text{ mm s}^{-1}$  and  $43 \text{ mm s}^{-1}$ ) did not cover the whole range of our interest. Therefore, a new pulling mechanism was introduced in the tests in 2012 that allowed us to extend the sliding range up to  $110 \text{ mm s}^{-1}$ .

The field experiments were conducted with first year sea ice in the Barents Sea and in fjords at Spitsbergen during three springs (2010-2012). In September of 2012, the ice friction tests were performed with multiyear sea ice northeast of Greenland. Most of the tests were performed to investigate the friction between sea ice and sea ice, while the rest were to study the friction between sea ice and corroded steel. The aim of the study was to survey the most important factors that affect ice friction in field conditions and to determine whether the existing friction models correctly predict the dependences observed in the field tests. The effects of the sliding velocity ( $6 \text{ mm s}^{-1}$  to  $105 \text{ mm s}^{-1}$ ), air temperatures ( $-2^\circ\text{C}$  to  $-20^\circ\text{C}$ ), normal load (300 N to 2000 N), presence of sea water in the interface, and ice grain orientation with respect to the sliding direction on the friction coefficient were investigated. The effect of the hold time on the static friction coefficient was also studied. The test campaigns showed that ice surface roughness is likely to be the most important parameter in determining the friction coefficient. Repeated sliding over the same track led to surface polishing and decreased the kinetic friction coefficient from 0.48 to 0.05. When sliding occurs between unsmoothed surfaces, the friction coefficient was found to be independent of the sliding velocity. As the contacting surfaces become smoother, the kinetic friction coefficient begins to depend on the velocity, as predicted by existing ice friction models. Some attempts were made to characterise ice surface irregularities and real contact area using two techniques: 1) the production of an ice surface cast and its further analysis using an optical microscope and 2) measurements of the pressure distribution and real contact

area using tactile sensors. The static friction coefficient increases logarithmically with the hold time and changes from approximately 0.6 at 5 s to 1.26 at 960 s.

The small-scale laboratory studies on the stick-slip interaction between ice and stainless steel were performed at the University Centre in Svalbard (UNIS). A specially designed device allowed us to study the effect of well controlled steel surface roughness on the interaction between ice and steel under various test conditions. The effects of the relative sliding rate ( $1.67 \times 10^{-6} \text{ m s}^{-1}$  to  $0.83 \times 10^{-3} \text{ m s}^{-1}$ ), temperature ( $-5^\circ\text{C}$  to  $-25^\circ\text{C}$ ) and applied constant pushing force were also investigated. Stick-slip interaction was always observed in the tests on samples with an arithmetic average roughness ( $R_a$ ) between  $2 \text{ }\mu\text{m}$  and  $15 \text{ }\mu\text{m}$ . Both steady state sliding and stick-slip were observed in the tests on samples with the lowest ( $R_a = 2 \text{ }\mu\text{m}$ ) and the highest ( $R_a = 25.2 \text{ }\mu\text{m}$ ) roughness. The slip distance was found to be equal to the mean pitch profile (mean profile wavelength) for all velocities studied. The elasticity of the ice was found to be an important factor in the stick-slip interaction.

The field studies of the vertical ice forces exerted on isolated vertical piles frozen in the ice were performed in Svea, Spitsbergen, in March of 2010. Four different piles made of steel and aluminium were used in the experiments. The piles were pushed through the ice using a hydraulic jack. The first peak load measured in the tests is associated with the onset of the ice-pile relative movement. Because we always observed failure at or very near the ice-pile interface, the first peak load can be treated as the strength of adhesion or the cohesive failure of ice in the vicinity of the interface. Elastic plate theory was used to estimate theoretically the vertical forces exerted on a pile.

## **Preface**

This thesis is submitted to the Norwegian University of Science and Technology (NTNU) in partial fulfilment of the requirements for the degree of philosophiae doctor.

This doctoral work has been performed at the Department of Civil and Transport Engineering, NTNU, Trondheim, with Professor Sveinung Løset (NTNU) as the main supervisor and co-supervisor Professor Aleksey Marchenko (UNIS).

The experimental part of the work was performed at the Arctic Technology Department of the University Centre in Svalbard (UNIS). The working space for the test periods, necessary field equipment and safety instructions were kindly provided by UNIS.

The work was funded by NTNU and the Research Council of Norway. The work is a part of the SAMCoT and PetroArctic projects.





## Acknowledgements

I have arrived at the final destination of my four-year journey as a PhD student. My main motivations to start this PhD were curiosity and an interest in the Arctic, its beautiful nature and severe conditions. I wanted to expose myself to the difficulties and challenges that polar researchers and engineers meet in this fascinating part of the Earth. I was very lucky to have a job where I could combine work in the office with being out in the Arctic. I received unique educational opportunities: I worked in the Cold Lab at the University Centre in Svalbard (UNIS), participated in experiments at the Hamburg Ship Model Basin (HSVA), performed diverse tests with sea ice in fjords at Spitsbergen and, finally, was on board the R/V 'Lance' and the icebreaker 'ODEN' for scientific surveys to the Barents Sea and northeast Greenland. Such an intensive and interesting PhD journey would not have happened without financial support from the Research Council of Norway, the SAMCoT and PetroArctic projects. There are a number of persons I would like to express my gratitude to for making different contributions to this work.

First of all I would like to acknowledge my supervisor professor Sveinung Løset, who gave me such a brilliant opportunity to do a PhD in his group. I always felt his support, enthusiasm and encouragement during these four years. His help in planning experiments, assistance during field tests and ability to generate fruitful discussions are difficult to overestimate. Sveinung has been very kind and helpful in everyday life and made everything possible to make my life in Norway pleasant.

Another person without whom this thesis would not be possible is my co-supervisor professor Aleksey V. Marchenko. I am extremely grateful to Aleksey V. for inviting me to take courses in the University Centre in Svalbard in the autumn semester of 2006. Aleksey V. made a significant contribution to this thesis as a supervisor. It has been always helpful and enjoyable to discuss my work with Aleksey V., develop ideas he generated, and listen to his incredible stories.

I am sincerely grateful to professor emeritus Mauri Määttänen, who helped me enormously during my work on this thesis. Mauri helped me to create an experimental setup, took part in several tests at Spitsbergen, and made many useful comments and suggestions to improve the scientific quality of the thesis. Professor Knut Høyland spent a great deal of time with me discussing my work and made many useful comments. Knut, I would like to thank you for that. Many thanks also go to Dr Alex Klein-Paste for giving me a tremendous amount of useful advice, for fruitful and very interesting discussions and for his willingness to help.

Most of the time working on my PhD, I spent in a lovely place known as the 'PhD Basement'. The unique environment in the 'basement' has been discussed in a number of PhD theses produced by my former colleagues. Although I had to leave my office in the 'basement' and move 'upstairs' after my office was destroyed in September 2012, I was always a frequent guest in the 'basement'. The only reason for this is, of course, my good friends and colleagues: Anton and Sergey Kulyakhtin, Marat Kashafutdinov, Wenjun Lu, Ekaterina Kim, Ivan Metrikin, Johan Wählin, Felix Breitschädel, Wolfgang

Kampel, Raed Lubbad, Torodd Nord, Andrei Tsarau, Anna Pustogvar, Farzad Faridafshin, Marit Reiso, Hayo Hendrikse, Martin Storheim, Daniel Zwick, Arun Kamath, Ole-Christian Ekeberg, Christian Lønøy, Kenneth Eik, Ada Repetto, Nicolas Serre, Oddgeir Dalane, Vegar Aksnes, Hans Bihs, Jenny Trumars, Paul Thomassen, Eric van Buren, Michael Muskulus, Mayilvahanan Alagan Chella, Karl Merz and Fredrik Sanquist.

Marion Beentjes, Maria Azucena Gutierrez Gonzalez, Kjerstina Røhme, Elin Tønset, Daniel Erland and Sonja Marie Ekrann Hammer helped me a great deal in solving my problems and fulfilling all my needs. I am also grateful to professor emeritus associate professor Alf Tørum and Øivind Arntsen for interesting conversations during lunches.

My second home during my PhD study was Spitsbergen, and in total, I have spent approximately 11.5 months there. My time in Spitsbergen was always exciting because of its unique nature and people. I met many nice and kind persons with whom we hiked and made ski, boat and snow scooter trips. I thank my colleagues, friends and staff from UNIS: Aleksey Shestov, Anatoly Sinitsyn, Renat Yulmetov, Tatyana Drotikova, Lucie Strub-Klein, Nataliya Marchenko, Louis Delmas, Dmitry Brazhnikov, David Wrangborg, Pernilla Karlsson, Gunar Sand, Jomar Finseth, Joar Aspenes Justad, Kåre Johansen, Monica Votvik and Berit Jakobsen.

Separately, I would like to acknowledge the people who helped me to perform the field tests. They are Marat Kashafutdinov, Sergey Kulyakhtin, Aleksey Shestov, Guido Kuiper, Michel Kampffmeyer, Maxim Yazarov, Dmitriy Sharapov and students from the Arctic Technology department at UNIS.

I gained additional motivation to work on my research topic after a number of discussions with people from the ‘ice community’, whom I met at the IAHR and POAC conferences and during numerous workshops and meetings. I would like to acknowledge those people for helping to maintain my interest in this topic: Lasse Makkonen, Tuomo Kärnä, Ove Tobias Gudmestad, Robert Gagnon, Evgeny Karulin, Marina Karulina, Erland Schulson, Ben Lishman, Peter Sammonds, Kari Kolari, Jukka Heinonen, Per-Olav Moslet, Jukka Tuhkuri, Karl-Ulrich Evers, Evgenii G. Morozov and Sergi V. Muzylev.

I would like to thank all my friends from all over the world, my water polo team mates, the men with whom I sang in Store Norske Mannskor (Longyearbyen) and the dancers from the NTNUI ballroom dance group.

I am thankful to Olga for her care, understanding and patience during my last two years of work on this thesis.

Last, but not least, I would like to thank my family: my parents Boris and Tatyana, Dmitriy, Tima and Dar’ya. My parents encouraged me all the time, and I always felt their love, care, understanding and approval of all my decisions.

Sergiy Sukhorukov

September 2013, Trondheim, Norway

# Contents

<b>Abstract.....</b>	<b>i</b>
<b>Preface.....</b>	<b>iii</b>
<b>Acknowledgements .....</b>	<b>v</b>
<b>Contents .....</b>	<b>vii</b>
<b>List of Figures.....</b>	<b>ix</b>
<b>List of Tables .....</b>	<b>xiii</b>
<b>Nomenclature .....</b>	<b>xv</b>
<b>1. Introduction .....</b>	<b>1</b>
1.1 Motivation	1
1.2 Objectives and Scope	2
1.3 Research Approach	3
1.4 Structure of dissertation	4
1.5 Readership	4
1.6 List of Publications and Declaration of Authorship	6
1.6.1 Main Papers .....	6
1.6.2 Other papers.....	6
1.6.3 Declaration of Authorship: .....	7
<b>2 State-of-the-Art.....</b>	<b>9</b>
2.1 Definition and brief history of tribology	9
2.2 Ice friction	11
2.2.1 Ice friction models .....	11
2.2.2 Experimental setups to study ice friction .....	15
<b>3 Field investigation on the friction of sea ice against sea ice and steel.....</b>	<b>17</b>
3.1 Introduction	17
3.2 Development of the setup	18
3.3 Experimental procedure and test parameters	21
3.4 Results	25
3.4.1 Ice-ice friction.....	27
3.4.2 Ice-steel friction.....	37
3.5 Discussion	40
3.6 Investigations of the contact area and ice surface roughness	44
3.6.1 Introduction .....	44
3.6.2 Experimental methods .....	45
3.6.3 Results and discussion .....	48
3.7 Summary	52

<b>4</b>	<b>Geometrical stick-slip between ice and steel .....</b>	<b>55</b>
4.1	Introduction	55
4.2	Experimental setup and test procedure	56
4.3	Results and analysis	64
4.3.1	“Type I” tests .....	64
4.3.2	“Type II” tests.....	70
4.4	Mathematical model	73
4.5	Discussion	76
4.6	Summary	80
<b>5</b>	<b>Vertical action on a pile frozen in level ice due to water level changes .....</b>	<b>83</b>
5.1	Introduction	83
5.2	Field experiments on the vertical forces exerted on metal piles frozen in level sea ice due to water level change	84
5.2.1	Experimental setup and procedure .....	84
5.2.2	Results and analysis.....	87
5.2.3	Discussion.....	89
5.3	Calculation of the vertical forces	89
5.4	Concluding remarks	94
<b>6</b>	<b>Conclusions and recommendations for further work .....</b>	<b>95</b>
6.1	Field tests on the friction of sea ice against sea ice and steel	95
6.2	Geometrical stick-slip between ice and steel	97
6.3	Vertical action on a pile frozen in the level sea ice due to water level changes	98
	<b>References.....</b>	<b>101</b>

## List of Figures

Figure 1.1. (a) R/V Lance in the Barents Sea; (b) rubble field in the Barents Sea near Engeøya Island (20/04/2012); (c) ice bustles in the Svea coal harbour, Spitsbergen (2010). .....	2
Figure 2.1. Leonardo da Vinci sketches showing his experiments to determine 1) the friction torque on a roller and half bearing; 2) the force of friction on a horizontal plane, using a pulley; 3) the influence of the apparent contact area on the force of friction (Persson, 2000). .....	9
Figure 2.2. Coulomb's representation of rough surfaces (Dowson, 1998).....	10
Figure 3.1. Experimental setup used in 2010. ....	19
Figure 3.2. Experimental setup used in 2011. ....	19
Figure 3.3. Experimental setup used in 2012. ....	20
Figure 3.4. Experimental setup: (a) 2011 setup used in "dry" friction tests; (b) setup used in most of the tests in 2012; (c) and (d) are the side and top views, respectively, of the setup used to perform the "wet" friction tests.....	21
Figure 3.5. Thin sections of the first year sea ice used in the 2011 tests: (a) horizontal thin section of the top level of sea ice with granular structure; (b) horizontal thin section of the bottom level of the sea ice with columnar structure; (c) vertical thin section of the level ice from the transition zone, when ice changes its structure from granular to columnar.....	23
Figure 3.6. Ice block sliding directions in relation to the ice grain orientation. The different ice block sliding directions in relation to the ice grain orientation correspond to sliding configuration (a) bottom-top, (b) side(∥)-top, (c) side(⊥)- top, and (d) top-top. ....	24
Figure 3.7. Experimental arrangement for sliding on the edge of the ice block. Sliding occurred both along and perpendicular to the block edge.....	25
Figure 3.8. Temporal variations of the frictional force (steady sliding regime). The normal force was $F_n = 276.8$ N, the apparent contact area $S_a = 0.0714$ m <sup>2</sup> , the sliding velocity $v = 87.7$ mm s <sup>-1</sup> , $T_{air} = -2$ °C, $T_{track} = -2.9$ °C, and the ice block sliding surface temperature $T_{ice\ block} = -2.3$ °C. The bottom-top sliding configuration was used in the tests. ....	26
Figure 3.9. Temporal variations of the friction force in the friction tests (stick-slip regime). The normal force was 242.4 N, $S_a = 0.101$ m <sup>2</sup> , $v = 5.4$ mm s <sup>-1</sup> , the air temperature $T_{air} = -10.6$ °C, $T_{track} = -5.5$ °C, and $T_{ice\ block} = -4.4$ °C. The bottom-top sliding configuration was used in the tests. ....	26
Figure 3.10. Dependence of the kinetic friction coefficient on run number in tests with surface smoothening. The test parameters are listed in Table 3.1. Test sets Rs1, Rs2 and Rs4 were performed with ice in the Barents Sea. The test set Rs3 was performed in the Van Mijenfjord at Spitsbergen.....	28
Figure 3.11. Kinetic friction coefficient versus sliding velocity in tests with natural ice surfaces. Three test series were performed: (1) tests in the Van Mijenfjord at Spitsbergen (VM1 - VM6), (2) tests in the Barents Sea, Series 1 (S1BS1 – S1BS3), (3) tests in the Barents Sea, Series 2 (S2BS1 – S2BS4). The test parameters are listed in Table 3.2. ....	30

Figure 3.12. Kinetic friction coefficient versus sliding velocity (left figure) and run number (right figure) in the same set of tests. Markers with the same colour correspond to approximately equal sliding velocities. Test parameters:  $F_n = 208.5$  N,  $S_a = 0.088$  m<sup>2</sup>,  $T_{air} = -12.7^\circ\text{C}$ ,  $T_{track} = -3.9^\circ\text{C}$  and  $T_{ice\ block} = -5.7^\circ\text{C}$ . The bottom-top sliding configuration was used in the tests. .... 31

Figure 3.13. Kinetic friction versus sliding velocity for three sliding configurations in the “dry” friction tests. The normal loads and apparent contact area are  $F_n = 620$  N,  $S_a = 0.0765$  m<sup>2</sup> for the bottom-top sliding configuration, respectively;  $F_n = 620$  N and  $S_a = 0.0822$  m<sup>2</sup> for the side( $\perp$ )–top sliding configuration; and  $F_n = 560$  N and  $S_a = 0.0588$  m<sup>2</sup> for the side( $\parallel$ )–top sliding configuration. The tests were performed at an air temperature of  $T_{air} = -22^\circ\text{C}$ . The tests were performed in the Advent fjord in 2011. The velocity in the fit equation has units of mm s<sup>-1</sup>. .... 31

Figure 3.14. Kinetic friction coefficient versus air temperature in the “dry” and “wet” friction tests. The sliding velocity was  $40.9 \pm 2.6$  mm s<sup>-1</sup>.  $S_{app}$  was between 0.056 m<sup>2</sup> and 0.110 m<sup>2</sup>, and  $F_n$  was between 214 N and 568 N. .... 32

Figure 3.15. Kinetic friction coefficient versus ice track temperature in the “dry” and “wet” friction tests. The sliding velocity was  $40.9 \pm 2.6$  mm s<sup>-1</sup>.  $S_{app}$  was between 0.056 m<sup>2</sup> and 0.110 m<sup>2</sup>, and  $F_n$  was between 214 N and 568 N. .... 33

Figure 3.16. Test arrangements to study effect of normal load in “dry” and “wet” friction tests. .... 34

Figure 3.17. Kinetic and static friction forces versus normal load in the “dry” and “wet” friction tests. The experimental parameters are presented in Table 3.3. .... 35

Figure 3.18. Sliding on the edge of the ice block. Sliding along the ice block edge and perpendicular to it was studied.  $T_{air} = -14^\circ\text{C}$ , normal load  $F_n = 190.4$  N. Apparent contact area ( $S_a$ ) was 17.4 cm<sup>2</sup> after the tests with sliding  $\parallel$  to the edge, and 23.2 cm<sup>2</sup> after the tests with sliding  $\perp$  to the edge, respectively. .... 35

Figure 3.19. Static friction coefficient versus hold time. Four test sets were performed in “dry” conditions and one in “wet” conditions. To avoid overlap, the points on the time scale are displaced. .... 37

Figure 3.20. Test arrangement used in the friction test between steel and sea ice in “dry” conditions. .... 38

Figure 3.21. Test arrangement used in the friction test between steel and sea ice in “wet” conditions. .... 38

Figure 3.22. Kinetic friction force versus normal load in “wet” and “dry” ice-steel friction tests. The experimental parameters are listed in Table 3.5. .... 39

Figure 3.23. Static friction force versus normal load in “wet” and “dry” ice-steel friction tests. The experimental parameters are listed Table 3.5. .... 39

Figure 3.24. Tactile sensor 5027 and real contact area measurements in the field. .... 46

Figure 3.25. Real contact area measurements using sensor 5513. .... 46

Figure 3.26. Surface microscope to study steel surface and casts of the ice surfaces. ... 47

Figure 3.27. Replica of an ice surface during roughness measurements using an optical 3D surface microscope. .... 47

Figure 3.28. Pressure distribution in the contact between ice and flat rubber surface. The measurements were performed using tactile sensor 5513. .... 49

Figure 3.29. Pressure distribution in the contact between ice and flat rubber surface. The measurements were performed using tactile sensor 5027. .... 50

Figure 3.30. Applied normal load versus real contact area related to the apparent contact area ( $A_r/A_{app}$ ). The tests were performed at $T_{air} = -10^\circ\text{C}$ . The bottom surface of the ice block (i.e., the surface with the skeleton layer) was a contact surface and had the temperature $T_{ice\ surface} = -7.1^\circ\text{C}$ . The black arrows show the sequence of the data points obtained in the tests. ....	51
Figure 3.31. Image of the ice surface replica obtained using an optical 3D microscope. ....	52
Figure 4.1. (a) Sketch of the samples and bases used in the “ice slide tests” and “piston slide tests”; (b) piston and ice extracted from a hollow cylinder after completing the “piston slide test”.....	57
Figure 4.2. Portable surface roughness tester.....	58
Figure 4.3. Roughness measurements of stainless steel piston and inner surface of the hollow cylinder.....	58
Figure 4.4. Basic characteristics of the threading on the steel surfaces.....	59
Figure 4.5. Axial profiles of the inner cylinder and piston surfaces. Note the difference in the vertical scale of the cylinder and piston roughness profiles for sample Hr..	59
Figure 4.6. Uniaxial compression machine (KNEKKIS): (a) “ice slide test” and (b) “piston slide test”.....	61
Figure 4.7. Sample before being submerged in water.....	62
Figure 4.8. (a) Freshwater ice and (b) salty ice formation in the annulus between the piston and ice.....	62
Figure 4.9. Ice formation in the annulus between the hollow cylinder and a coaxially located steel piston.....	62
Figure 4.10. Samples containing salty ice after their extraction from the ice tank (left) and after the sawing process (right).....	63
Figure 4.11. Summary of the sample preparation procedure for the “piston slide tests” (using freshwater ice).....	63
Figure 4.12. Load versus displacement profiles obtained during the “ice slide tests” of the following samples: (a) Sr, (b) Mr and (c) Hr. The displacement rate and temperature were $1.67 \times 10^{-5} \text{ m s}^{-1}$ and $-15^\circ\text{C}$ , respectively. Samples with freshwater ice and salty ice ( $16.1 \pm 1.5 \text{ ppt}$ ) were used in the tests.....	65
Figure 4.13. Ice surface after testing of sample Mr filled with freshwater ice.....	66
Figure 4.14. Load versus displacement profiles obtained during the “piston slide tests” of the following samples: (a) Sr, (b) Mr, (c) Hr, (d) NHr and (e) TBr. The displacement rate and temperature in the tests performed on freshwater ice were $0.83 \times 10^{-4} \text{ m s}^{-1}$ and $-5^\circ\text{C}$ , respectively, and the displacement rate and temperature in the tests performed on salty ice were $0.66 \times 10^{-4} \text{ m s}^{-1}$ and $-10^\circ\text{C}$ , respectively. The salinity of the salty ice was 13.7 ppt.....	67
Figure 4.15. Samples after “piston slide tests”.....	68
Figure 4.16. Displacement of the piston corresponding to one period of load oscillation versus the displacement rate. The horizontal lines indicate the profile pitches $S_m$ measured with the profilometer.....	69
Figure 4.17. Load versus displacement profiles obtained from the piston slide tests. The displacement rate was $0.83 \times 10^{-4} \text{ m s}^{-1}$ , and the tests were performed at three different temperatures: $-25^\circ\text{C}$ , $-10^\circ\text{C}$ and $-5^\circ\text{C}$ .....	69

Figure 4.18. Temporal variations in the actual load and displacement during the “Type II” test on sample Hr: (a) entire data record and (b) data for the time period between 39 s and 57 s. The test temperature was $-15^{\circ}\text{C}$ , and $F_{\text{app}}/F_{1\text{st peak}} = 75\%$ .	70
Figure 4.19. Temporal variations in the actual load and displacement observed in the tests on sample NHr at different programmed loads $F_{\text{app}}/F_{1\text{st peak}}$ : (a) 25%; (b) 50%; (c) 75%; and (d) 90%. The test temperature was $-15^{\circ}\text{C}$ .	71
Figure 4.20. Onset time versus programmed (applied) load in tests of different samples. The tests were performed at $-15^{\circ}\text{C}$ .	72
Figure 4.21 Load versus displacement rate in the “Type II” tests on samples Mr and Hr. The test temperature was $-15^{\circ}\text{C}$ , and $F_{\text{app}}/F_{1\text{st peak}}$ was 50% and 75% in the tests on samples Mr and Hr, respectively.	72
Figure 4.22. Displacements measured in the “Type II” tests and simulated displacements versus time for samples Mr and Hr.	75
Figure 4.23. Scheme of the interaction between ice and steel asperities in an “ice slide test”.	77
Figure 5.1. Vertical pile frozen in the level ice: (a) ice sheet does not exert vertical force on the pile; (b) ice bent due to changing water level uplifting the pile.	83
Figure 5.2. Experimental setup to push a vertical pile frozen in level ice.	84
Figure 5.3. Pile pushed using a BHJ as a jack.	85
Figure 5.4. Ice piles used in the tests (left photo) and measurements of their roughness.	85
Figure 5.5. Temporal variations of vertical force and pile displacement in the second set of tests for piles no. 1, 3 and 4. Piles were pushed downwards using a BHJ.	88
Figure 5.6. Equivalent problem to the ice-pile interaction when the water level is changing.	90
Figure 5.7. Bending moments per unit length along the radial coordinate, $r$ .	92
Figure 5.8. Uplifting force on the pile at the initial failure at the ice-pile interface versus the pile radius for three ice thicknesses ( $h_{\text{ice}}$ ): 0.3 m, 0.5 m and 0.8 m.	93
Figure 5.9. Deflection of the ice plate at the failure initiated at the ice-pile interface versus pile radius for three ice thicknesses ( $h_{\text{ice}}$ ): 0.3 m, 0.5 m and 0.8 m.	93
Figure 5.10. Ice accretion on the vertical piles (left) and vertical walls (right).	94



## List of Tables

Table 3.1. Experimental parameters in the tests with surface smoothening due to repeated sliding over the same ice track.....	27
Table 3.2. Test parameters and static and kinetic friction coefficients. The effect of the velocity is studied when sliding occurs between natural (unsmoothed) surfaces. Each block slid on the corresponding ice track three times at a certain velocity. The average values from the three runs for the static and kinetic friction coefficients are given. ....	29
Table 3.3. Experimental parameters for the tests studying the effect of a normal load on the static and kinetic friction coefficients. The normal load ranged between 300 N and 2100 N. The bottom-top sliding configuration was used in these tests. ....	33
Table 3.4. Experimental conditions and obtained static friction coefficient in tests with hold times. ....	36
Table 3.5. Experimental parameters in ice-steel friction tests where the effect of the normal load on the static and kinetic friction coefficients was studied. The normal load ranged between 300 N and 2100 N.....	40
Table 3.6. Static and kinetic friction coefficients obtained in the ice-steel friction tests. Experimental parameters are listed in Table 3.5. ....	40
Table 3.7. Ice surface roughness measurements using optical 3D microscope and casts of the different ice surfaces. ....	51
Table 4.1. Roughness characteristics of the piston and inner cylinder surfaces: $S_m$ is the mean profile pitch (screw pitch); $R_z$ is the surface roughness depth (corresponding to the basic threading depth); and $R_a$ is the arithmetic mean surface roughness. The roughnesses were measured along the long axes of the cylinders and pistons. ....	60
Table 4.2. Summary of the “Type I” tests. ....	64
Table 4.3. Summary of the “Type II” tests.....	64
Table 4.4. Fit coefficients in the resistance formula (4.2) obtained from the “Type I” tests performed at a displacement rate of $0.167 \text{ mm s}^{-1}$ . The tests were carried out at $-18^\circ\text{C}$ . $\langle F \rangle_I$ is the mean force during the entire test. ....	74
Table 4.5. Fit coefficients in the force – displacement rate dependence obtained in the “Type II” tests. The tests were performed at $-15^\circ\text{C}$ . $\langle v \rangle$ and $\langle F \rangle_{II}$ are the mean displacement rate and force during the second phase of the “Type II” tests, respectively.....	75
Table 4.6. Upper limits of the contact pressure ( $p_{\max}$ ) between the ice and steel asperities and corresponding contact areas ( $S_{\text{cont}}$ ) in the “ice slide” and “piston slide” tests performed on samples Sr, Mr and Hr.....	78
Table 5.1. Shape, dimensions and surface roughness of the piles used in the tests. ....	86
Table 5.2. Peaks forces measured in the first set of experiments. In the table “Pressure” is the pressure in the jack.....	87
Table 5.3. Comparison of the results obtained in the two different sets of tests. The first set was performed after the piles had been exposed to freezing in the level ice during 44 hours. In the second set of tests, the freezing time was around one week	

(173 hours). The air temperature during this period was consistently below  $-10^{\circ}\text{C}$ .

..... 89

Table 5.4. Values for the parameters used to estimate bending moments..... 92

## Nomenclature

$A$	constant
$A_{app}$	apparent contact area
$A_{dry}, A_{wet}$	dry and wet part of the apparent contact area
$A_r$	apparent contact area
$A, B$	constitutive parameters
$B$	function of thermal conductivity, contact dimensions and thermal diffusivity of ice
$b$	contact length
$C$	constant
$c_1, c_2$	specific heat capacity of ice and slider material
$D$	contact spot diameter
$d_{cyl}$	inner diameter of the hollow cylinder
$D_c$	critical slip distance
$E$	Young's modulus
$F_n$	normal load
$F_f$	static or kinetic friction force
$F_0$	constant that sometimes is called initial cohesion force
$F_x$	pushing force
$\langle F \rangle_I$	mean force during the entire "Type I" test
$\langle F \rangle_{II}$	mean force during the second phase of the "Type II" test
$h$	latent heat of melting for ice
$h_{wef}$	water film thickness
$H_1$	indentation hardness of ice
$k$	thermal conductivity of the slider
$l$	volumetric latent heat of fusion for ice
$L$	sintering factor
$M_r, M_\theta$	bending moments of the ice plate
$m$	piston/ice mass
$n$	number of contact points
$P$	contact pressure
$Q$	cutting force
$p, q$	numerical constants that are specified by the physical working mechanisms of ice sintering
$p_1$	fit parameter
$q_1, q_2$	fit parameters
$r$	radius of the contact area of the asperities
$R$	radius of the asperities
$R$	pile radius
$R_1, R_2$	radii of the cylinders

$R_I, R_{II}$	resistance in “Type I” and “Type II” tests, respectively
$R_a$	arithmetic mean surface roughness
$R_z$	surface roughness depth
$S_a$	apparent contact area
$T_0$	ambient temperature
$T_m$	melting point temperature of the ice appropriate to the pressure
$T_f$	softening temperature of ice
$T_a$	temperature of approaching track
$\Delta T_1, \Delta T_2$	temperature differences
$v, V_s$	sliding velocity
$\langle v \rangle$	mean displacement rate
$V_s^*$	normalising constant
$w$	half width of the constant
$\delta_n$	relative displacement of the cylinders
$\eta_0, \eta$	viscosity of water
$\theta$	state variable
$\lambda_1, \lambda_2$	thermal conductivity of ice and slider
$\mu$	kinetic coefficient of friction
$\mu_0$	nominal coefficient of friction
$\mu_t$	true friction coefficient
$\mu_m$	contribution to the friction coefficient due to the energy required to melt the ice surface layer
$\mu_{dry}$	friction coefficient in dry friction tests
$\mu_{st}$	static friction coefficient
$\nu$	Poisson’s ration
$\rho_0$	water density
$\rho_1, \rho_2$	ice and thermal material density
$\sigma$	compressive strength of ice
$\sigma_0$	real contact pressure
$\sigma_f$	flexural strength of ice
$\tau$	shear strength of ice

# Chapter 1

## 1. Introduction

### 1.1 Motivation

The growing interest in the exploration and production of hydrocarbons in cold regions and the intention and willingness to use shorter sea routes that go through the Arctic all dictate new challenges for engineers. Among many problems for the platform and drilling ship operations, such as cold weather, heavy wind, waves and remoteness, the engineers must also address ice actions. According to Løset et al. (2006), the entire lifespan of structures in the Arctic (i.e., stability, strength and serviceability) depends on ice-structure interaction. Underestimating the ice action may lead to collapse of the structure and ecological disaster. Thus, knowledge of the properties of sea ice and understanding of the different physical processes occurring during ice-structure interaction are vital for the development of safe and sustainable technologies for hydrocarbon production in cold waters.

Figure 1.1 shows R/V Lance in first year sea ice and two examples of ice features that are encountered in cold regions: ice ridges and ice bustles, formed around structure piles in areas with high water level fluctuations.

Ice friction is one of the key phenomena in ice-structure interactions and plays an important role in a number of engineering applications. It affects the performance of icebreakers in ice-covered waters (Ionov and Gramuzov, 2001; Liukkonen, 1988; Valanto, 2001). Knowing the sea ice friction on different materials (including sea ice) is necessary for calculating the ice loads on sloping offshore structures (Croasdale and Cammaert, 1994; Palmer and Croasdale, 2013; Tikanmäki et al., 2011). According to Schulson and Duval (2009), friction is a fundamental process during the brittle compressive deformation of cold ice. Friction is the largest sink of energy during the rafting and ridging processes of sea ice. Therefore, the results of the numerical simulations describing these processes are affected by the choice of input for the friction coefficient (Hopkins et al., 1991; Hopkins and Tuhkuri, 1999; Marchenko and Makshtas, 2005; Paavilainen et al., 2011; Polojärvi and Tuhkuri, 2013). The formation of ice bustles around piles (Figure 1.1(c)) imposes additional gravitational actions on the structure, increases the effective diameter of the pile, and may be a potential threat to the safety of the structure (Løset and Marchenko, 2009). ISO 19906 (2010) emphasises the importance of friction when ice is acting on sloping and conical structures, as in ice ridging and the interaction of with a hull. However, there is little information about friction coefficient values and the effect of different parameters. ISO 19906 (2010) does not propose any friction model that takes into account the effects of different parameters on the static and kinetic friction coefficients.

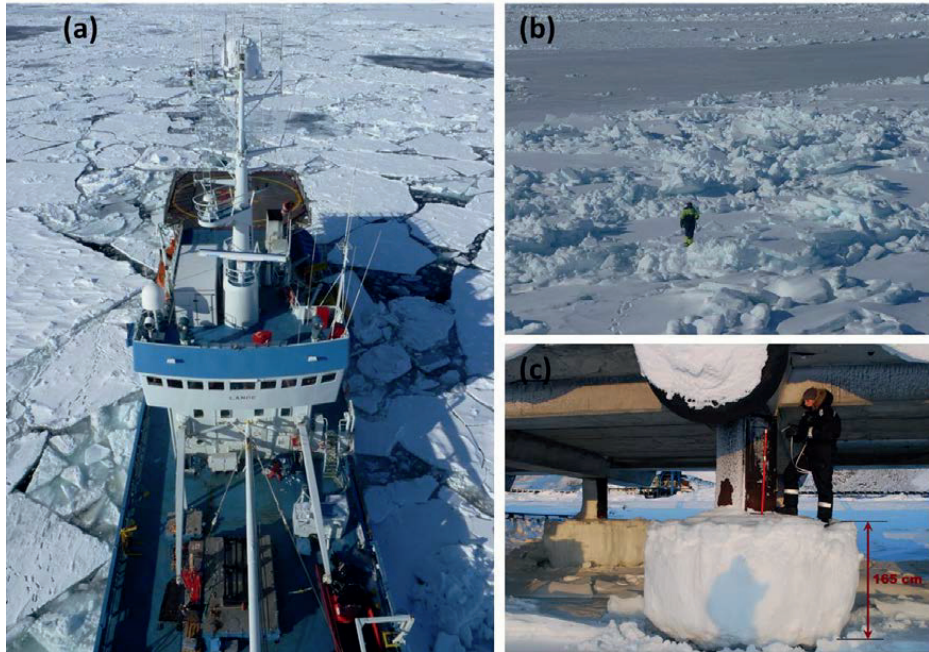


Figure 1.1. (a) R/V Lance in the Barents Sea; (b) rubble field in the Barents Sea near Engeøya Island (20/04/2012); (c) ice bustles in the Svea coal harbour, Spitsbergen (2010).

Despite the importance of ice friction in many engineering and scientific applications, it is still not well studied and remains poorly understood. The majority of the ice friction studies have been performed in small-scale laboratory tests. According to a survey of the literature, the existing frictional models (Akkok et al., 1987; Evans et al., 1976; Makkonen and Tikanmaki, 2013; Oksanen and Keinonen, 1982) were validated only using lab data. Nevertheless, from the engineering point of view, it is important to know how well the friction models capture the main dependences on external parameters (temperature, velocity, normal load, presence of sea water) observed in real field conditions. Some data were obtained in past field friction tests by Ryvlin (1973), Gavrilov (1984) and Pritchard et al. (2012). More field data are needed for further development of the ice friction model.

## 1.2 Objectives and Scope

The main intent of the present thesis has been to gain increased knowledge about ice friction. The work presented in the thesis can be divided into three parts. In the first part, the friction between sea ice sliding against itself and corroded steel was studied in field tests. The effects of different parameters on the kinetic and static friction coefficients were investigated. The second part is devoted to the study of the stick-slip interaction between ice and stainless steel in small-scale laboratory tests. The effect of surface roughness on this interaction was the main focus. The third part is devoted to

the field study of the vertical ice forces exerted on isolated vertical piles frozen in level sea ice. The objectives of the thesis were to do the following:

- investigate the friction of sea ice on sea ice and of sea ice on steel in field conditions;
- identify and quantify the most important parameters that affect the friction coefficients;
- compare the results with the predictions made by existing ice friction models, and determine their limitations;
- investigate the effect of steel surface roughness on the stick-slip interaction between ice and steel in laboratory tests;
- study in field conditions the vertical action due to water level changes of sea ice on an isolated vertical pile frozen in the ice.

### 1.3 Research Approach

The work presented in the thesis is mainly experimental and consists of three parts. The first part is the investigation of the friction of sea ice against itself and corroded steel in field conditions. The effects of the velocity, normal load, air temperature, presence of sea water in the sliding interface, and ice grain orientation with respect to the sliding direction on the friction coefficient were investigated. The experiments were conducted in the Barents Sea and the fjords at Spitsbergen. The experimental setup was designed and then significantly improved during three consequent field seasons (2010-2012). The initial version of the setup was similar to the experimental setups used by Ryvlin (1973), Gavrilov (1984) and Pritchard et al. (2012). In the final version of our setup, a stiff pulling rod (actuator) was used to tow an ice block, in contrast to elastic cables used by other authors. The values and dependences obtained for the kinetic and static friction coefficients were analysed, discussed and compared with previous works and the existing ice friction models in the literature (Akkok et al., 1987; Evans et al., 1976; Oksanen and Keinonen, 1982). The main limitation of the study is that sufficiently flat snow-free level ice was used in the tests.

The second part is devoted to the investigation of the stick-slip interaction between ice and stainless steel with regular surface roughness. The experimental setup was initially developed by Nanetti et al. (2008) and modified by the author. The tests were performed in the Cold Lab at UNIS. A special geometry of the testing samples allowed us to use a compression rig to initiate and maintain the relative sliding between the ice and the steel surface, recording the temporal variations in load and displacement. A detailed analysis of the experimental data was performed. The pressure concentration between the ice and steel surface asperities was estimated based on the Hertz contact problem. It was assumed that the ice and steel asperities deform elastically during their interaction. This assumption is supported by visual observations of the ice surface after the test.

The third part is devoted to a field study on the vertical forces exerted on isolated vertical piles frozen in level sea ice. The tests were performed in Svea, Spitsbergen in

March of 2010. Four different piles made of steel and aluminium with different diameters were used in the experiments. The piles were pushed through the ice using a hydraulic jack. The first peak load measured in the tests is associated with the onset of the relative movement in the ice-pile interface. Because we always observed failure at the interface, the first peak load can be treated as the strength of adhesion. Elastic plate theory was used to calculate the maximum vertical force acting on the pile. The pile in the calculations was treated as an absolutely rigid body.

## 1.4 Structure of dissertation

The thesis consists of an Introduction (Chapter 1) and five further Chapters (2 - 6).

Chapter 1, the motivation of the work and the objectives, scope, research approach and contributions are presented.

Chapter 2 presents state-of-the-art of ice friction problems. It gives short history of tribology in general, experimental methods, existing friction theories and ice friction models.

Chapter 3 outlines the development of the setup and the test results, analysis and discussion of the field study on the friction of sea ice against itself and against corroded steel. The effects of the different parameters that influence the kinetic and static friction coefficients are discussed in detail. A comparison with previous studies is made. The ice roughness, real contact area and pressure distribution in the contact are investigated.

Chapter 4 describes the results and analysis of the small-scale laboratory tests on the stick-slip interaction between ice and stainless steel. The effects of surface roughness, temperature, applied force and displacement rate on the ice-steel interaction are discussed. The analysis allowed us to find the dependence between the friction force and the displacement rate. The Hertz contact problem was used to determine the local contact pressure between the ice and steel surface asperities.

Chapter 5 presents the results and analysis of the field experiments on the vertical ice forces exerted on isolated vertical piles frozen in level sea ice due to water level changes. Elastic plate theory is used for the theoretical calculation of the maximum vertical force exerted on the piles.

Finally, Chapter 6 concludes the study and makes recommendations for further work within the field of ice friction against ice and steel.

## 1.5 Readership

The thesis presents the results from the field studies on the friction of sea ice on sea ice and on corroded steel together with a laboratory study on the geometrical stick-slip interaction between ice and stainless steel. The primary readership of this thesis is as follows:



- Engineers and researchers interested in or working with sea ice related problems, especially ice-structure interaction, modelling ridging and rafting processes and ship performance in ice infested waters;
- Students and teachers dealing with sea ice. For instance, the thesis may serve as part of the syllabus in a university course such as *Arctic Offshore Engineering* or *Ice Mechanics*.

## **1.6 List of Publications and Declaration of Authorship**

### **1.6.1 Main Papers**

#### **Paper I**

Sukhorukov, S. and Løset, S., 2013. Friction of sea ice on sea ice. *Cold Regions Science and Technology*, 94 (2013): 1-12.

#### **Paper II**

Sukhorukov, S. and Løset, S., 2011. Field experiments on ice-ice friction, *Proceedings of the 21st International Conference on Port and Ocean Engineering under Arctic Conditions*, Montreal, Canada, POAC11-008.

#### **Paper III**

Sukhorukov, S., Määttänen, M. and Løset, S., 2012. Field experiments on the friction coefficient of sea ice on sea ice, *Proceedings of the 21st IAHR International symposium on ice*, Dalian, China, pp. 65-77.

#### **Paper IV**

Sukhorukov, S. and Marchenko, A., 2013. Geometrical stick-slip between ice and steel, *Cold Regions Science and Technology* (*submitted*).

#### **Paper V**

Sukhorukov, S. and Marchenko, A., 2009. Stick-slip interaction of ice with steel surfaces, *Proceedings of the 20th International Conference on Port and Ocean Engineering under Arctic Conditions*, Luleå, Sweden, POAC09-70.

### **1.6.2 Other papers**

The author was also involved in other studies that were published, but not directly related to the topics discussed in the current thesis and therefore, the material form these papers was not included in the thesis.

#### **Paper VI.**

Marchenko, A., Thiel, T. and Sukhorukov, S., 2012. Measurements of thermally induced deformations in saline ice with fiber bragg grating sensors, *Proceedings of the 21st IAHR International Symposium on Ice*, Dalian, China, pp. 651-659.

#### **Paper VII.**

Määttänen, M., Løset, S., Metrikine, A., Evers, K.-U., Hendrikse, H., Lønøy, C., Metrikin, I., Nord, T. and Sukhorukov, S., 2012. Novel ice induced vibration testing in large-scale facility: Deciphering ice induced vibrations, Part 1, *Proceedings of the 21st IAHR International Symposium on Ice*, Dalian, China, pp. 946-958.

### 1.6.3 Declaration of Authorship:

**Paper I. (Sukhorukov and Løset, 2013).** I am responsible for the entire work in the paper. S. Løset helped to perform the tests, made relevant recommendations and comments during the paper writing process.

**Paper II. (Sukhorukov and Løset, 2011).** I initiated the ideas to study ice friction under field conditions. The setup was designed together with S. Løset. I developed test procedure and experimental programme, performed data analysis and wrote the paper. S. Løset gave useful advices and made minor corrections in the final paper.

**Paper III. (Sukhorukov, Määttänen, Løset, 2012).** I was actively involved in the setup design and developed the test procedure. The tests, data analysis and paper writing were performed by me. M. Määttänen and S. Løset participated in the setup development, helped to perform minor part of the tests and made useful comments to increase scientific quality of the paper. M. Määttänen also proposed the tests where sliding occurred on the edge of the ice block.

**Paper IV. (Sukhorukov and Marchenko, 2013).** I modified the setup and test procedure, developed earlier by M. Nanneti. I suggested and performed new tests at a constant displacement rate and constant applied load, analysed the data, performed all calculations and wrote the paper. My co-author Aleksey Marchenko gave valuable advices about data analysis, suggested to use Hertz contact problem to estimate normal pressure in the ice-steel interface and made useful comments to improve scientific quality of the paper.

**Paper V. (Sukhorukov and Marchenko, 2009).** I performed the tests, analysed the data, made pressure calculations based on the Hertz contact problem and wrote the paper. A. Marchenko suggested a method to calculate local pressure in the ice-steel interface and contributed to the paper writing.



# Chapter 2

## 2 State-of-the-Art

### 2.1 Definition and brief history of tribology

According to Persson (2000), tribology is the science and technology of interacting solid surfaces in relative motion. The word *tribology* derives from Greek root τριβω (“I rub”) and suffix λόγια (“study of”). The topics covered by this word include friction, lubrication and wear (Persson, 2000).

An extensive history of tribology is presented in the book Dowson (1998). Here, we present a very brief historical note on this topic starting from the late 1400s.

Leonardo da Vinci (1452-1519) produced the first recorded systematic experimental studies of friction, wear and bearings. Figure 2.1 shows some of Leonardo’s sketches demonstrating his studies on friction and bearings.

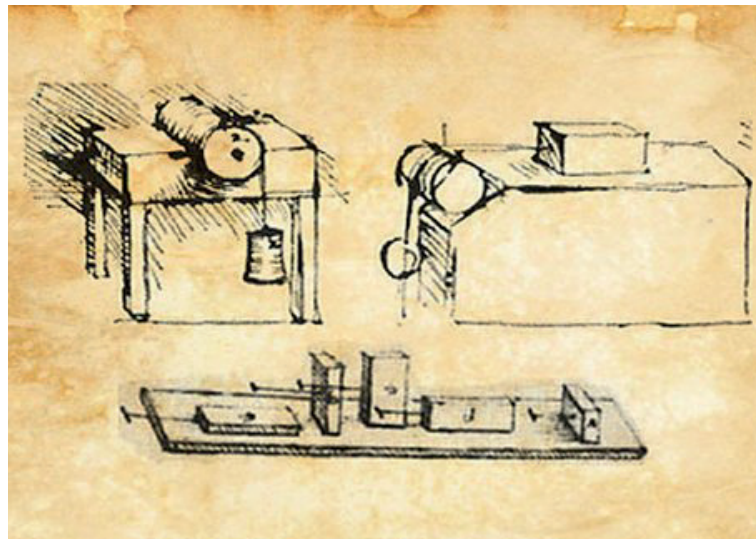


Figure 2.1. Leonardo da Vinci sketches showing his experiments to determine 1) the friction torque on a roller and half bearing; 2) the force of friction on a horizontal plane, using a pulley; 3) the influence of the apparent contact area on the force of friction (Persson, 2000).

Da Vinci was the first to state two basic laws of friction, 200 years before Isaac Newton defined the term *force*. Leonardo da Vinci wrote (Persson, 2000):

- “The friction made by the same weight will be of equal resistance at the beginning of its movement, although the contact may be of different breadth and length”;
- “Friction produces double the amount of effort if the weight be doubled.”

According to Persson (2000), Leonardo also introduced the coefficient of friction as the ratio between the friction force and the normal force (load). For polished and smooth surfaces, he concluded that “every friction body has a resistance of friction equal to one-quarter of its weight.”

Guillaume Amonton (1663-1705) rediscovered the frictional laws first discovered by Leonardo da Vinci. Leonhard Euler (1707-1783) introduced a mathematical method of approaching the law of dry friction (Popov, 2010). Euler believed that friction originates from the interlocking of triangular irregularities, was the first to distinguish between static and kinetic friction and introduced symbol  $\mu$  for the friction coefficient.

Charles August Coulomb (1736-1806) made a comprehensive study of friction and investigated the influence of five main factors on friction (Persson, 2000): a) the nature of the materials in contact and their surface coatings; b) the extent of the surface area; c) the normal pressure (or force); d) the length of time that the surfaces remained in stationary contact; e) ambient conditions such as temperature, humidity, and even vacuum. Coulomb considered that contacting surfaces are covered by flexible, elastic fibres that are similar to the hairs on a brush (Figure 2.2).

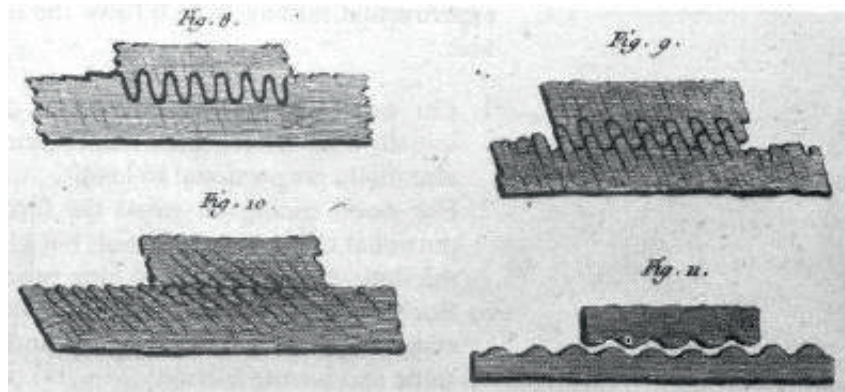


Figure 2.2. Coulomb’s representation of rough surfaces (Dowson, 1998).

Coulomb summarised most of his results in the friction law known as the Amonton-Coulomb law

$$F = \mu L, \quad (2.1)$$

where  $F$  is the friction force;  $L$  is the normal force; and the friction coefficient  $\mu$  is

usually nearly independent of the normal force and of the sliding velocity (as long as it is not too high or too low).

F. P. Bowden and D. Tabor (approximately 1940) gave a physical explanation for the frictional laws. They noted that because of surface roughness, there is a significant difference between the apparent and the real contact area. The real contact area increases as the normal force increases, as more asperities come into contact and the average area of each asperity contact grows. Bowden and Tabor stated that the real area alone determines the magnitude of the friction force.

Makkonen (2012) proposed a new thermodynamic model of sliding friction. His theory is based on the thermodynamic surface energy per unit area and refers to the excess energy of a surface with respect to an atomically complete contact. The author considered the growth and disappearance of the real nanoscale contacts. Makkonen (2012) obtained the following final expression for the friction coefficient:

$$\mu = \frac{\gamma_1 + \gamma_2 - \gamma_{1,2}}{2dH}, \quad (2.2)$$

where  $\gamma_1$  and  $\gamma_2$  are the surface energies of solid 1 and solid 2, respectively;  $\gamma_{1,2}$  is the surface energy for the solid 1-solid 2 interface;  $d$  is the characteristic length of the real contact; and  $H$  is the indentation hardness of the softer material.

Significant contributions to the understanding of the friction and wear were also made by Kragelsky (1968) and Rabinowicz (1995). With the development of the first atomic force microscope (AFM) in 1986, scientists obtained a unique tool to study friction and better understand the basic mechanics of friction at the atomic scale. However, the mechanisms of friction at the macroscopic scale are not well understood and still need to be studied. The development of supercomputers allowed simulations of realistic sliding systems (Persson, 2000). The most recent achievement in contact mechanics and friction was described in the book by Popov (2010).

## 2.2 Ice friction

It is well known that skiing and skating are possible and enjoyable because of the unusually small friction coefficient. The pressure melting theory was once commonly accepted as the explanation for skiing and skating. It was assumed that the force exerted by a skate or ski on the ice beneath it causes a depression of the equilibrium melting-point of the ice, thereby producing local surface melting (Hobbs, 2010). The thin melt water layer was considered as a lubricant. Bowden and Hughes (1939), using the Clausius-Clapeyron equations, showed the inadequacy of this earlier theory. The authors also proposed that the lubricating liquid was produced as a result of heating due to the work dissipated by the friction in the interface.

### 2.2.1 Ice friction models

Ice friction is a very complex process, and different friction regimes may occur depending on the properties of the sliding materials and test parameters (Kennedy et al., 2000; Kietzig et al., 2010). Therefore, there is no universal model that satisfactorily

describes ice friction under all possible conditions. We will briefly present several existing ice friction models.

Evans et al. (1976) quantitatively developed a frictional heating theory proposed by Bowden and Hughes (1939). It was assumed that the heat produced by friction raises the temperature of the ice surface to its melting point and produces a small amount of water that lubricates the contact area. The largest amount of the frictional heat is conducted from the contact area into the slider and ice. Evans et al. (1976) calculated the dependence of the friction coefficient on the thermal conductivity of the slider, ambient temperature, and sliding velocity. They derived the following expression for the friction coefficient:

$$\mu = \frac{Ak(T_m - T_0)}{F_n v} + \frac{B(T_m - T_0)}{F_n v^{0.5}} + \mu_m, \quad (2.3)$$

where  $A$  is a constant that depends on the size of the contact area, geometry, and nature of the slider surface;  $k$  is the thermal conductivity of the slider;  $T_0$  and  $T_m$  are the ambient temperature and melting point temperature appropriate to the pressure, respectively;  $F_n$  is the normal load;  $v$  is the sliding velocity; and  $B$  is defined as a function of  $k$ , dimensions of rectangular contact and thermal diffusivity of ice. The last term in Eq.(2.3),  $\mu_m$ , is the contribution of the friction coefficient due to the energy required to melt the ice surface layer. The authors estimated the maximum value of  $\mu_m$  as 0.005 and concluded that this parameter makes a fairly small contribution to the total friction coefficient over much of the range of velocities.

Oksanen and Keinonen (1982) expanded upon the theory of Evans et al. (1976); specifically, they calculated the friction coefficient by assuming that the water layer formed by frictional heating was the only cause of friction. The frictional force was caused by viscous shear in a water layer between two materials. Transient heat conduction into the ice and slider was also assumed. The authors established the following final expression for the friction coefficient:

$$\mu = n^{1/4} H_1^{-3/4} F_n^{-1/4} \left\{ \frac{1}{2} \frac{1}{(2v)^{1/2}} \left[ \Delta T_1 (\lambda_1 c_1 \rho_1)^{1/2} + \Delta T_2 (\lambda_2 c_2 \rho_2)^{1/2} \right] + \left[ \frac{1}{8v} \left( \Delta T_1 (\lambda_1 c_1 \rho_1)^{1/2} + \Delta T_2 (\lambda_2 c_2 \rho_2)^{1/2} \right)^2 + \eta_0 v h \rho_0 \right]^{1/2} \right\}, \quad (2.4)$$

where  $n$  is a number of contact points,  $H_1$  can be interpreted as the indentation hardness of ice,  $\eta_0$  is the viscosity of water,  $h$  is the latent heat of melting for ice,  $\rho_0$  is the water density,  $\lambda$  is the coefficient of thermal conductivity,  $c$  is the specific heat capacity,  $\rho$  is the density, and  $\Delta T$  is the temperature difference between the contact surface and bulk solid. Subscripts 1 and 2 refer to the ice and sliding material, respectively. Oksanen and Keinonen (1982) distinguished two temperature regions with distinct frictional behaviours. When the temperature difference  $\Delta T_1$ (ice) is large, the heat conduction term



is dominant over the viscous shear and the last term in Eq. (2.4) can be omitted. The same result is obtained for the zero water layer thickness. This result indicates that the generated frictional heat is mostly conducted in between the two solids and plays a negligible part in melting the ice. In this case, the friction coefficient is proportional to  $v^{-0.5}$ . When the temperature differences  $\Delta T_1$  and  $\Delta T_2$  are small, the viscous shear term is dominant, suggesting that the available frictional heat melts the ice. In this case, the friction coefficient is proportional to  $v^{0.5}$ . Tikanmäki et al. (2011) and Makkonen and Tikanmäki (2013) further developed this friction model taking into account depression of the equilibrium phase change temperature due to pressure, dependence of ice hardness on the temperature and squeeze-out of melt water film.

Akkok et al. (1987) proposed a model in which the softening temperature of ice is used as an upper bound for the surface temperature instead of the melting temperature. When the ice reaches the softening temperature, the contacting surface is easily abraded and removed by shear. Therefore, the authors assumed that all energy is conducted into the ice and slider and that no energy is consumed to melt the ice. Akkok et al. (1987) derived the following equation for the friction coefficient:

$$\mu = C \frac{(T_f - T_a)}{P} \left( \frac{k \rho c}{vb} \right)^{1/2}, \quad (2.5)$$

where  $b$  is the contact length,  $P$  is the contact pressure,  $C$  is a constant,  $T_f$  is the softening temperature of the ice, and  $T_a$  is the temperature of the approaching track.

Baurle et al. (2007) described a numerical model for polyethylene sliding on ice and snow for their tribometer experiments. In their model, the generated friction heat is dissipated by a combination of several mechanisms: dry friction, heat conduction, phase changes, shearing of water films, and the squeeze out. The total friction force was calculated using the following formula:

$$F_f = \mu_{dry} \cdot F_n \cdot \frac{A_{dry}}{A_{app}} + \frac{\eta \cdot v \cdot A_{real}}{h_{wf}} \cdot \left( 1 - \frac{A_{dry}}{A_{app}} \right), \quad (2.6)$$

where  $\mu_{dry}$  is the friction coefficient in dry friction tests (a constant value of 0.3 was used),  $A_{dry} = 1 - A_{wet}$  is the part of the apparent area ( $A_{app}$ ) where dry friction is predominant,  $h_{wf}$  is the water film thickness,  $\eta$  is the water viscosity,  $F_n$  is the normal load, and  $v$  is the sliding velocity. The water film in the sliding interface is governed by

$$\frac{\partial h_{wf}}{\partial t} = \frac{1}{l} \left( \frac{\eta \cdot v^2}{h_{wf}} - \lambda \cdot \partial_z T \Big|_{z=0} \right) - \frac{8 \cdot h_{wf}^3 \cdot \sigma_0}{3 \cdot \eta \cdot D^2}, \quad (2.7)$$

where  $l$  is the volumetric latent heat of fusion,  $\lambda$  is the thermal conductivity, and  $\partial_z T \Big|_{z=0}$  represents the average temperature gradient at the interface. The last term in Eq. (2.7) considers the squeeze of the lubricating water, where  $D$  and  $\sigma_0$  are the contact

spot diameter and normal pressure, respectively. The basis for the model was a one-dimensional model of heat generation at the interface and heat flow into the slider and ice. The changing conditions in the direction of the sliding (changing film thickness and real contact area) were considered by performing several calculations along the slider. The authors used experimental data to extend the model and reproduce dependencies of the friction coefficient on the temperature and load. They noted that the calculation is very sensitive to the input parameters, such as ice roughness and contact diameter.

Maeno and Arakawa (2004) formulated a new theory of ice friction at very low sliding velocities ( $< 10^{-6} \text{ m s}^{-1}$ ) by improving the traditional adhesion theory of Tabor (1959). The authors considered the effect of junction growth by ice sintering. According to their theory the ice-ice friction coefficient is expressed as

$$\mu = L \frac{\tau}{\sigma}, \quad (2.8)$$

where  $\tau$  and  $\sigma$  are the shear and compressive strengths of ice at the interface, respectively, and  $L$  is a constant called the sintering factor for ice friction.

$$L = \left[ 1 + 2C \left( \frac{r}{R} \right)^{1-q} \frac{R^{1-p}}{v} \right]^{2/q}, \quad (2.9)$$

where  $C$  is a constant that depends on the temperature,  $p$  and  $q$  are numerical constants specified by the physical working mechanisms of ice sintering,  $r$  is the radius of the contact area of the asperities,  $R$  is the radius of the asperities (it was assumed that all asperities have a spherical shape and the same radius), and  $v$  is the sliding velocity. Calculations showed that  $L$  becomes significant at temperatures above  $-20^\circ\text{C}$ .

All of the friction models presented above require that the real contact area and the amount, distribution, and size of the contact spots are known. Direct measurements of these parameters are problematic and, in most cases, impossible. These factors do greatly influence the results and are used as turning parameters in most models to fit the model with experimental data. The existing models do not consider the effect of ploughing, which is a significant contributor to the frictional resistance.

Another approach to model ice friction was proposed by Fortt and Schulson (2009) and Lishman et al. (2011). The authors focused on the sliding process in which the velocity and state change with time, similar to what occurs in the Arctic environment during the interaction of ice floes. Fortt and Schulson (2009) and Lishman et al. (2011) suggested using friction models and tests proposed earlier in rock mechanics (Gu et al., 1984; Ruina, 1983). Fortt and Schulson (2009) performed experiments in which the sliding velocity was “instantaneously” changed once the friction coefficient reached a steady-state value. The authors used the following phenomenological relationship to describe the friction coefficient:

$$\mu = \mu_0 + A \ln \left( \frac{V_s}{V_s^*} \right) + B \ln \left( \frac{V_s^* \theta}{D_c} \right), \quad (2.10)$$

where  $\mu$  is the kinetic coefficient of friction,  $\mu_0$  is the nominal coefficient of friction,  $V_s$  is the sliding velocity,  $\theta$  is a state variable (in units of time) dependent on time and displacement,  $A$  and  $B$  are constitutive parameters that measure the effects of rate and material state, respectively,  $V_s^*$  is a normalising constant, and  $D_c$  is a critical slip distance that is determined experimentally. Fortt and Schulson (2009) concluded that when velocity changes are confined to either the velocity-weakening or velocity-strengthening regime, the sensitivity of the friction coefficient to changes in the sliding velocity does not change and is comparable to that calculated from constant-velocity tests. However, when the sliding velocity is increased from the velocity-strengthening regime to the velocity-weakening regime and vice versa, the coefficient of friction is history dependent. The authors attributed this history dependence to the effect (or lack of effect) of cohesion across the sliding interface. Lishman et al. (2011) suggested using a single-state-variable constitutive law that predicts the nature of the memory effects in moving ice-ice contact.

$$\begin{aligned} \mu &= \mu_0 + \theta + A \ln \frac{V}{V_*} \\ \frac{d\theta}{dt} &= -\frac{V}{D_c} \left( \theta + B \ln \frac{V}{V_*} \right). \end{aligned} \quad (2.11)$$

The effective friction  $\mu$  comprises of three terms: a constant term  $\mu_0$ , a rate-dependent term  $A \ln(V/V_*)$ , and state dependence. The state dependence term is controlled by the dynamics of the second equation in Eq. (2.11). Here  $\theta$  is the state variable,  $t$  is time,  $V$  is the slip rate,  $V_*$  is a characteristic slip rate, and  $D_c$  is the critical slip displacement.  $A$ ,  $B$ , and  $\mu_0$  are empirically determined parameters of the model. Lishman et al. (2011) noted that Eq. (2.11) should be coupled with a spring slider model for the pushing force to correctly predict the dependence of the static friction coefficient on hold time. The proposed model was found to be in satisfactory agreement with the experimental data. The key parameter in the model was the critical slip displacement  $D_c$ . The analysis of the experimental data showed that the critical slip displacement cannot be considered as a material constant for ice but that it varies with scale. In their recent paper Lishman et al. (2013) modified their model and suggested to use a critical slip time instead of a critical slip displacement. The critical slip time is the time over which critical slip occurs. Lishman et al. (2013) found that critical slip time remains constant over a range of slip rates and scales.

### 2.2.2 Experimental setups to study ice friction

There are several types of experimental setups to perform tests on ice friction.

The first type is using a turntable filled with ice. This technique was used in a number of ice friction studies reported in the literature (Akkok et al., 1987; Bäurle, 2006;

Calabrese et al., 1980; Kietzig et al., 2009; Oksanen and Keinonen, 1982). Evans et al. (1976) used a revolving ice at constant speed and two sliders supported on its surface by a pendulum frame. By measuring the deflection angle of the pendulum from its equilibrium position, the frictional force was obtained. This type of experimental setup has a very significant weak point: the sliding occurs between a slider and a sliding track (ice) in a repetitive manner. Therefore, the ice track during the friction tests will be heated, and a melt water layer will be formed that will drastically affect the results. To avoid this problem, Baurle (2006) designed a tribometer with the diameter of the track at the position of the slider equal to 1.60 m. Thus, the ice surface was refrozen between two sequential passes of the slider. Similar precautions with some variations were taken by other authors (Evans et al., 1976; Oksanen, 1983). The vibration of the apparatus due to rotation is also an important issue that should be considered when using this type of setup.

Another type of experimental setup is a linear experimental device. In this case, the slider is forced to move along a straight line by a pulling mechanism and, therefore, constantly “meets” unmodified (“new”) ice. This type of setup was used by many authors (Forland and Tatinclaux, 1985; Frederking and Barker, 2002; Gavriilo, 1984; Kennedy et al., 2000; Lishman et al., 2011; Pritchard et al., 2012; Repetto-Llamazares et al., 2011; Ryvlin, 1973; Saeki et al., 1986; Schulson and Fortt, 2012; Sukhorukov et al., 2012; Tabata and Tusima, 1981; Tatinclaux and Murdey, 1985; Tusima and Tabata, 1979). The majority of the setups of this type used in above works have a significant problem: the applied pulling force is not applied along the same straight line as the frictional force. Therefore, an unbalanced moment arises, and non-uniform pressure is distributed over the contact interface. To avoid this problem, Lishman et al. (2011), Kennedy et al. (2000), and Schulson and Fortt (2012) used a special symmetrical arrangement with a double shear configuration. Two ice blocks were sliding on opposite faces of a third ice block located between them. Lishman et al. (2011) used a similar arrangement in their basin tests performed at the Hamburg Ice Basin (HSVA). The use of such an arrangement in field conditions is very demanding. Thus, in all tests performed in the field (Gavriilo, 1984; Pritchard et al., 2012; Ryvlin, 1973; Sukhorukov et al., 2012), a conventional setup was used where one ice block was pulled along a straight sliding track.

## Chapter 3

### 3 Field investigation on the friction of sea ice against sea ice and steel

#### 3.1 Introduction

Numerous studies have been performed to investigate the friction between ice and different materials (Calabrese et al., 1980; Forland and Tatinclaux, 1985; Frederking and Barker, 2002; Liukkonen, 1988; Oksanen and Keinonen, 1982; Ryvlin, 1973; Saeki et al., 1986; Tatinclaux and Murdey, 1985; Tusima and Tabata, 1979). Several friction models and theories (Akkok et al., 1987; Evans et al., 1976; Liukkonen, 1992; Oksanen and Keinonen, 1982) were developed and verified using the results obtained in small-scale laboratory tests. Until recently, fewer studies have focused on the sliding of ice on ice. To date, most ice-ice friction studies have employed small-scale laboratory tests (Fortt and Schulson, 2007; Fortt and Schulson, 2009; Fortt and Schulson, 2011; Kennedy et al., 2000; Maeno and Arakawa, 2004; Maeno et al., 2003; Repetto-Llamazares et al., 2011; Schulson and Fortt, 2012). Most of these laboratory tests were performed with artificially formed and very smooth ice surfaces (Kennedy et al., 2000; Maeno et al., 2003). Other tests on ice-ice friction were conducted when sliding occurred along Coulombic shear faults (Fortt and Schulson, 2007; Fortt and Schulson, 2009; Fortt and Schulson, 2011). In their tests, the authors used very small samples, and sliding of several millimetres occurred. Such well-controlled small-scale laboratory tests help to understand the physics of the ice friction and the effect of various parameters on the friction coefficient (e.g., sliding velocity, temperature, normal load), but the results may not be fully applicable to larger scales. Lishman et al. (2011) performed ice-ice friction tests in the Hamburg Ice Basin (HSVA) and used an analogy with the friction in rocks (Dieterich, 1978; Gu et al., 1984; Ruina, 1983). These authors proposed a rate- and state-dependent friction model for saline ice. A similar approach was used by Fortt and Schulson (2009). From an engineering perspective, it is important to compare how well the dependences obtained in the laboratory and basin tests describe friction processes in the field. To the best of our knowledge, only a limited amount of field data are available for sea ice-sea ice friction (Gavrilo, 1984; Pritchard et al., 2012; Ryvlin, 1973). In all of these tests, the authors used an elastic cable to pull ice blocks and studied the effect of the velocity, normal load, and presence of snow on the surface of the level ice.

This chapter presents description of setup development and results from the field tests performed during three field seasons (March-April 2010, 2011 and 2012) at Spitsbergen and in the Barents Sea on the friction of sea ice on sea ice and steel. The main purpose of the experiments was to determine the most important factors that affect the friction of sea ice on sea ice and corroded steel in field conditions and to determine whether the existing friction models (Evans et al., 1976; Oksanen and Keinonen, 1982) are in agreement with these data. The influences of the sliding velocity, air and ice track temperature, normal load, and ice block sliding direction in relation to the ice grain

orientation were studied. Furthermore, the presence of sea water in the sliding interface on the friction coefficient was investigated and discussed.

### 3.2 Development of the setup

Field experiments on the friction of sea ice on sea ice were performed in March and April of 2010, 2011 and 2012. In 2010, the tests were conducted near Akselöya Island at Spitsbergen (77°43.664 N, 14°46.565 E). In 2011, all the tests were performed in the Adventfjord (78°13.604 N, 15°38.637 E) at Spitsbergen. In 2012, some of the tests were conducted in the Van Mijenfjord at Spitsbergen, and the remainder was performed near Edgeøya Island (77°21.784 N, 24°05.743 E) in the Barents Sea.

Figure 3.3 shows photos of the experimental setups used in 2010-2012. In 2010, ice blocks were slid along the track using a pulling mechanism, which was driven by an electrical motor and operated at two speeds: 350 rpm and 1200 rpm. The motor was geared down using a system of gearing wheels, and three different pulling velocities were used in the tests. The pulling force was measured using a load cell attached between the pulling chain and the ice block. The mean velocity of the ice block was estimated roughly by dividing the sliding length by the elapsed time.

Significant modifications and improvements of the experimental setup were done in 2011. The improvements provided better control of sliding velocity and decreased compliance of the actuating mechanism. Unfortunately, we could not check whether setup modifications decreased stick-slip motion of sliding mass. The main reason for this is that sliding velocities in tests with different setups did not overlap. Figure 3.4 shows sketches of the experimental setups used in 2011 and 2012. In the tests, ice blocks were slid along tracks using a pulling mechanism driven by a linear actuator with a controlled velocity.

In 2011, the linear actuator (LA30, LINAK) with a stroke length of 40 cm was used in the tests as the pulling mechanism. The pulling velocity ranged from 6 mm s<sup>-1</sup> to 43 mm s<sup>-1</sup>. The force was measured using a load cell attached between the ice block and a pulling rod. Depending on the expected load level, one of the two available load cells, having a capacity of 490 N and 1960 N, was used in the tests. The pulling rod was connected to the actuator shaft via a small sledge that prevented the shaft from revolving (Figure 3.4a). The load cell was supported in the horizontal position and attached at a height such that the rod was also close to horizontal alignment. A displacement transducer was used to measure the ice block position in time, and the average sliding velocity was obtained from these data. The actuator and displacement transducer were mounted on a plate of plywood, which was attached to the level ice by four ice screws. Data were collected using a CR100 data logger (Campbell Scientific) at a sampling rate of 50 Hz.

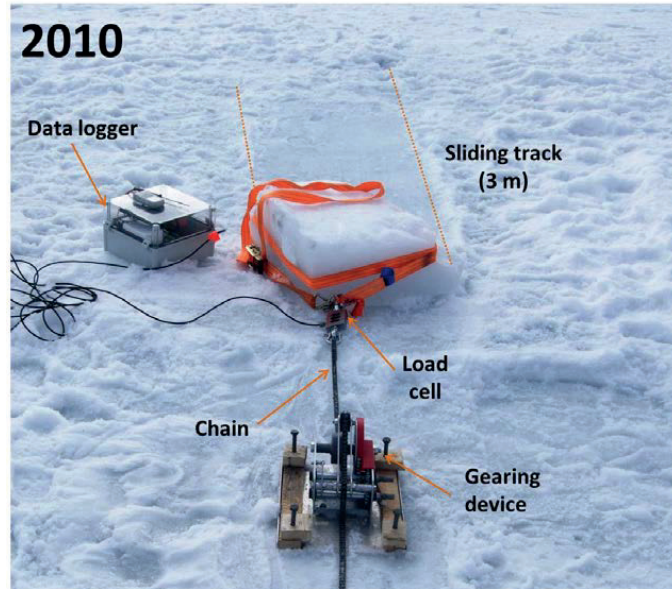


Figure 3.1. Experimental setup used in 2010.

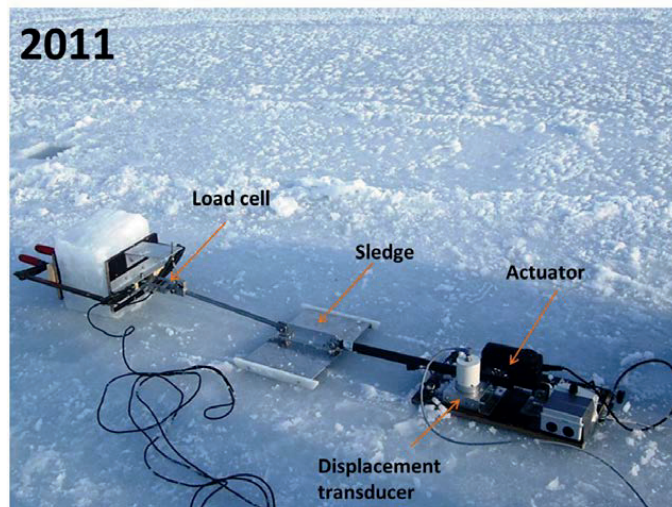


Figure 3.2. Experimental setup used in 2011.

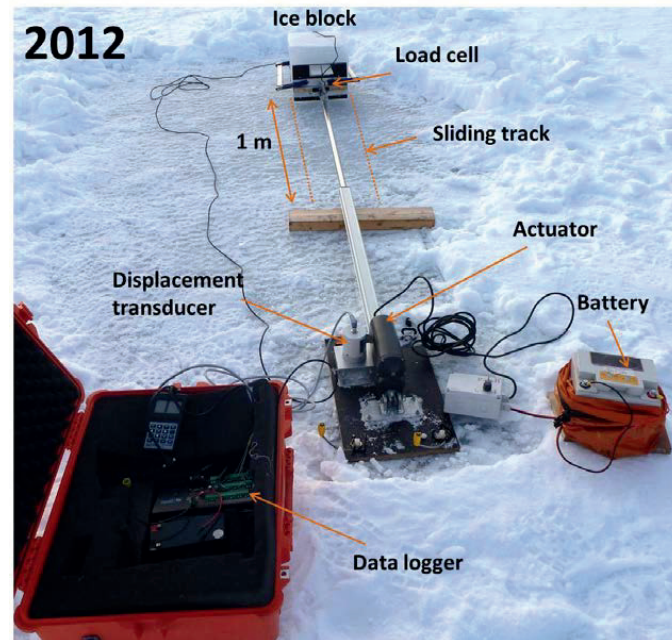


Figure 3.3. Experimental setup used in 2012.

In 2012, another linear actuator, LA36, with a stroke length of 100 cm was used. This actuator allowed ice blocks to be pulled at velocities of up to  $110 \text{ mm s}^{-1}$ . The actuator shaft did not revolve during the motion and could therefore be directly connected to the load cell (Figure 3.4b). In friction tests with a high normal load, the power of actuator LA36 was not sufficient. Therefore, actuator LA30 was used for these tests. The load cells, displacement transducer, and data acquisition system were the same as the experiments in 2011.

Two types of tests were performed to study the friction of sea ice on sea ice: “wet” friction tests and “dry” friction tests. In the “wet” friction tests, the interface between the sliding ice block and underlying ice was flooded with sea water (Figure 3.4 c-d), while in the “dry” friction test, the ice blocks slid along the “dry” level ice surface (Figure 3.4 a-b). The term “dry” friction test is not fully correct in our case because of the water layer that forms on the surface due to ice melting. Real dry ice friction can be achieved only at very low temperatures and low velocities, conditions that were not the case in our testing.

The experimental setup to perform “wet” friction tests is shown schematically in Figure 3.4(c-d). An ice block with horizontal dimensions of approximately 1.2 m by 0.90 m was cut from the level sea ice. The block was submerged horizontally under the water such that a water layer with a thickness ranging between 15 and 35 mm flooded the top surface of the block. To submerge the block and keep it stationary in the submerged



position, we used the following procedure: two 1.5-m-long boards were placed parallel to each other on the top of a floating ice block and were attached to the level ice by four ice screws. Four 35-mm-thick wooden prisms were inserted between the wooden boards and floating ice block such that the top surface of the block was submerged. In this position, the submerged ice block was attached with four ice screws to the boards to prevent the vertical displacement of the block.

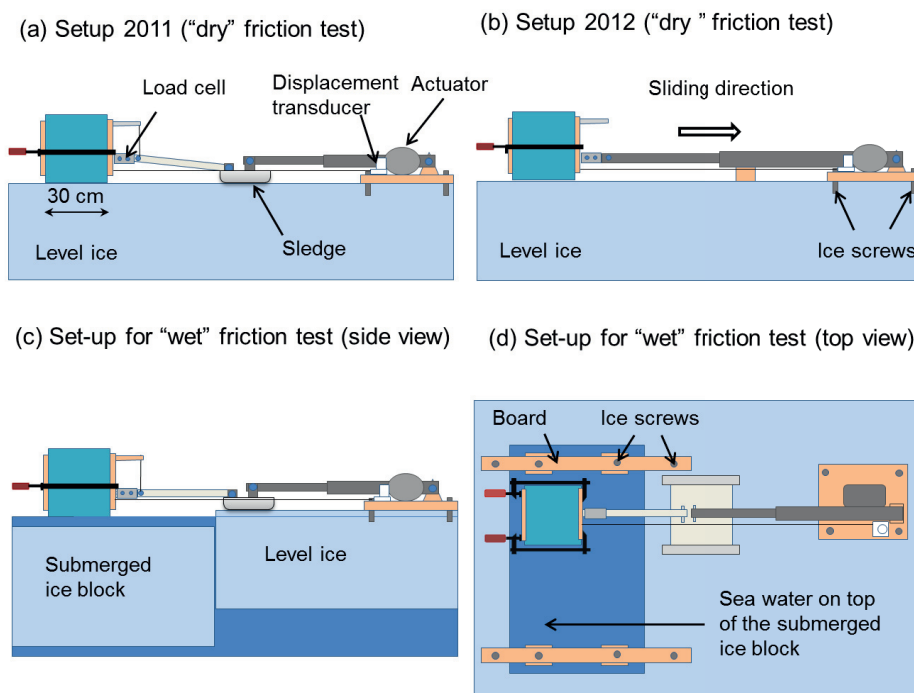


Figure 3.4. Experimental setup: (a) 2011 setup used in "dry" friction tests; (b) setup used in most of the tests in 2012; (c) and (d) are the side and top views, respectively, of the setup used to perform the "wet" friction tests.

### 3.3 Experimental procedure and test parameters

The state of the sea ice surface observed in the field varied significantly. Temperature variations, the presence of precipitation in the form of rain and snow, flooding by sea water, and multiple cycles of freezing and melting are possible factors that influence sea ice surface roughness. Sliding on very uneven surfaces with bumps and dimples led to ice block wobble and large oscillations in the measured friction forces. Such data are difficult to interpret, and therefore, only ice with a sufficiently smooth surface was used in the tests. To prepare a sliding track, the top surface of the level ice was first carefully cleared from the snow with a shovel and then with a brush.

The ice blocks used in the tests as sliders were obtained from the level sea ice and resembled rectangular prisms with a height ranging from 0.24 m to 0.35 m and horizontal dimensions ranging from 0.24 m to 0.37 m. The top and bottom surfaces of the sliding blocks were not specially prepared before the test. The idea was to study the friction when it occurs along natural surfaces. The roughness of the side surfaces of the ice blocks was created artificially during the sawing process. The ice block used in the tests in most cases did not reach thermal equilibrium with the air. The time between when an ice block was extracted from the level ice and used in the test varied between 20 min to 2 hr. Therefore, we reported the air temperature, ice track temperature, and temperature of the sliding surface of an ice block.

The effect of the sliding velocity, normal load, ice block sliding direction in relation to the ice columnar grain orientation, and surface polishing on the kinetic friction coefficient were studied in both the “dry” and “wet” friction tests.

The effect of sliding velocity in the 2011 tests was studied by pulling ice blocks at different sliding velocities along the same ice track. From run to run, the velocity was changed randomly and ranged between  $6 \text{ mm s}^{-1}$  and  $43 \text{ mm s}^{-1}$ . The analysis showed that the first eight to ten measurements were fairly scattered because of surface polishing.

In the 2012 tests, the velocity range used in the tests ranged between  $6 \text{ mm s}^{-1}$  and  $110 \text{ mm s}^{-1}$ . Two groups of tests were performed to study the effect of velocity. In the first group of tests, ice blocks were pulled along their bottom surface (skeleton layer) along the natural surface of the level ice. Each block was pulled at only one chosen velocity several times along the corresponding ice track. The values for the kinetic friction coefficient obtained in the first run for each block characterised the friction coefficient between the two natural surfaces and thus included the effect of surface smoothening.

In the second group of tests, an ice block slid along the same track many times. The velocity from run to run was changed in a cyclic order. In the first run, the ice block was pulled at the highest velocity,  $v_5$  (approximately  $110 \text{ mm s}^{-1}$ ); in the second run at the slowest velocity,  $v_1$  (approximately  $10 \text{ mm s}^{-1}$ ); in the third run at a velocity  $v_2 > v_1$ ; in the fourth run at a sliding velocity  $v_3 > v_2$ , then at  $v_4 > v_3$ , and finally again at the highest velocity,  $v_5$ . This cycle of runs, where the velocity was changed in increasing order from  $v_1$  to  $v_5$ , was repeated several times.

To study the effect of the normal load on the friction coefficient, thick steel plates with a weight of 343 N each were placed on top of the sliding block. Thus, it was possible to vary the normal load from approximately 250 N (the weight of the sliding ice block) to 2000 N when all five steel plates (dead weights) were placed on the top. The tests were performed for both the “dry” and “wet” friction conditions.

Growing in natural conditions, sea ice is a polycrystalline material with different structures, sizes and orientations of ice crystals at the top and at the bottom. The properties of sea ice depend on the size, the orientation of its crystals, its salinity, its temperature, its density and the presence of impurities (Løset et al., 2006). The top surface of the level ice is granular ice with randomly oriented crystals and ice platelets <

0.5 mm thick (Løset et al., 2006; Weeks, 2010). Below the granular layer, there is typically a fairly thin transition zone (5 to 30 cm), where crystal orientation undergoes a rapid change. The ice below the transition zone is called columnar ice, with the dominant crystals having their c-axes horizontal and showing pronounced elongation parallel to the direction of heat flow. The average crystal size in columnar (S2) ice is equal to 10 mm. On the bottom of the growing sea ice, a mushy layer, also called a skeleton layer, is formed. Figure 3.5 shows two horizontal and one vertical thin sections of the level sea ice that was used in the tests in 2011. The salinity at the top, middle and bottom of the ice block was 8.7 ppt, 7.4 ppt and 11.9 ppt, respectively.

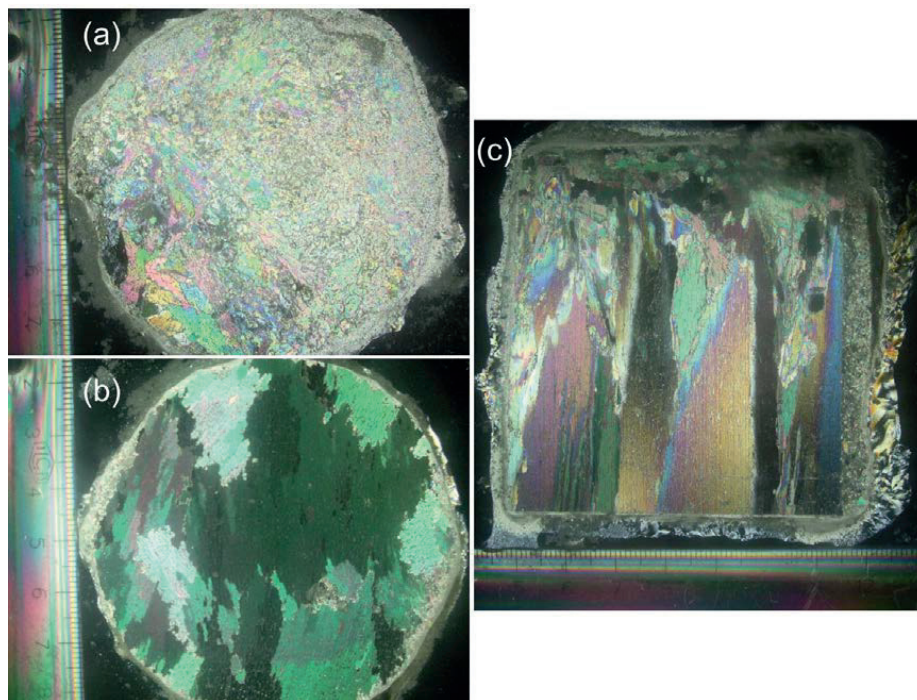


Figure 3.5. Thin sections of the first year sea ice used in the 2011 tests: (a) horizontal thin section of the top level of sea ice with granular structure; (b) horizontal thin section of the bottom level of the sea ice with columnar structure; (c) vertical thin section of the level ice from the transition zone, when ice changes its structure from granular to columnar.

The effect of the ice block sliding direction in relation to the ice columnar grain orientation was investigated by placing the ice blocks on their various sides and pulling them along the track. Four different block orientations are shown in Figure 3.6. The sliding configuration in which the bottom surface of the ice block slid on the top surface of the level ice is denoted as bottom-top. The second sliding configuration is denoted as side(II)-top, which corresponds to the case in which the ice block was placed on its side and pulled along the ice growth direction on the top surface of the level ice. The sliding

configuration in which the ice block was placed on its side and pulled perpendicular to the ice growth direction is denoted as side( $\perp$ )-top. In the final configuration, denoted as top-top, the top surface of the ice block (granular ice) was pulled along the ice track.

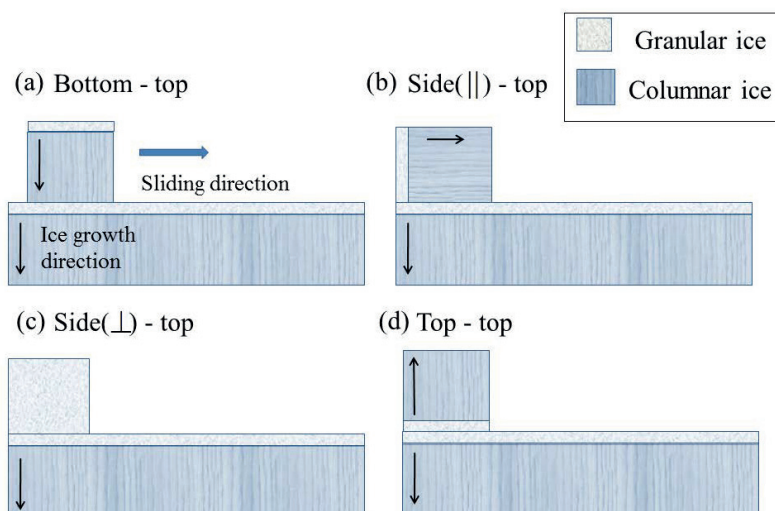


Figure 3.6. Ice block sliding directions in relation to the ice grain orientation. The different ice block sliding directions in relation to the ice grain orientation correspond to sliding configuration (a) bottom-top, (b) side( $\parallel$ )-top, (c) side( $\perp$ )- top, and (d) top-top.

Several edge sliding tests were performed to study edge sliding effect on the friction coefficient in 2011. The ice block was placed on its edge and kept aligned by a wooden frame (Figure 3.7). The frame did not carry the horizontal load due to the pinned connection between its parts and thus did not influence the measured friction force. In the tests, the ice block was pulled both perpendicular and parallel to its edge along the “dry” level ice surface.

The effect of the stationary contact time on the static friction coefficient was studied in both the 2011 and 2012 tests. In these tests, the ice block was pulled along the track for a small distance and then stopped for a certain time (the hold time or stationary contact time ranged from 5 s to 960 s). The ice block was then pulled again and stopped again. In our tests, the first peak load was associated with the static friction force. Some authors distinguish the break-away friction coefficient from the static friction coefficient (Calabrese et al., 1980; Olsson et al., 1998). According to Olsson et al. (1998), where static friction is the friction when sticking and the break-away force is the force required to overcome the static friction and initiate motion. The break-away friction force varies significantly with the hold time (time during which the surfaces were in stationary contact) and the rate of increase of the external load. In the current paper, we do not distinguish break-away friction from the static friction.

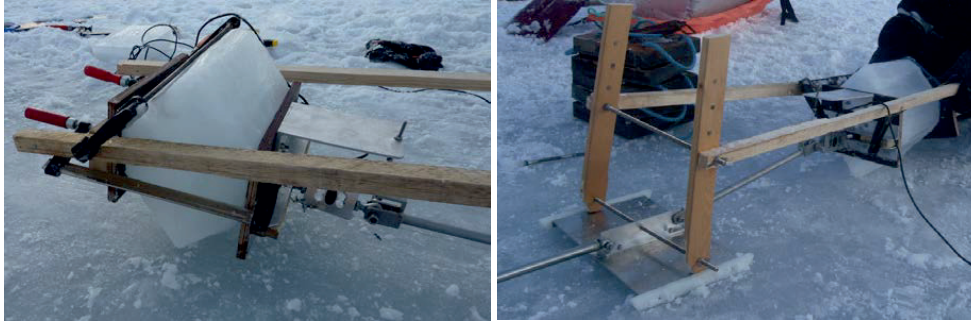


Figure 3.7. Experimental arrangement for sliding on the edge of the ice block. Sliding occurred both along and perpendicular to the block edge.

### 3.4 Results

The main focus in the tests was to study friction of sea ice on sea ice. Nevertheless some tests were performed to study friction of sea ice on corroded steel. The results are given separately in subsections below.

Two distinctive sliding regimes were observed in the tests. The first regime (shown in Figure 3.8) is associated with steady sliding. The first peak load corresponds to the force needed to overcome static friction. After sliding was initiated, the pulling force had to balance the kinetic friction force. The static and kinetic friction coefficients were calculated using the well-known expression

$$\mu = \frac{F_f}{F_n}, \quad (3.1)$$

where  $F_f$  is the static or kinetic friction force and  $F_n$  is the normal load. The kinetic friction force was obtained by taking an average of the measured friction force over the time when the ice block was steadily sliding.

The second regime is associated with the stick-slip motion shown in Figure 3.9. The stick-slip regime was observed in some tests at a low sliding velocity. Fourier analyses indicated that load oscillations in the stick-slip regime had frequencies between 20 Hz and 25 Hz. Our acquisition system did not allow us to sample data at rates higher than 50 Hz. Therefore, we obtained very few points per stick-slip cycle. In future tests, an acquisition system with higher sampling rates should be used. In tests where stick-slip was observed, the static and kinetic friction forces were calculated in the same manner as in the tests without stick-slip. The value for the kinetic friction coefficient was obtained using the middle portion of the temporal variation of the friction force.

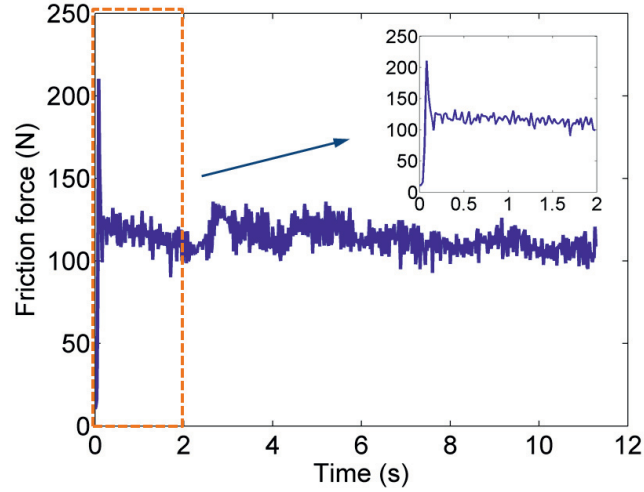


Figure 3.8. Temporal variations of the frictional force (steady sliding regime). The normal force was  $F_n = 276.8$  N, the apparent contact area  $S_a = 0.0714$  m<sup>2</sup>, the sliding velocity  $v = 87.7$  mm s<sup>-1</sup>,  $T_{air} = -2^\circ\text{C}$ ,  $T_{track} = -2.9^\circ\text{C}$ , and the ice block sliding surface temperature  $T_{ice\ block} = -2.3^\circ\text{C}$ . The bottom-top sliding configuration was used in the tests.

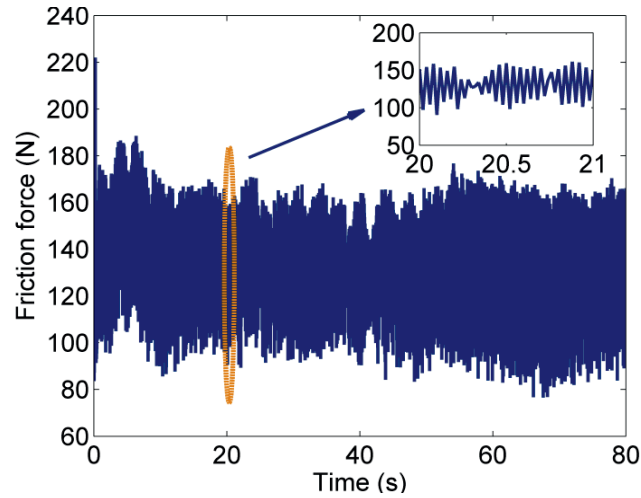


Figure 3.9. Temporal variations of the friction force in the friction tests (stick-slip regime). The normal force was 242.4 N,  $S_a = 0.101$  m<sup>2</sup>,  $v = 5.4$  mm s<sup>-1</sup>, the air temperature  $T_{air} = -10.6^\circ\text{C}$ ,  $T_{track} = -5.5^\circ\text{C}$ , and  $T_{ice\ block} = -4.4^\circ\text{C}$ . The bottom-top sliding configuration was used in the tests.

### 3.4.1 Ice-ice friction

#### Effect of repeated sliding on the kinetic friction coefficient

Microscopic surface topography (roughness) of the contacting surfaces influences the friction coefficient. The ice surface changes significantly during the sliding because of the improvement in the alignment of the opposing faces, deformation and breakage of the contacting asperities, surface melting, and re-freezing. In this section, we present the results from four sets of tests in which the ice blocks slid repeatedly over the same ice track. The experimental parameters are presented in Table 3.1, and the results in Figure 3.10.

The highest value for the kinetic friction coefficient was obtained in the first run, when natural ice surfaces slid against each other. The following runs with the same surfaces led to a significant decrease in the kinetic friction coefficient. In test sets Rs2 and Rs4, the friction coefficient decreased by a factor of ten (from 0.48 to 0.05). In two other sets (Rs1 and Rs3), the kinetic friction coefficient also decreased with the number of runs, but the change was not as significant as in the other tests.

Table 3.1. Experimental parameters in the tests with surface smoothening due to repeated sliding over the same ice track.

Set no.	Configuration	Interface	$T_{track}$ (°C)	$T_{ice\ block}$ (°C)	$T_{air}$ (°C)	$F_n$ (N)	$S_a$ (m <sup>2</sup> )	$v$ (mm s <sup>-1</sup> )
Rs1	Bottom-top	“Dry”	-5.4	-5.0	-11.6	260.1	0.112	101.3 ± 4.8
Rs2	Bottom-top	“Wet”	-1.8	-1.8	-12.4	207.2	0.101	92.4 ± 9.3
Rs3*	Bottom-top	“Dry”	-11.2	-6.0	-13.2	314.8	0.075	98.8 ± 3.0
Rs4	Top-top	“Dry”	-5.7	-6.1	-11.4	243.2	0.102	101.1 ± 6.0

\*The test set was performed in the Van Mijenfjord at Spitsbergen. The rest of the tests were done in the Barents Sea.

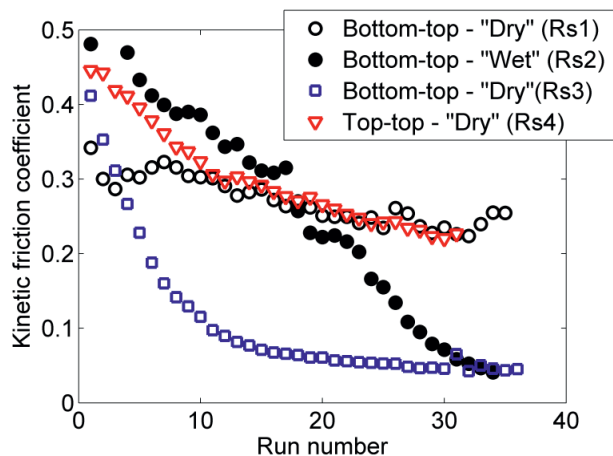


Figure 3.10. Dependence of the kinetic friction coefficient on run number in tests with surface smoothing. The test parameters are listed in Table 3.1. Test sets Rs1, Rs2 and Rs4 were performed with ice in the Barents Sea. The test set Rs3 was performed in the Van Mijenfjord at Spitsbergen.

#### Effect of the velocity on the kinetic friction coefficient

The effect of the sliding velocity on the kinetic friction coefficient was studied in different sets of experiments. In the first set of experiments, we studied the effect of velocity when sliding occurred between natural (unsmoothed) surfaces. A total of 13 ice blocks were used for this type of test. Each ice block slid on its bottom (skeleton layer)/top surface on a corresponding ice track (snow-free, level ice surface). In total, each block had three runs along the same ice track. In the second set of tests, the ice block slid along the same ice track many times. The block was pulled at different velocities, which changed in a cyclic order, as described in Section 3.2. In these experiments, both surface smoothing and the sliding velocity affected the friction coefficient. In the third set of tests, the sliding occurred between preliminary smoothed surfaces, and the velocity changed in a random order. Three sliding configurations were tested: bottom-top, side( $\perp$ )-top, and side( $\parallel$ )-top.

##### A. Friction between natural (unsmoothed) sea ice surfaces

The ice blocks sawn from the level ice slid on their bottom (skeleton layer) or top surfaces on a snow-free, level ice surface. Three series of tests were performed during the field season in 2012. One test series was performed in the Van Mijenfjord at Spitsbergen (bottom-top sliding configuration), and two test sets were performed in the Barents Sea close to Edgeøya Island for the top-top (Series 1) and bottom-top (Series 2) sliding configurations. The test parameters and static and kinetic friction coefficients are listed in Table 3.2.



Table 3.2. Test parameters and static and kinetic friction coefficients. The effect of the velocity is studied when sliding occurs between natural (unsmoothed) surfaces. Each block slid on the corresponding ice track three times at a certain velocity. The average values from the three runs for the static and kinetic friction coefficients are given.

Block	$v$ (mm s <sup>-1</sup> )	$T_{track}$ (°C)	$T_{ice\ block}$ (°C)	$T_{air}$ (°C)	$F_n$ (N)	$S_a$ (m <sup>2</sup> )	$\mu_{st}$	$\mu_k$
Tests in the Van Mijenfjord at Spitsbergen								
VM1	104.8 ± 0.3	-2.4	-2.4	-2 ± 1	298.8	0.084	0.63 ± 0.06	0.41 ± 0.03
VM2	6.4 ± 2.0	-2.9	-2.9	-2 ± 1	294.8	0.114	0.55 ± 0.06	0.43 ± 0.01
VM3	48.3 ± 2.8	-2.7	-2.4	-2 ± 1	312.8	0.082	0.67 ± 0.13	0.42 ± 0.01
VM4	16.6 ± 1.1	-2.9	-2.8	-2 ± 1	276.8	0.068	0.51 ± 0.12	0.42 ± 0.01
VM5	38.6 ± 0.6	-2.9	-2.3	-2 ± 1	269.8	0.068	0.77 ± 0.27	0.44 ± 0.03
VM6	87.2 ± 0.8	-2.9	-2.7	-2 ± 1	310.8	0.082	0.59 ± 0.01	0.41 ± 0.03
Tests in the Barents Sea, Series 1								
S1BS1	16.8	-4.7	-4.9	-8.8	242.4	0.976	0.8	0.52
S1BS2	60.7 ± 1.8	-5.7	-5.9	-10.8	266.2	0.112	0.86 ± 0.10	0.43 ± 0.01
S1BS3	97.8 ± 4.1	-5.7	-6.1	-11.4	243.2	0.102	0.76 ± 0.30	0.44 ± 0.01
Tests in the Barents Sea, Series 2								
S2BS1	12.1 ± 6.5	-5.5	-4.4	-10.6	242.4	0.101	0.86 ± 0.17	0.49 ± 0.05
S2BS2	37.1 ± 0.7	-4.0	-4.1	-10.5	251.9	0.111	0.71 ± 0.38	0.46 ± 0.05
S2BS3	58.4 ± 2.8	-5.1	-5.0	-12.0	243.3	0.099	0.74 ± 0.23	0.42 ± 0.03
S2BS4	91.2 ± 1.3	-5.2	-4.8	-11.9	266.3	0.112	0.73 ± 0.37	0.44 ± 0.05

Figure 3.11 shows the dependence of the kinetic friction coefficient on the sliding velocity. The kinetic friction coefficient was found to be independent of the velocity when sliding occurred along unprepared, natural surfaces. Repeated runs over the same track led to a decrease in the kinetic friction coefficient in all tests.

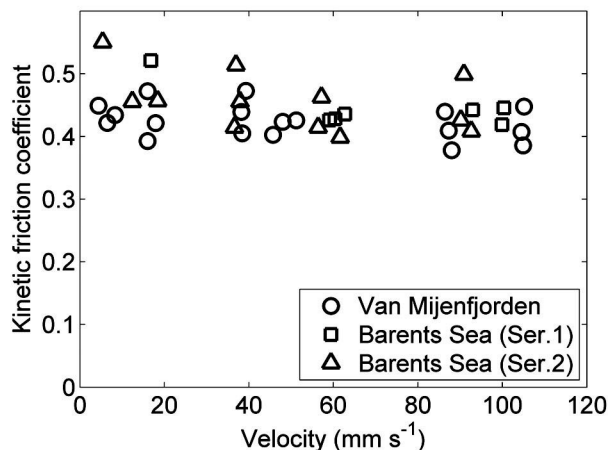


Figure 3.11. Kinetic friction coefficient versus sliding velocity in tests with natural ice surfaces. Three test series were performed: (1) tests in the Van Mijenfjorden at Spitsbergen (VM1 - VM6), (2) tests in the Barents Sea, Series 1 (S1BS1 – S1BS3), (3) tests in the Barents Sea, Series 2 (S2BS1 – S2BS4). The test parameters are listed in Table 3.2.

The values for the static friction coefficient ranged between 0.44 and 1.15. Such scatter in the static friction coefficient values could be explained by the different hold times (the time during which the ice block was stationary before sliding and necking between asperities in the two surfaces could occur). Another reason for scatter could be the low sampling frequency (50 Hz). Therefore, the highest value for the friction force likely was not always registered.

#### B. Friction on gradually smoothing surfaces

When sliding surfaces become smoother, the sliding velocity becomes more important for the kinetic friction coefficient. In this set of tests, the sliding velocity changed from run to run in a cyclic order. Figure 3.12 shows how the kinetic friction coefficient depends on the velocity and run number. Together with decrease in the friction coefficient due to repeated sliding, we can clearly see the change in the friction coefficient due to change in sliding velocity.

#### C. Sliding on smoothed surfaces

Figure 3.13 shows the effect of velocity in “dry” friction tests for three different sliding configurations. Several first runs for each sliding configuration were removed from the plot to minimise the effect of surface smoothing and thus the significant decrease in the kinetic friction coefficient from run to run. The sliding velocity in the tests was changed in a random order. The kinetic friction coefficient was found to be independent of the sliding configuration when sliding occurred between preliminary smoothed contacting surfaces, which is in agreement with previously reported conclusions

(Kennedy et al., 2000; Ryvlin, 1973; Saeki et al., 1986; Tatinclaux and Murdey, 1985). The entire dataset was fit with a function proportional to  $v^{-1/2}$ , which is in agreement with the friction models (Akkok et al., 1987; Evans et al., 1976; Oksanen and Keinonen, 1982). Similar values for the kinetic friction coefficient and its velocity dependence were observed in the “wet” friction tests.

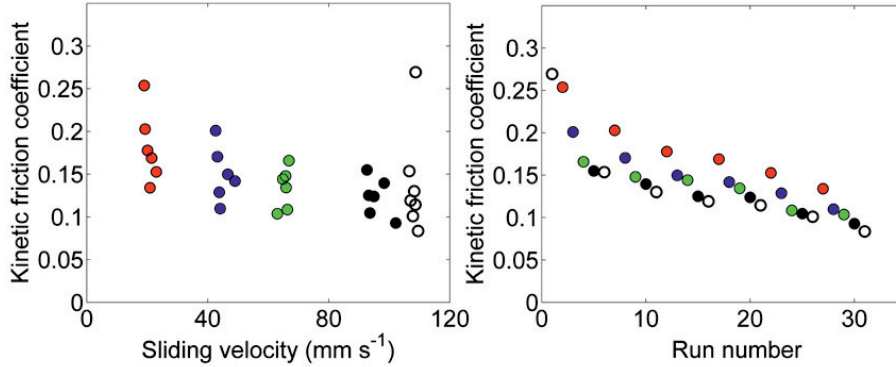


Figure 3.12. Kinetic friction coefficient versus sliding velocity (left figure) and run number (right figure) in the same set of tests. Markers with the same colour correspond to approximately equal sliding velocities. Test parameters:  $F_n = 208.5$  N,  $S_a = 0.088$  m<sup>2</sup>,  $T_{air} = -12.7^\circ\text{C}$ ,  $T_{track} = -3.9^\circ\text{C}$  and  $T_{ice\ block} = -5.7^\circ\text{C}$ . The bottom-top sliding configuration was used in the tests.

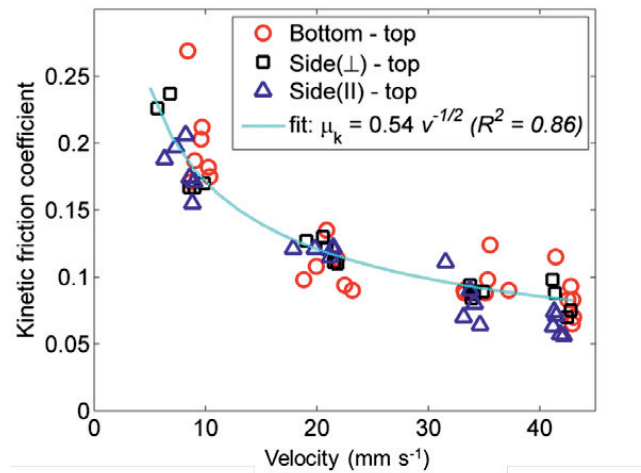


Figure 3.13. Kinetic friction versus sliding velocity for three sliding configurations in the “dry” friction tests. The normal loads and apparent contact area are  $F_n = 620$  N,  $S_a = 0.0765$  m<sup>2</sup> for the bottom-top sliding configuration, respectively;  $F_n = 620$  N and  $S_a = 0.0822$  m<sup>2</sup> for the side( $\perp$ )-top sliding configuration; and  $F_n = 560$  N and

$S_a = 0.0588 \text{ m}^2$  for the side(II)–top sliding configuration. The tests were performed at an air temperature of  $T_{air} = -22^\circ\text{C}$ . The tests were performed in the Advent fjord in 2011. The velocity in the fit equation has units of  $\text{mm s}^{-1}$ .

**Effect of the temperature on the kinetic friction coefficient**

In field conditions, the top surface of the level ice, sliding ice block, and air normally have different temperatures, and all of these temperatures may affect the friction coefficient. The dependences of the kinetic friction coefficient on the air temperature and ice track temperature were studied in both the “dry” and “wet” friction tests. The sliding velocity in all tests was the same ( $40.9 \pm 2.6 \text{ mm s}^{-1}$ ), while the normal load, apparent contact area, and surface roughness were different. The data obtained in the tests were significantly scattered and a firm trend could not be observed (Figure 3.14 and Figure 3.15). Both high (approximately 0.5) and low (approximately 0.05) values for the kinetic friction coefficient were obtained in tests at various air and ice track temperatures. The highest values for the friction coefficients were observed in tests where sliding occurred between natural surfaces (the first run). The kinetic friction obtained in the following runs decreased with run number.

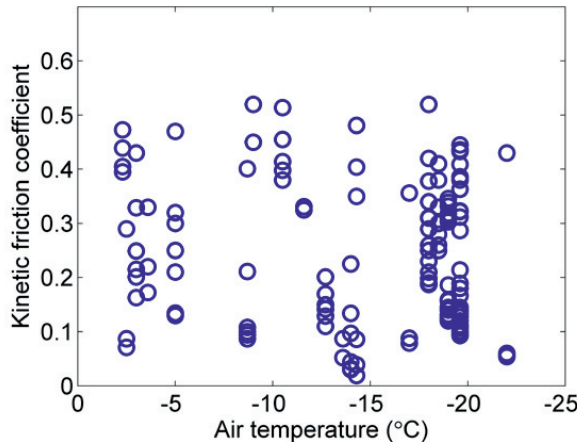


Figure 3.14. Kinetic friction coefficient versus air temperature in the “dry” and “wet” friction tests. The sliding velocity was  $40.9 \pm 2.6 \text{ mm s}^{-1}$ .  $S_a$  was between  $0.056 \text{ m}^2$  and  $0.110 \text{ m}^2$ , and  $F_n$  was between 214 N and 568 N.

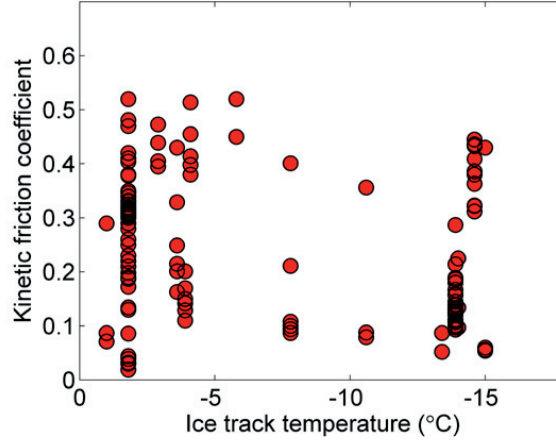


Figure 3.15. Kinetic friction coefficient versus ice track temperature in the “dry” and “wet” friction tests. The sliding velocity was  $40.9 \pm 2.6 \text{ mm s}^{-1}$ .  $S_a$  was between  $0.056 \text{ m}^2$  and  $0.110 \text{ m}^2$ , and  $F_n$  was between 214 N and 568 N.

It was pointed out above that the alignment of the opposing sliding faces and the decrease in ploughing component of the frictional resistance (due to ice surfaces changes) lead to significant decrease in the kinetic friction coefficient. Since we could not control the roughness of the ice surfaces, and in different tests the ice likely had different microscopic topography, it is impossible to find pure effects of the temperature on the friction coefficient in our field tests. Another aspect is that the strength and mechanical behaviour of ice are surely affected by temperature. Thus an increase of ice temperature may cause a more rapid “run in” and smoothening of the interacting surfaces.

#### Normal load effect

The effect of the normal load on the kinetic and static friction coefficients was studied in the “dry” and “wet” friction tests. The bottom-top sliding configuration was used in both sets of tests. The experimental parameters are listed in Table 3.3. Figure 3.16 shows the photos of the experimental sides in tests where effect of normal load was studied.

Table 3.3. Experimental parameters for the tests studying the effect of a normal load on the static and kinetic friction coefficients. The normal load ranged between 300 N and 2100 N. The bottom-top sliding configuration was used in these tests.

Interface	$v$ ( $\text{mm s}^{-1}$ )	$T_{track}$ ( $^{\circ}\text{C}$ )	$T_{ice\ block}$ ( $^{\circ}\text{C}$ )	$T_{air}$ ( $^{\circ}\text{C}$ )	$S_a$ ( $\text{m}^2$ )
“Dry”	$28.2 \pm 5.2$	-6.4	-3.5	-9.7	0.112
“Wet”	$30.9 \pm 6.4$	-1.8	-1.8	-11.6	0.097

Figure 3.17 shows the static and kinetic friction forces plotted versus the normal load. The data can be fit with the following linear function:

$$F = \mu_t F_n + F_o, \quad (3.2)$$

where  $\mu_t$  and  $F_o$  are constants and  $F_n$  is the normal load. In the literature, the constants  $\mu_t$  and  $F_o$  are sometimes called the true friction coefficient and initial cohesion force, respectively (Tatinclaux, 1989). The difference between the true friction coefficient and the friction coefficient defined by Eq. (3.1) disappears when the initial cohesion force is equal to zero. The presence of sea water in the sliding interface did not have a significant effect on the static and kinetic friction forces (Figure 3.17).

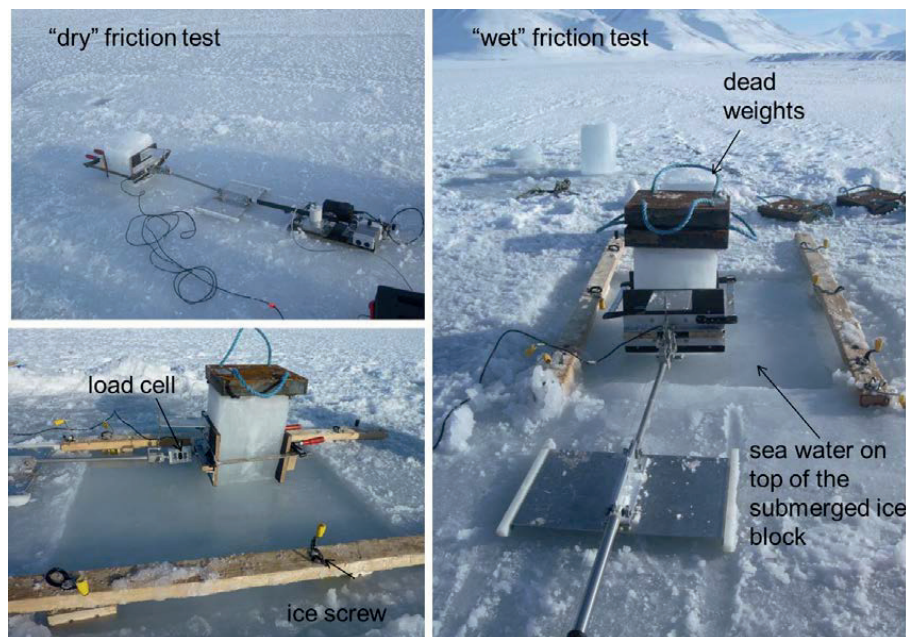


Figure 3.16. Test arrangements to study effect of normal load in “dry” and “wet” friction tests.

#### Sliding on the ice block edge

Sliding on ice block edges is more likely than sliding along the flat surfaces in rafting, ridge-building and pile-up processes. Several tests were performed to study the effect of edge sliding on the friction coefficient. The same ice block was first pulled 12 times parallel to its edge, then turned 90° and pulled 12 times perpendicular to the edge. The normal load was the same in both types of tests,  $F_n = 190.4$  N, while the apparent contact area increased during the tests mainly due to wear of the ice block edge. Apparent contact area, measured after the tests when sliding occurred parallel to the edge, was 17.4 cm<sup>2</sup>. Apparent contact area increased to 23.2 cm<sup>2</sup> after 12 slides

perpendicular to the ice block edge. The values for the friction coefficient and its dependence on velocity in the edge sliding tests are very similar to the results obtained in tests in which sliding occurred along the ice block side (Figure 3.18). The results from the other edge sliding tests showed similar effects of the sliding velocity on the friction coefficient but significant scatter in friction coefficient values. The effect of temperature might be the main reason for these discrepancies.

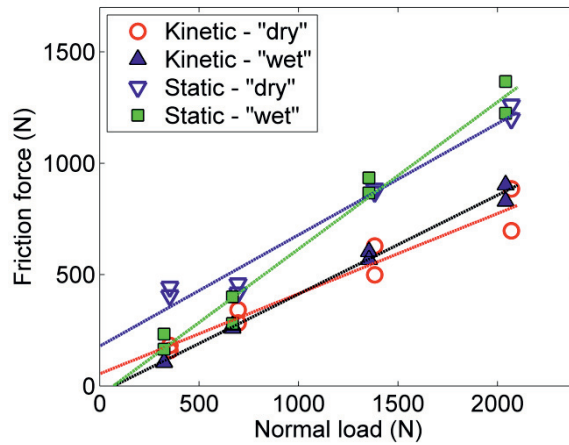


Figure 3.17. Kinetic and static friction forces versus normal load in the “dry” and “wet” friction tests. The experimental parameters are presented in Table 3.3.

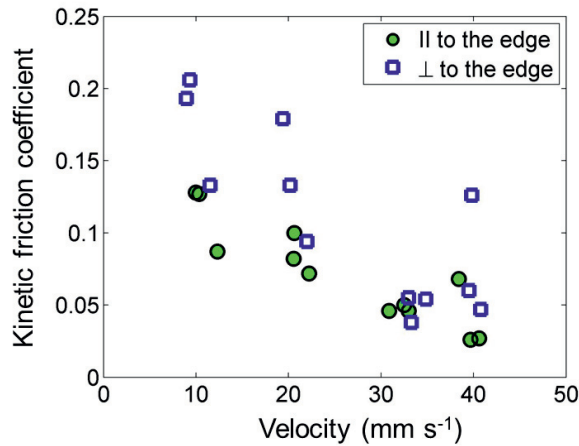


Figure 3.18. Sliding on the edge of the ice block. Sliding along the ice block edge and perpendicular to it was studied.  $T_{air} = -14^{\circ}\text{C}$ , normal load  $F_n = 190.4\text{ N}$ . Apparent contact area ( $S_a$ ) was  $17.4\text{ cm}^2$  after the tests with sliding  $\parallel$  to the edge, and  $23.2\text{ cm}^2$  after the tests with sliding  $\perp$  to the edge, respectively.

Static friction coefficient and its dependence on the hold time

Five sets of tests (StF1-StF5, see Table 3.4) were performed to study the effect of the hold time on the static friction coefficient. The hold time ranged between 5 s and 960 s. The contacting surfaces of the ice blocks used in the tests had different surface roughnesses and structures (see Figure 3.19). Test sets StF1-StF4 were performed under “dry” conditions, whereas test set StF5 was performed under the “wet” condition. In all test sets, the static friction coefficient increased with an increase in the hold time. A slightly lower static friction coefficient was measured in the “wet” friction tests (Figure 3.19).

Table 3.4. Experimental conditions and obtained static friction coefficient in tests with hold times.

Set no.	$F_n$ (N)	$S_a$ (m <sup>2</sup> )	$T_{air}$ (°C)	$T_{ice\ block}$ (°C)	$T_{track}$ (°C)	$v$ (mm s <sup>-1</sup> )	Hold time (s)	Data points	$\mu_{st}$
StF1	402	0.116	-13.6	-8	-11.8	-40	5	2	0.69 ± 0.12
							20	3	0.86 ± 0.05
							80	3	0.76 ± 0.34
							320	3	1.29 ± 0.11
StF2	427	0.088	-13.6	-11.8	-13.4	-40	5	4	0.71 ± 0.11
							20	3	0.75 ± 0.15
							80	3	0.87 ± 0.11
							320	3	0.96 ± 0.19
StF3	332.6	0.095	-12	-11.5	-11	-40	5	5	0.65 ± 0.13
							20	4	0.85 ± 0.19
							80	4	0.98 ± 0.05
							320	4	0.89 ± 0.18
							960	5	1.26 ± 0.03
StF4	326.5	0.083	-6.9	-	-	36.0	5	11	0.82 ± 0.09
							20	9	0.93 ± 0.04
							80	2	1.06 ± 0.01
StF5	295.6	0.09	-18	-1.8	-1.8	36.3	5	6	0.6 ± 0.05
							20	8	0.66 ± 0.09
							80	6	0.82 ± 0.13



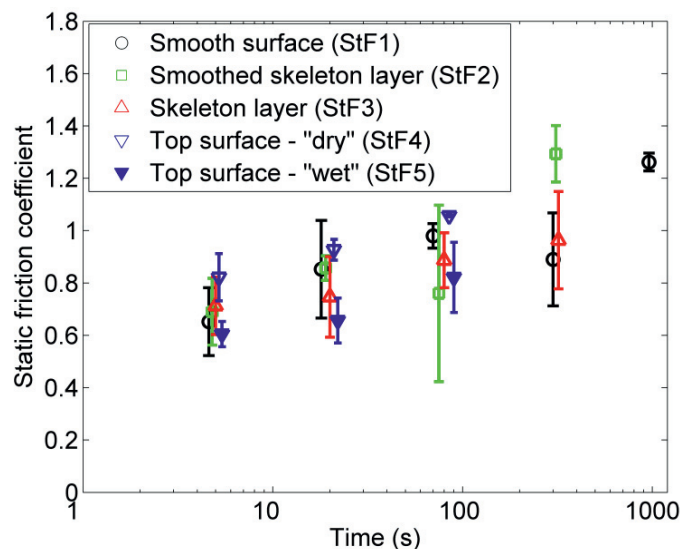


Figure 3.19. Static friction coefficient versus hold time. Four test sets were performed in “dry” conditions and one in “wet” conditions. To avoid overlap, the points on the time scale are displaced.

### 3.4.2 Ice-steel friction

Friction between sea ice and corroded steel was studied using the same experimental setup as in the ice-ice friction tests. A steel plate with horizontal dimensions of 60 cm by 120 cm was attached by ice screws to the level ice. Figure 3.20 and Figure 3.21 show the test arrangements used to study the friction between sea ice and steel in “dry” and “wet” conditions, respectively. The steel surface was corroded and had a mean surface roughness  $R_a = 10.7 \mu\text{m}$ . In the ice-steel friction test, the effects of the normal load, the presence of sea water in the sliding interface and the sliding configuration were studied.

#### Normal load effect

Figure 3.22 and Figure 3.23 show the kinetic and static friction force versus the normal load in the ice-steel friction tests. Two sliding configurations were tested: bottom – top (steel surface) and top – top (steel surface). The experimental parameters and conditions are listed in Table 3.5. A linear relationship between both the kinetic and the static friction forces and the normal load was observed. No clear effects of the sliding configuration or the presence of sea water in the interface were detected. The values for the static and kinetic friction coefficients are presented in Table 3.6. The kinetic friction coefficient between ice and corroded steel obtained in our tests is in agreement with the results obtained by Ryvlin (1973) and Saeki et al. (1986). However, we obtained somewhat higher values for the static friction coefficient. This difference in results may be attributed to the differences in roughness of ice and steel as well as in hold time.

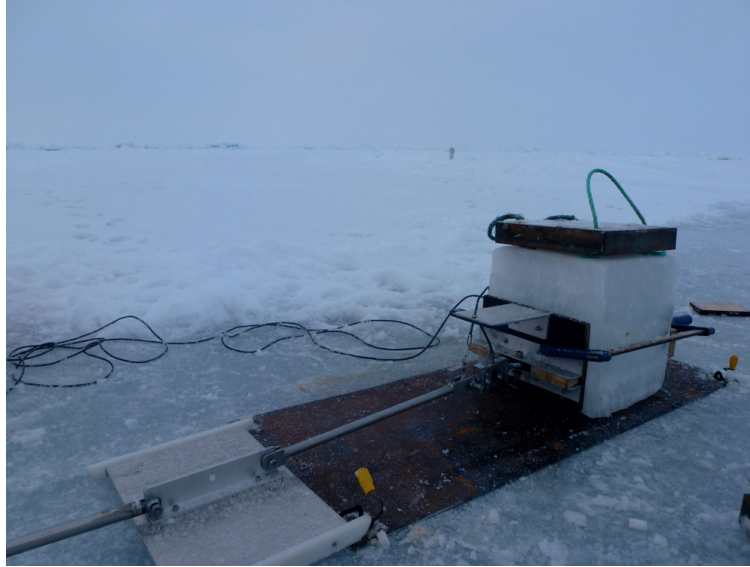


Figure 3.20. Test arrangement used in the friction test between steel and sea ice in “dry” conditions.

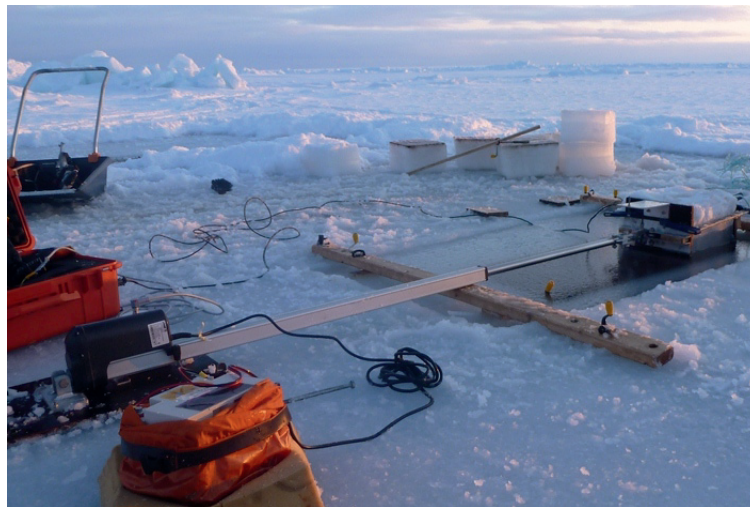


Figure 3.21. Test arrangement used in the friction test between steel and sea ice in “wet” conditions.

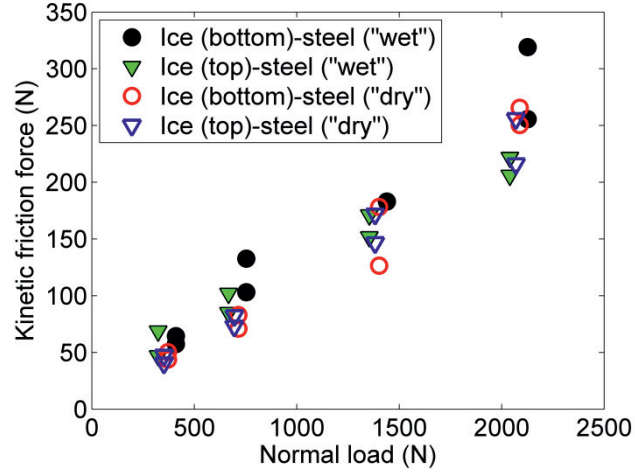


Figure 3.22. Kinetic friction force versus normal load in “wet” and “dry” ice-steel friction tests. The experimental parameters are listed in Table 3.5.

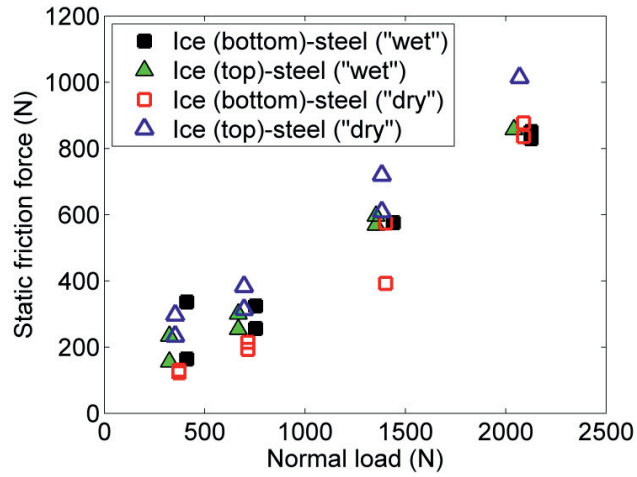


Figure 3.23. Static friction force versus normal load in “wet” and “dry” ice-steel friction tests. The experimental parameters are listed Table 3.5.

Table 3.5. Experimental parameters in ice-steel friction tests where the effect of the normal load on the static and kinetic friction coefficients was studied. The normal load ranged between 300 N and 2100 N.

Set no.	Sliding Configuration	Surface condition	$S_a$ (m <sup>2</sup> )	$T_{air}$ (°C)	$T_{ice\ block}$ (°C)	$T_{track}$ (°C)	$v$ (mm s <sup>-1</sup> )
Nd1	Bottom-steel	Dry	0.094	-9.8	-7.6	-	37.7 ± 1.4
Nd2	Bottom-steel	Wet	0.128	-11.6	-1.8	-1.8	38.7 ± 2.0
Nd3	Top-steel	Dry	0.107	-11.3	-7.6	-	38.2 ± 2.2
Nd4	Top-steel	Wet	0.098	-11.3	-1.8	-1.8	38.3 ± 1.5

Table 3.6. Static and kinetic friction coefficients obtained in the ice-steel friction tests. Experimental parameters are listed in Table 3.5.

Set no.	Sliding configuration	Surface condition	$\mu_{st}$	$\mu_k$
Nd1	Bottom-steel	Dry	0.43 ± 0.09	0.12 ± 0.03
Nd2	Bottom-steel	Wet	0.36 ± 0.09	0.13 ± 0.04
Nd3	Top-steel	Dry	0.50 ± 0.12	0.11 ± 0.02
Nd4	Top-steel	Wet	0.40 ± 0.05	0.09 ± 0.02

### 3.5 Discussion

The decrease in the kinetic friction coefficient observed in the tests when the ice blocks repeatedly slid over the same corresponding ice tracks (see Figure 3.10) can be related to the changes in the contacting surfaces. Initially, rough natural ice block and level ice surfaces become smoother during the sliding process because of an improvement with sliding in the alignment of the opposing faces, partial fracturing of the interlocking asperities and surface melting. The biggest change in the ice surface roughness (and in the friction coefficient) occurs during several first runs. The possible explanation could be that owing to macroscopic topography natural surfaces of sea ice fit together rather poorly until they have been run in, such that the resistance to initial sliding is caused mostly by ploughing. In subsequent runs smoothing takes place and thus the kinetic friction coefficient does not change significantly and finally reaches a constant value. In our tests, the measurements of the ice surface roughness were not systematic, and therefore, we could not correlate them to the kinetic friction coefficients. In the future, field tests should be performed to study more carefully this dependence. In natural conditions during rafting, ridge build-up, and ice floe interactions, the roughness of the ice surfaces changes continuously. The effect of the roughness with different materials sliding on ice has been investigated experimentally in numerous studies (Calabrese et al., 1980; Forland and Tatinclaux, 1985; Kietzig et al., 2009; Saeki et al., 1986; Tusima and Tabata, 1979). Generally, the kinetic friction coefficient was found to increase with an increase in the material surface roughness.

Fewer studies have investigated the effect of the surface roughness when ice is sliding on ice. In most of the laboratory experiments, the ice surfaces were polished prior to testing (Kennedy et al., 2000; Maeno and Arakawa, 2004). The role of roughness ( $R_a$ ) on the friction coefficient was analysed by Schulson and Fortt (2012). They combined the data obtained for sufficiently smooth ice surfaces ( $R_a = 0.4\text{-}10\ \mu\text{m}$ ) with the data obtained earlier by Fortt and Schulson (2009) for sliding across Coulombic shear faults in freshwater ice ( $R_a = 1.31 \pm 0.27\ \text{mm}$ ) at a temperature of  $-10^\circ\text{C}$  and a sliding velocity of  $10^{-4}\ \text{m s}^{-1}$ . The friction coefficient was found to be proportional to  $R_a^{0.08}$ . The authors also concluded that the roughness did not change significantly upon sliding, which contradicts our results (see Figure 3.10). One possible explanation is that in Schulson and Fortt (2012) and Fortt and Schulson (2009), sliding over a few millimetres were conducted, while in our case, the sliding distance was up to 1 m, and thus allowing for a more surface smoothing/changes. The sliding on the weak skeleton layer in the field tests might be another reason for the observed differences. Furthermore there was a difference in normal stress in our tests (which ranged between 2.0 kPa and 4.2 kPa) and tests performed by Schulson and Fortt (2012), where the normal stress ranged between 29 kPa and 40 kPa.

The changes in the kinetic friction coefficient, observed in test sets Rs1-Rs4 (see Figure 3.10 and Table 1), were different. It is hard to find any explanation for such differences because similar experimental parameters were used in all test sets (except Rs3). Consideration of the two test sets Rs1 and Rs3 reveal significant difference in the effect of run number on the friction coefficient. It should be noted that test set Rs1 was performed in the Barents Sea on relatively flat level ice, while in test set Rs3, which was done in the Van Mijenfjord, the sliding occurred on an ice track exhibiting a wavy surface (with the wave length of about 20 mm and an amplitude that ranged between 3 mm and 5 mm). The real contact area in test set Rs3 was smaller than in test set Rs1 due to waviness of the ice track. Therefore, in test set Rs3 the normal pressure in the contact spots was higher, and hence, more frictional heat was generated. The frictional heat increases the temperature of the ice and might produce melt water at the interface, and therefore, lead to quicker decrease in kinetic friction coefficient with run number. Alternative explanation is that heated ice has lower hardness, and therefore, abrasion of the surface asperities occurs faster.

#### *Effect of sliding velocity on the kinetic friction coefficient*

The effect of the sliding velocity on the kinetic friction coefficient depends on the velocity range and temperature. At very low sliding velocities, the ice friction is creep controlled and exhibits velocity strengthening. At high velocities, the friction exhibits velocity weakening, which is attributed to the melting in the sliding interface (Kennedy et al., 2000; Schulson and Fortt, 2012). All of our tests were performed in the velocity weakening regime ( $5\ \text{mm s}^{-1}$  to  $110\ \text{mm s}^{-1}$ ) and were therefore predicted by the frictional models (Akkok et al., 1987; Evans et al., 1976; Oksanen and Keinonen, 1982). The dependence of the kinetic friction coefficient on the sliding velocity was expected. Nevertheless, we observed that when sliding occurs between natural unsmoothed ice surfaces, the kinetic friction coefficient did not depend on the velocity. As the surfaces became smoother, the friction coefficient started to depend on the velocity in the

manner predicted by the friction models, i.e.,  $\mu \sim v^{-0.5}$ . Thus, existing models must be corrected to describe the friction between natural surfaces. Pritchard et al. (2012) found very little or no effect of the sliding velocity (up to  $40 \text{ mm s}^{-1}$ ) on the friction coefficient in the field tests of sea ice on sea ice. Similar conclusions were made by Ryvlin (1973) and Gavrilov (1984).

### Effect of the normal load

There are two common ways to report the effect of the normal load on the friction coefficient. The first way is to calculate the friction coefficient using Eq. (3.1) and to plot it versus the normal load. The second way is to present the dependence between the friction force (shear stress) and normal load (normal pressure), as was performed in the current work. In this case, the friction coefficient can be defined as the slope of the frictional force-normal load curve, i.e.,  $\mu_t = \Delta F / \Delta F_n$ , which is sometimes called the true friction coefficient (Tatinclaux, 1989). In most of the reported tests, the frictional force is a linear function of the normal load (Fortt and Schulson, 2009; Liukkonen, 1988; Schulson and Fortt, 2012; Tatinclaux, 1989; Tatinclaux and Murdey, 1985; Tusima and Tabata, 1979), and therefore, the true friction coefficient is independent of the normal load. However, the kinetic friction coefficient calculated with Eq. (3.1) might depend on the normal load. This dependence occurs if the free term  $F_o$  in the linear relationship between the frictional force and normal load, Eq. (3.2), is not zero. In this case, the friction coefficient is defined as  $\mu = \mu_t + F_o / F_n$ . For positive  $F_o$  and low normal loads, the friction coefficient  $\mu$  is higher than the real friction coefficient  $\mu_t$ . The difference between  $\mu$  and  $\mu_t$  disappears with an increase in the normal load. Tusima and Tabata (1979) studied the friction between sea ice and numerous metals, plastics, and coatings and found that in most cases, the initial cohesion force  $F_o$  was equal to or almost equal to zero, and therefore, the friction coefficient did not depend on the normal load. The friction model proposed by Oksanen and Keinonen (1982) predicts  $\mu \sim F_n^{-1/4}$  for partial contact and  $\mu \sim F_n^{-1}$  for full contact. Nevertheless, their lab tests showed that the data fit better if the power of the normal load is in the range between  $-1/2$  and  $-1/4$ . Akkoc et al. (1987) performed a regression analysis of their data on ice-steel friction and found considerable scatter in the load dependence. Their overall results showed that  $\mu \sim F_n^{-1/2}$ . Tatinclaux (1989) re-analysed the data from several papers (including Oksanen and Keinonen, 1982), in which the friction coefficient was found to be proportional to the power function of the normal load, and he concluded that even in this case, the frictional force was still linearly related to the normal load. He also noted that for most of the reported ice friction tests, the free term  $F_o$  (see Eq. (3.2)) is comparable with the measurement error. In our tests on the friction of sea ice on sea ice,  $F_o$  was  $54.6 \text{ N}$  and  $-31.5 \text{ N}$  in the “dry” and “wet” friction tests (kinetic friction dependence), respectively, which significantly exceed the sensitivity of the load cells. A negative value for the free term does not have a physical meaning. The scatter in our data might be the reason for the non-zero free term  $F_o$  in Eq. (3.2).

**Effect of temperature on the kinetic friction coefficient**

Temperature is one of the most important parameters that affects the friction regime (Kennedy et al., 2000; Oksanen and Keinonen, 1982). The data obtained in our tests are significantly scattered, and therefore, the temperature dependence is unclear. Both very high and low friction coefficients are observed for all tested temperatures. The scatter in the data might be attributed to the different surface roughness in the different tests. The results from the laboratory tests showed that the friction coefficient increases with a decrease in the temperature (Akkok et al., 1987; Fortt and Schulson, 2011; Kennedy et al., 2000; Marmo et al., 2005; Oksanen and Keinonen, 1982; Schulson and Fortt, 2012). The friction models predict a linear dependence of the friction coefficient on the temperature difference,  $\Delta T$ , between the bulk temperature of the ice block and the temperature in the sliding interface (melting or softening temperature). Akkok et al. (1987) performed a regression analysis of the data obtain in laboratory tests, where ice slid on steel, glass, and nylon, and found that the experimental temperature dependence is better described when  $\mu \sim \Delta T^{0.75}$ . The dependence was explained by the decrease in the hardness of the ice with increasing temperature (Barnes et al., 1971; Butkovich, 1958). Calabrese et al. (1980) observed in ice-steel friction tests a slight decrease in the friction coefficient as the temperature increased from  $-25^{\circ}\text{C}$  to  $-8^{\circ}\text{C}$ . As the temperature continued to increase to  $0^{\circ}\text{C}$ , the friction coefficient decreased sharply.

**Static friction coefficient and its dependence on the hold time**

To initiate sliding of an ice block resting on a sliding track, the static friction force has to be overcome. Calabrese et al. (1980) presented their results from the ice-steel friction tests and suggested distinguishing the static and breakaway friction coefficients. The difference between these two friction coefficients is the duration of the stationary contact before the test is run. In breakaway friction tests, the specimen remained in contact with the sliding track under a normal load for a specific length of time (hold time), while static friction was obtained after “very short” stationary contact. In this paper, we did not separate these two friction coefficients and used the unified static friction term. Figure 3.19 shows that the static friction coefficient increases with the hold time. Similar behaviour was recently reported by Lishman et al. (2011) and Schulson and Fortt (2013), who performed experiments both on sea ice and freshwater ice at  $-10^{\circ}\text{C}$ . Considering our data sets, we obtained the following equation for the fit curve:

$$\mu_{st} = 0.193 \log_{10} t + 0.565, \quad (3.3)$$

with a coefficient of determination  $R^2 = 0.43$ . Our tests were performed at the following experimental parameters: normal pressures were between 3.6 kPa and 4.8 kPa, the air temperature was between  $-6.9^{\circ}\text{C}$  and  $-18^{\circ}\text{C}$ , the actuator pulling velocity was approximately  $4 \times 10^{-2} \text{ m s}^{-1}$ , and the hold time ranged from 5 s to 960 s. Lishman et al. (2011) reported the results from both ice basin tests and laboratory tests. The basin test was performed at a normal load of 10 kPa, a pushing rate of  $8 \times 10^{-3} \text{ m s}^{-1}$ , and hold times of 10 s, 100 s, and 1,000 s and showed the following fit relation between the static friction coefficient and hold time:  $\mu_{st} = 0.48 \log_{10} t + 0.394$ , with  $R^2 = 0.48$  (Lishman et

al., 2009). The tests performed in the lab at a normal load of 50 kPa and a pushing rate of  $10^{-4} \text{ m s}^{-1}$  showed that the static friction coefficient increased faster with time than in the ice basin tests. Schulson and Fortt (2013) performed a laboratory test with the sliding velocity ranging from  $10^{-6} \text{ m s}^{-1}$  to  $10^{-4} \text{ m s}^{-1}$  and the holding time from 1 s to  $10^4$  s under a normal stress of 60 kPa. The authors found that an increase in the static friction coefficient with time can be described by the expression  $\mu_{st} = 0.30 \log_{10} t + \mu_k$ , where  $\mu_k$  is the kinetic friction coefficient at the corresponding sliding velocity. Schulson and Fortt (2013) presented a model that explains the static friction behaviour observed in the tests. The authors considered the interaction of asperities that protrude from the opposing surface and attributed frictional resistance to adhesion, deformation, and the rupture of the points in contact.

A comparison of our data with the data reported by Lishman et al. (2011) and Schulson and Fortt (2013) demonstrates that the coefficient in front of the logarithm in the fit equations is the lowest in our tests (0.193) and the highest in the laboratory tests performed by Lishman et al. (2011). The difference in the dependences might be related to the difference in the experimental setups and ice surface conditions.

## 3.6 Investigations of the contact area and ice surface roughness

### 3.6.1 Introduction

It is well known that when sliding occurs between two solids, only a small part of the apparent contact area is in contact due to surface roughness (Hatton et al., 2009; Makkonen, 2012; Persson, 2000). The contacts may occur on many different scales, from the millimetre scale to atomic dimensions. According to Makkonen (2012), in any theoretical treatment of friction, it is necessary to define precisely the term contact and its scale. Persson (2000) stated that in most practical applications, the diameters of the contact areas (junctions) are on the order of  $\sim 10 \text{ }\mu\text{m}$ . Nevertheless, the development of micro- and nano-technologies formulates new challenges and problems related to friction, where nano-scale junctions should be taken into account. The physical processes underlying the formation and behaviour of nano-scale junctions are quite different from the ones underlying micro-scale junctions (Persson, 2000). In this thesis, we will not address the topic of nano-scale level processes but will refer readers to Persson (2000) and Makkonen (2012). At the micro-scale, the surface asperities of the two bodies are first brought into contact, then deform in compression until the real contact area can support the normal load, and then a shear force is applied to initiate the sliding (Hatton et al., 2009; Lishman and Sammonds, 2013).

The existing ice friction models (presented in Section 2.2.1) require that the real contact area and the amount, distribution, and size of the contact areas be known. The measurement of these parameters is problematic, as the friction process is dynamic. Very often, people do not measure the real contact area characteristics but use them as turning parameters to fit the model with experimental data.



A number of different techniques have been used to characterise the real contacts between ice and various materials (including ice) (Bäurle, 2006; Hatton et al., 2009; Kennedy et al., 2000; Schulson and Fortt, 2012). The most common way to characterise an ice surface is to produce a cast of the surface and then analyse it using an optical profilometer. Baurle et al. (2007) used electron microscopy X-ray computer tomography to investigate the contact area between polyethylene and snow. However, it is very difficult to use these techniques in field tests.

Here, we present our attempts to characterise real contact area characteristics in field conditions.

### 3.6.2 Experimental methods

To obtain an idea of the level of ice surface roughness and the size of the unit contact area, two different experimental techniques were used. The first technique was used to characterise the pressure distribution, real contact area and unit contact area. For this purpose, tactile sensors were used. An I-Scan system was used to measure the pressure distribution, real contact area and a size of unit contact between an ice block and a smooth rubber mat. The system is comprised of Microsoft Windows – based software, the associated data acquisition hardware, and a thin tactile sensor. The sensors use a resistive-based technology. The application of pressure to an active sensor results in a change in the resistance of the sensing element in inverse proportion to the pressure applied.

Two sensor models were used in the tests, 5513 and 5027. The tactile pressure sensor 5513 has a sensitive area with horizontal dimensions of 416.1 mm and 156.5 mm. The sensor has 2288 sensing elements (sensels) with horizontal dimensions of 5.6 mm and 1.8 mm. Another tactile sensor, 5027, has a smaller total sensitive area (equal horizontal sizes of 27.9 mm by 27.9 mm) and 1936 sensing elements with dimensions 0.2 mm by 0.2 mm. Before the sensors were used in the field tests, they were calibrated in the cold lab at a temperature of  $-5^{\circ}\text{C}$ . The sensitivity of the sensors was adjusted to the expected normal loads.

To measure the pressure distribution and real contact between an ice block and a flat surface, the following procedure was used (see Figure 3.24). A rubber mat with a smooth surface was put on top of the flat steel plate, which was resting on the level ice. A tactile sensor was placed between an ice block and the rubber mat. The ice block had horizontal dimensions of 13 cm and 30.5 cm and thus did not exceed the sensitive area of the sensor 5513. The pressure distribution and real contact area were measured with four normal loads. The measurements were performed first under increasing normal load levels and then in decreasing order. The same type of measurement with the same ice block was made using another sensor (5027). The sensitive area of the sensor was too small to cover the whole ice block surface, but it gave a more detailed spatial resolution of the pressure and unit contact size.

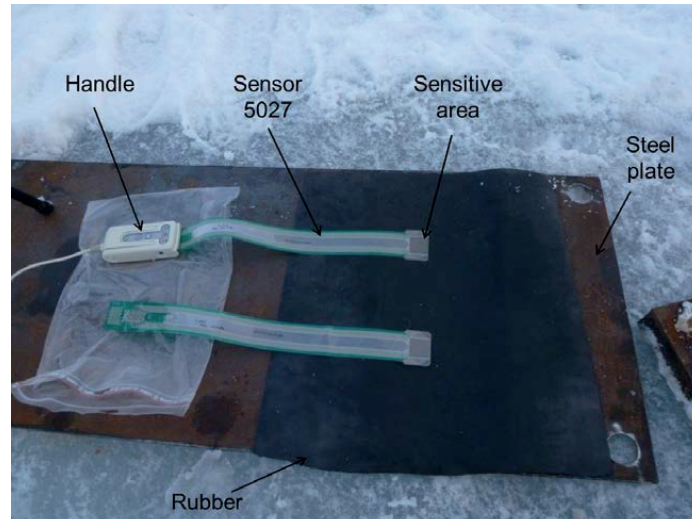


Figure 3.24. Tactile sensor 5027 and real contact area measurements in the field.

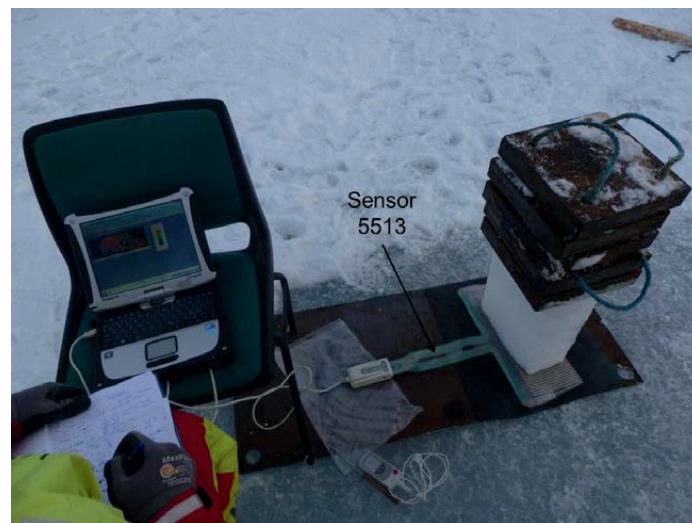


Figure 3.25. Real contact area measurements using sensor 5513.

The second technique was used to characterise ice surface roughness. Conventional methods of measuring surface roughness, such as stylus roughness measurements or non-contact surface roughness measurements using a laser illumination source and a multiple sensor detection system, cannot be applied to ice due to its low hardness and optical peculiarities, respectively. Therefore, a replica of the ice surface was obtained and then analysed in the lab. To prepare ice surface replicas in the field, we used a synthetic rubber replicating compound, 101RF fluid, produced by Microset. The

compound was applied to the ice surface area with a diameter of approximately 50 mm and then cured for 20 hours. The replica was then easily removed from the ice surface. The roughness of the replicas was measured by a 3D surface microscope InfiniteFocus at the SINTEF Tribology Laboratory.

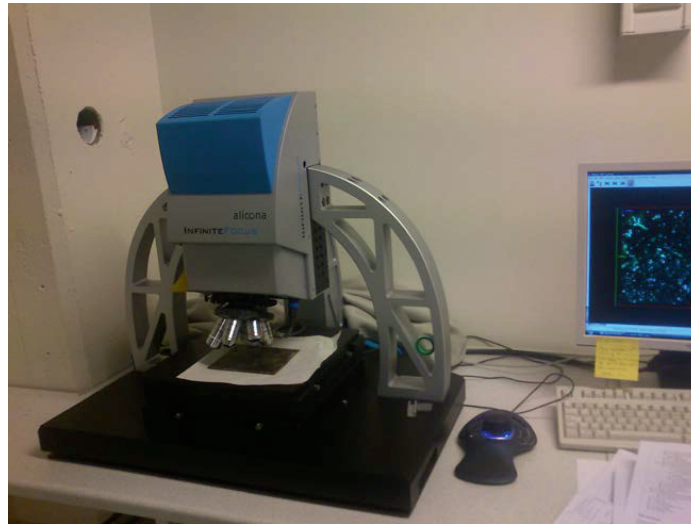


Figure 3.26. Surface microscope to study steel surface and casts of the ice surfaces.

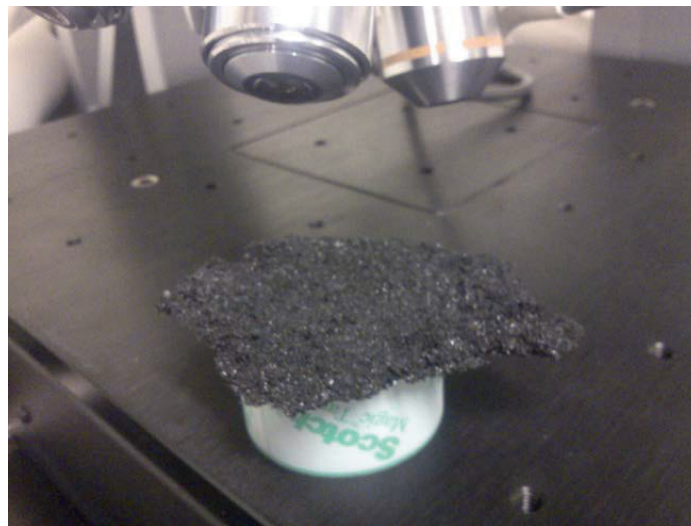


Figure 3.27. Replica of an ice surface during roughness measurements using an optical 3D surface microscope.

### 3.6.3 Results and discussion

Figure 3.28 shows the pressure distribution over the contact area measured using the tactile sensor 5513 (which covers the whole contact area but has quite large sensel dimensions). It was found that for the minimal normal load, 120 N (which is the weight of the ice block), the real contact covers only 14.7 % of the apparent contact area. The contacts occur in many contact spots whose size is equal to or smaller than the sensel size. The pressure at the contact spots is not the same at each junction. The real contact area increases with increasing normal load and is equal to 81 % of the apparent contact area when the maximum normal load is applied (1836 N). The pressure on the contact also increases, and according to our measurements, exceeds 46 kPa over significant parts of the contact. When the normal load decreases from a high value to lower one, the real contact area and pressure on the contact become lower. However, due to ice creep, the real contact areas measured in this case were slightly higher than in the tests with the same normal load before the increase. Figure 3.29 shows similar measurements performed using tactile sensor 5027 with a higher spatial resolution (sensel sizes 0.2 mm by 0.2 mm). Sensor 5027 does not cover the whole ice block contact area, and therefore the results will depend significantly on the location of the sensor. The contact spots obtained using this sensor have a smaller size (Figure 3.29). The real contact area also increases with an increasing normal load and decreases as the normal load decreases.

Figure 3.30 shows the normal load versus the real contact area related to the apparent contact area for both sensors. The same ice block was used in the tests. First, the load was gradually increased from the lowest value to the maximum value and then decreased down to the initial value (weight of the ice block). Hysteresis was observed, which is partly related to the creep of the ice contact spots. The rest of the hysteresis is related to sensor error. The black arrows in Figure 3.30 show the results of the measurements. The real pressure at the contact junctions obtained using sensor 5027 was lower than the real pressure measured in tests using sensor 5513. The difference could be explained by the difference in calibration, which is crucial for such measurements. The real contact areas related to the apparent contact area found in our tests are likely higher than the real contact area when the ice block is placed or sliding on level ice. It is related to the difference in ice and rubber hardness. The calibration of the tactile sensors also influences the values for the real contact area obtained in the tests. Therefore, more careful investigations with different underlying materials (e.g., glass, steel, wood) should be performed.

Table 3.7 presents the results of the ice roughness measurements using the replication technique and an optical 3D surface microscope. It should be noted that due to the relatively high roughness of the replicas of the ice surfaces and the relatively small area of the measurements (2.84 mm × 2.15 mm), the measurements are not very reliable. Nevertheless, it gives us certain idea regarding the range of ice surface roughnesses in natural conditions. The natural (unsmoothed) roughness of the skeleton layer (at the bottom of the level ice) was not measured in our tests, but normally has higher values than are presented in Table 3.7.

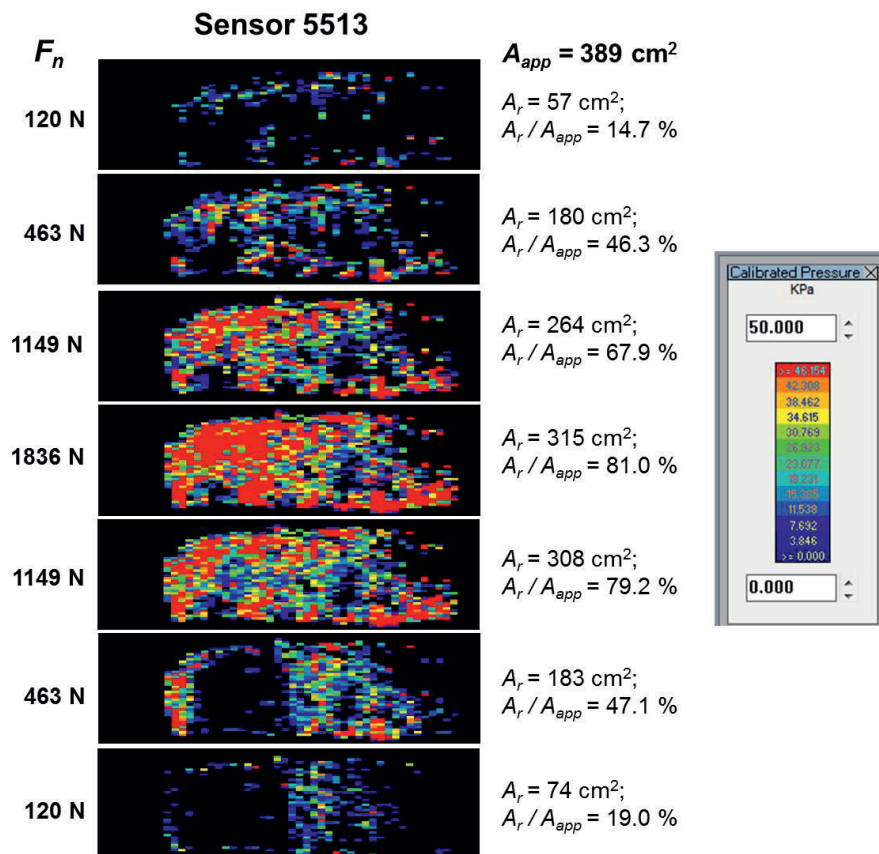


Figure 3.28. Pressure distribution in the contact between ice and flat rubber surface. The measurements were performed using tactile sensor 5513.

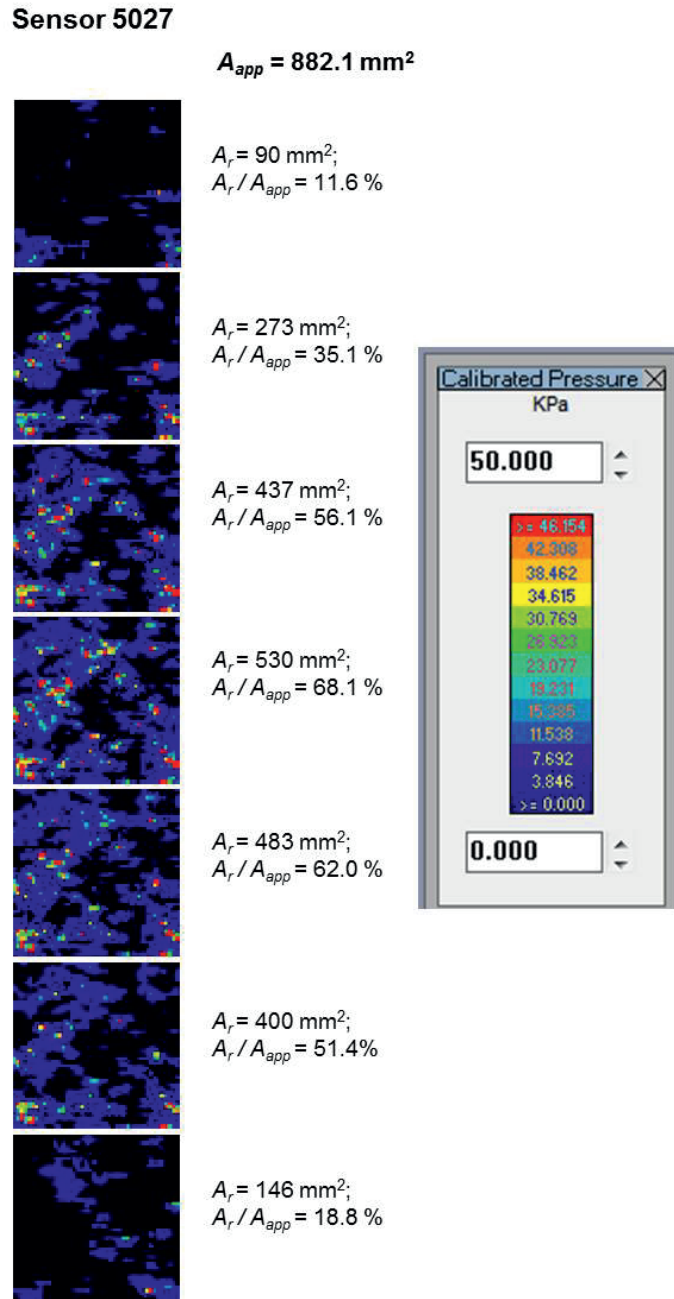


Figure 3.29. Pressure distribution in the contact between ice and flat rubber surface. The measurements were performed using tactile sensor 5027.

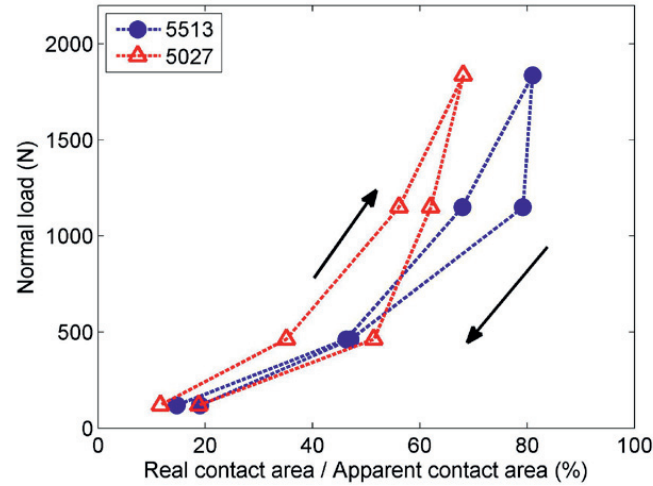


Figure 3.30. Applied normal load versus real contact area related to the apparent contact area ( $A_r/A_{app}$ ). The tests were performed at  $T_{air} = -10^\circ\text{C}$ . The bottom surface of the ice block (i.e., the surface with the skeleton layer) was a contact surface and had the temperature  $T_{ice\ surface} = -7.1^\circ\text{C}$ . The black arrows show the sequence of the data points obtained in the tests.

Table 3.7. Ice surface roughness measurements using optical 3D microscope and casts of the different ice surfaces.

Sample name	Ra ( $\mu\text{m}$ )	Rq ( $\mu\text{m}$ )	Short description
Ice R1-1	$202.4 \pm 17.3$	$307.8 \pm 20.15$	natural top surface of the level ice
Ice 1R-2	$179.1 \pm 2.3$	$260.0 \pm 2.6$	natural top surface of the level ice
Ice 2R	$103.3 \pm 2.4$	$121.0 \pm 1.5$	ice track surface after 5 runs
Ice 4R	$98.4 \pm 2.3$	$115.3 \pm 3.2$	ice block bottom surface (skeleton layer) after 5 runs
Ice 5R	$50.6 \pm 3.7$	$65.7 \pm 4.9$	ice block bottom surface (skeleton layer) after 5 runs
Ice 6R-1	$65.55 \pm 1.7$	$79.81 \pm 1.8$	ice block bottom surface (skeleton layer) after 5 runs
Ice 6R-2	$82.4 \pm 1.5$	$95.01 \pm 0.9$	ice block bottom surface (skeleton layer) after 5 runs
Ice 7R	$80.8 \pm 14.6$	$108.3 \pm 13.5$	top surface of the ice block

Figure 3.31 shows image of the ice surface replica obtained using an optical 3D microscope.

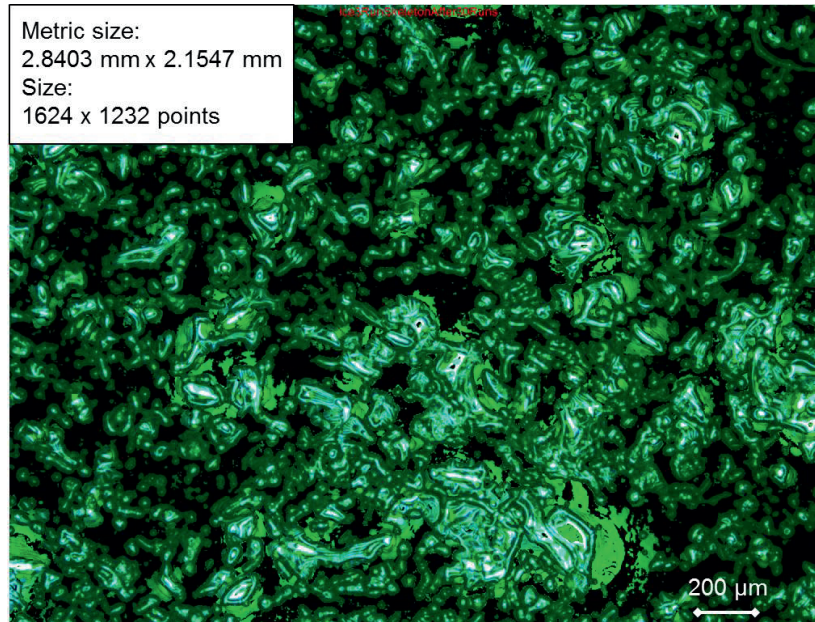


Figure 3.31. Image of the ice surface replica obtained using an optical 3D microscope.

### 3.7 Summary

A number of field tests on the friction of sea ice on sea ice were performed. They highlighted the effects of the sliding velocity, air and ice track temperatures, normal load, presence of sea water in the interface, and ice grain orientation with respect to the sliding direction on the friction coefficient. Measurements of the ice surface roughness, real contact area and pressure distribution in the contact were performed. The main findings can be summarised as follows:

- 1) Ice surface roughness is an important parameter that determines the value of the friction coefficient. Repeated sliding over the same track led to surface polishing and decreased the kinetic friction coefficient from 0.48 to 0.05 in the most extreme case.
- 2) The velocity dependence of the kinetic friction coefficient predicted by the existing friction models does not work when sliding occurs between natural ice surfaces. In this case, the friction coefficient was found to be independent of the sliding velocity ( $6 \text{ mm s}^{-1}$  to  $105 \text{ mm s}^{-1}$ ). As the contacting surfaces became smoother, the kinetic friction coefficient started to depend on the velocity, as predicted by existing ice friction models.
- 3) The frictional force (both static and dynamic) was linearly related to the normal load.



- 4) The presence of sea water in the sliding interface has very little effect on the static and kinetic friction coefficients.
- 5) The static friction coefficient logarithmically increases with the hold time, from approximately 0.6 at 5 s to 1.26 at 960 s.



# Chapter 4

## 4 Geometrical stick-slip between ice and steel

### 4.1 Introduction

Ice friction is a very complex phenomenon that depends on a number of parameters: velocity, temperature, normal load, thermal properties of the sliding material, relative humidity, apparent contact area and surface roughness (Kietzig et al., 2010). Numerous studies have been performed to investigate the effect of these parameters on the friction coefficient (Evans et al., 1976; Forland and Tatinclaux, 1985; Frederking and Barker, 2002; Hatton et al., 2009; Lishman et al., 2011; Lishman et al., 2013; Maeno and Arakawa, 2004; Marmo et al., 2005; Oksanen and Keinonen, 1982; Saeki et al., 1986; Schulson and Fortt, 2012; Tabata and Tusima, 1981). If sliding occurs between materials with different hardnesses, as in the ice-steel interaction, harder surface asperities will plough out the softer material (Bowden and Tabor, 2001). The total friction force in this case can be expressed as the sum of two components: the force required to shear the junctions formed at the contact points between materials and the ploughing force. It is understood that surface roughness has a great effect on the ploughing component. The effect of material surface roughness on the ice friction coefficient has been studied by many authors. Tusima and Tabata (1979) observed that in ice friction tests with rough stainless steel, the friction coefficient was 4 - 10 times larger than that in tests with smooth surfaces. An increase in the friction coefficient with material surface roughness was also reported by Saeki et al. (1986), Forland and Tatinclaux (1985), Tatinclaux and Murdey (1985), Nakazawa et al. (1993) and Frederking and Barker (2002).

Kietzig et al. (2009) studied the effect of controlled surface roughness on the friction between ice and steel. The authors used femtosecond laser irradiation to change an initially hydrophilic stainless steel surface to a hydrophobic surface with controlled dual-scale roughness. Kietzig et al. (2009) observed that controlled roughness increases the coefficient of friction at low sliding speeds and low temperatures, whereas at temperatures close to the melting point of ice and relatively high speeds, roughness and hydrophobicity significantly reduce ice friction. The authors explained the decrease in friction by the suppression of capillary bridges between surface asperities. Kietzig et al. (2009) also observed that grooves oriented in the sliding direction also reduce friction at low velocities compared to scratches and grooves randomly distributed over a surface.

Two regimes of sliding might be observed in friction tests: steady motion and stick-slip motion, which denotes the situation in which the sliding body alternates between stick and slip. The manifestation of either regime depends on the sliding velocity and overall elastic properties of the sliding body. According to Persson (2000), one fundamental problem in sliding friction is mapping out the dynamic phase diagram (in the stiffness -

velocity plane) over which steady and stick-slip motion occur and determining the nature of the transitions between stick-slip and steady sliding. A number of authors have observed stick-slip motion in ice friction tests under certain conditions (Frederking and Barker, 2002; Lishman et al., 2011; Maeno et al., 2003; Pritchard et al., 2012; Rist, 1997; Sammonds et al., 2005; Sammonds et al., 1998; Schulson and Fortt, 2012; Tusima and Tabata, 1979). Maeno et al. (2003) performed ice-ice friction tests with very smooth contacting surfaces to eliminate the effects of ploughing and surface abrasion. The authors observed that stick-slip occurred for sliding velocities ranging between  $10^{-5} \text{ m s}^{-1}$  and  $10^{-3} \text{ m s}^{-1}$ . Lishman et al. (2009) observed stick-slip in ice-ice friction tests performed in the Hamburg Ice Basin (HSVA) at a sliding velocity of  $2.8 \times 10^{-3} \text{ m s}^{-1}$ . Sammonds et al. (2005) observed stick-slip in coarse-grained freshwater ice and sea ice but not in fine-grained freshwater ice under the same conditions. This finding indicates that the interactions between surface asperities play an important role during stick-slip.

In this paper, we present the results obtained from small-scale laboratory tests in which the stick-slip interactions between ice and stainless steel were investigated. The origin of the stick-slip oscillations in our tests was closely related to the interaction of regular asperities produced on a steel surface with ice and was therefore different from the stick-slip observed in tests involving smooth surfaces reported previously in the literature. We use the term “geometrical” stick-slip here to emphasise the difference. In this work, we studied the effects of surface roughness, sliding rate and temperature on the ice-steel interaction. Concentrations of the local pressure at the ice-steel interface were estimated using the Hertz contact problem. The results of this work and further investigations may be useful in achieving increased understanding of ice-induced vibrations.

## 4.2 Experimental setup and test procedure

The experimental setup was initially developed by Nanetti et al. (2008) and modified by the author. Figure 4.1 shows the two types of experimental samples used in the tests. The first sample type was used for “ice slide tests” and consisted of a hollow steel (AISI303) cylinder with an inner diameter of 50 mm and a height of 95 mm, with ice frozen inside the cylinder. The sample was mounted on a cylindrical steel base with a circular hole, the diameter of which was slightly larger than the inner diameter of the hollow cylinder. In the “ice slide tests”, the ice was pushed out of the hollow cylinder toward the base. The second sample type was used for “piston slide tests” and consisted of a hollow steel cylinder, a coaxially located steel piston with a diameter of 15 mm and a height of 125 mm and ice grown in the annulus between the piston and the cylinder. The sample was mounted on a base with a hole, the diameter of which was slightly larger than the diameter of the piston. During testing, the piston head was pushed toward the base to create relative sliding between the piston and ice. Similar test configurations were used by Haehnel and Mulherin (1998) and Goldshtein and Epifanov (2012) to measure the adhesive strengths between ice and various materials and coatings.

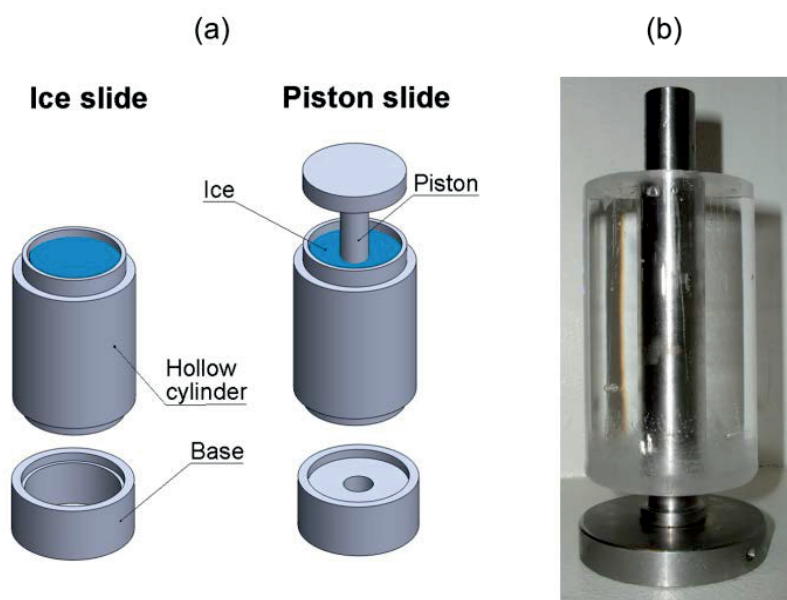


Figure 4.1. (a) Sketch of the samples and bases used in the “ice slide tests” and “piston slide tests”; (b) piston and ice extracted from a hollow cylinder after completing the “piston slide test”.

The inner surface of the cylinder and piston surface were worked using a lathe. Five pairs of pistons and cylinders with identical dimensions and different roughnesses were produced and labelled Sr, Mr, Hr, NHr and TBr. Sample Sr had the lowest roughness, and sample TBr had the highest roughness. Figure 4.4 shows the basic characteristics of the threading, and Table 4.1 presents the surface roughness characteristics measured using a SurfTest SJ301 stylus-type roughness measuring instrument (Figures 4.2-4.3). The roughnesses reported in Table 4.1 correspond to the stylus tracings along the long axes of the cylinders and pistons. The roughness profiles of the cylinders’ and pistons’ surfaces are shown in Figure 4.5, and the roughness measurements showed that the cylinder surfaces and the surfaces of the corresponding pistons in samples NHr and TBr possessed very similar roughness characteristics. Samples Mr and Hr possessed the same mean profile pitch ( $S_m$ ) in their cylinders and corresponding pistons, whereas the surface roughness depth ( $R_z$ ) and arithmetic mean surface roughness ( $R_a$ ) differed and were lower for the piston surfaces. Sample Sr exhibited a similar mean arithmetic roughness in its piston and the cylinder, but the piston surface showed more randomly distributed surface asperities without clear periodicity.



Figure 4.2. Portable surface roughness tester.

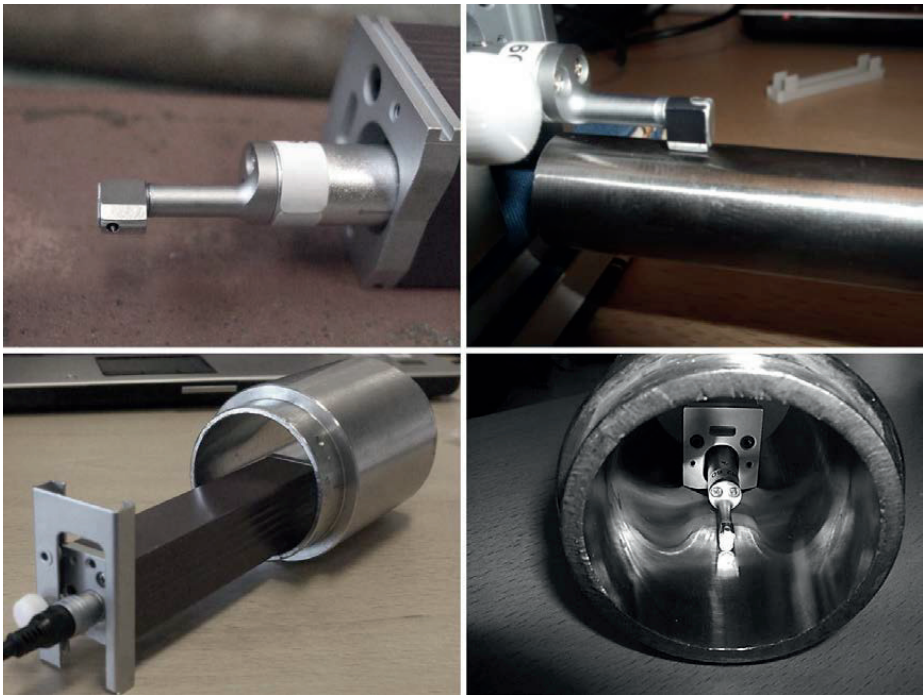


Figure 4.3. Roughness measurements of stainless steel piston and inner surface of the hollow cylinder.

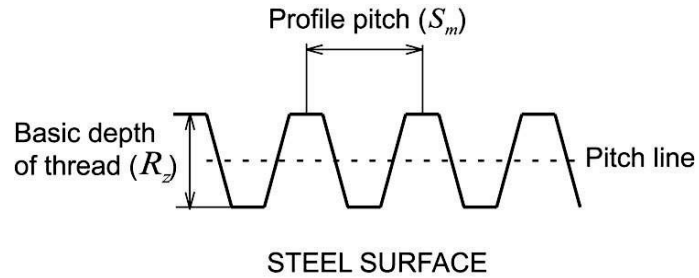


Figure 4.4. Basic characteristics of the threading on the steel surfaces.

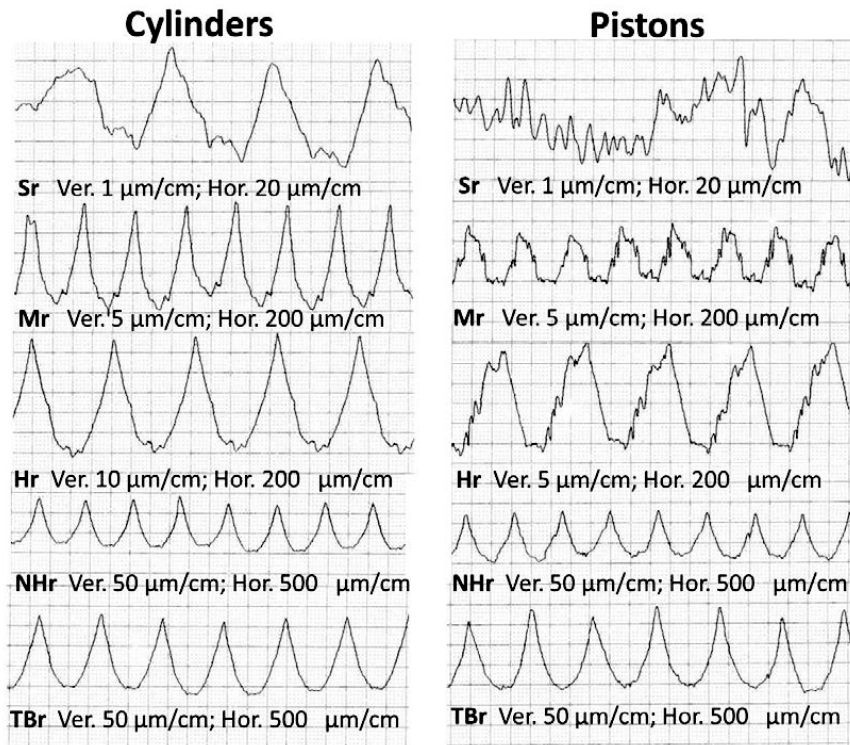


Figure 4.5. Axial profiles of the inner cylinder and piston surfaces. Note the difference in the vertical scale of the cylinder and piston roughness profiles for sample Hr.

Table 4.1. Roughness characteristics of the piston and inner cylinder surfaces:  $S_m$  is the mean profile pitch (screw pitch);  $R_z$  is the surface roughness depth (corresponding to the basic threading depth); and  $R_a$  is the arithmetic mean surface roughness. The roughnesses were measured along the long axes of the cylinders and pistons.

Sample name	$S_m$ (mm)	$R_z$ ( $\mu\text{m}$ )	$R_a$ ( $\mu\text{m}$ )	$S_m$ (mm)	$R_z$ ( $\mu\text{m}$ )	$R_a$ ( $\mu\text{m}$ )
	<i>Pistons</i>			<i>Cylinders</i>		
Sr	-	1.85	0.31	0.050	1.50	0.31
Mr	0.256	8.56	2.00	0.253	13.74	3.04
Hr	0.412	14.41	3.83	0.408	30.98	7.34
NHr	0.595	66.06	14.81	0.596	68.51	15.04
TBr	0.770	109.1	24.30	0.770	104.1	25.23

The tests were performed in a cold laboratory at the University Centre in Svalbard (UNIS). A deformation-controlled compression machine (KNEKKIS) was used to push the ice (in the “ice slide tests”) and piston (in the “piston slide tests”). The KNEKKIS is specially designed to perform uniaxial compression tests at a constant velocity (strength tests) and at a constant load (creep tests). The lower cylinder of the KNEKKIS moves upward, whereas the upper plate attached to the load cell does not move (Figure 4.6). The maximum achievable load when using the compression machine is 100 kN, and the capacity of the load cell used in the tests was 50 kN. Temporal variations in the force and displacement were measured and stored in a computer file. To perform the “ice slide tests”, an indenter with a circular cross-section and a diameter slightly smaller than the inner diameter of the hollow cylinder was attached to the upper plate of the KNEKKIS.

#### *Sample preparation procedure*

The following procedure was followed to prepare samples for the “piston slide tests”. The piston was placed coaxially to the hollow cylinder such that the bottoms of the piston and cylinder lay in the same plane. A holding frame was used to keep the piston in place during the ice formation process, and this frame was attached to the piston head and hollow cylinder with screws. The same frames attached to the cylinders were used to prepare samples for the ice slide tests. Each assembled sample was wrapped in a layer of polyethylene foam and then inserted into a piece of plastic pipe such that the holding frame was located outside of the pipe and foam (Figure 4.7). The distance between the bottom of the pipe and the bottom of the cylinder was 50 mm.

Samples containing freshwater ice and salty ice were used in the tests, and two different procedures were used to create the two sample types. To make freshwater ice, each sample was placed in a bucket filled with tap water (Figure 4.8(a)). The bottoms of the pipes rested at the bottom of the bucket, and the water level was approximately 5 mm below the tops of the pipes. Figure 4.8(b) shows the ice formation process for the samples containing salty ice. Each assembled sample was partially immersed in an ice tank with a depth of 1.2 m and horizontal dimensions of 0.5 m and 1 m; the ice tank was



filled with sea water with a salinity of 34 ppt that was taken from the Adventfjord. The samples were hung from wooden bars supported by the opposite walls of the tank. Three metal rings screwed to the outer surface and fishing line were used to hang the samples. The temperature in the laboratory was cooled to  $-20^{\circ}\text{C}$ , at which point ice was formed.

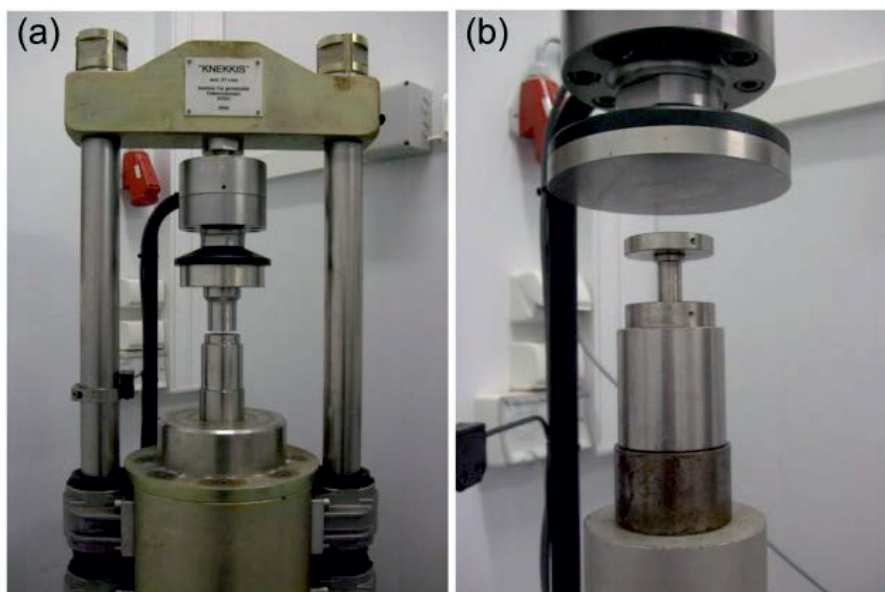


Figure 4.6. Uniaxial compression machine (KNEKKIS): (a) “ice slide test” and (b) “piston slide test”.

Due to the high thermal conductivity of stainless steel compared to that of ice and water, the formation of the ice began on the steel surfaces (i.e., the pistons and cylinders). During the ice formation process, the ice grew in the annulus from the piston and hollow cylinder surfaces. The freezing fronts “met” each other, and the interface between the fronts could be observed in the ice due to the presence of air bubbles in it (Figure 4.9).

When the required ice thickness was obtained, the samples were pulled out of the plastic pipes surrounded by ice. The wrapping mat was removed from each sample, and the excess ice that had formed below the bottom of the cylinder and the piston was cut off evenly with a band saw (Figure 4.10). Next, the holding frames were detached, and the samples were left in the cold laboratory for several hours at the desired test temperature to obtain a uniform temperature inside them. The sample preparation procedure for the “piston slide tests” (using freshwater ice) is summarised in Figure 4.11. Each sample was mounted on the corresponding base and placed into the KNEKKIS immediately before the test was started (Figure 4.6).

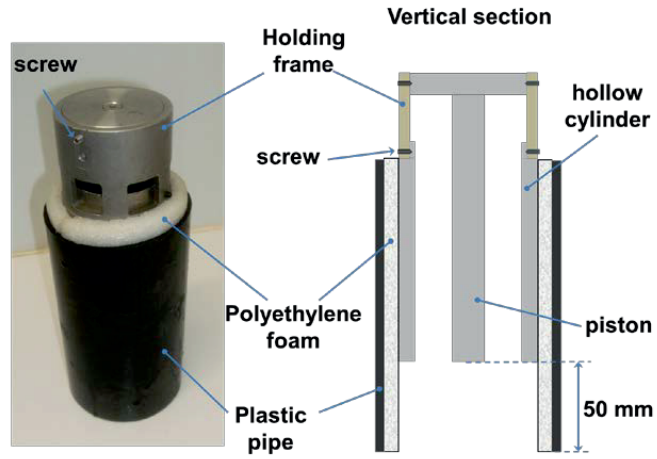


Figure 4.7. Sample before being submerged in water.



Figure 4.8. (a) Freshwater ice and (b) salty ice formation in the annulus between the piston and ice.



Figure 4.9. Ice formation in the annulus between the hollow cylinder and a coaxially located steel piston.



Figure 4.10. Samples containing salty ice after their extraction from the ice tank (left) and after the sawing process (right).

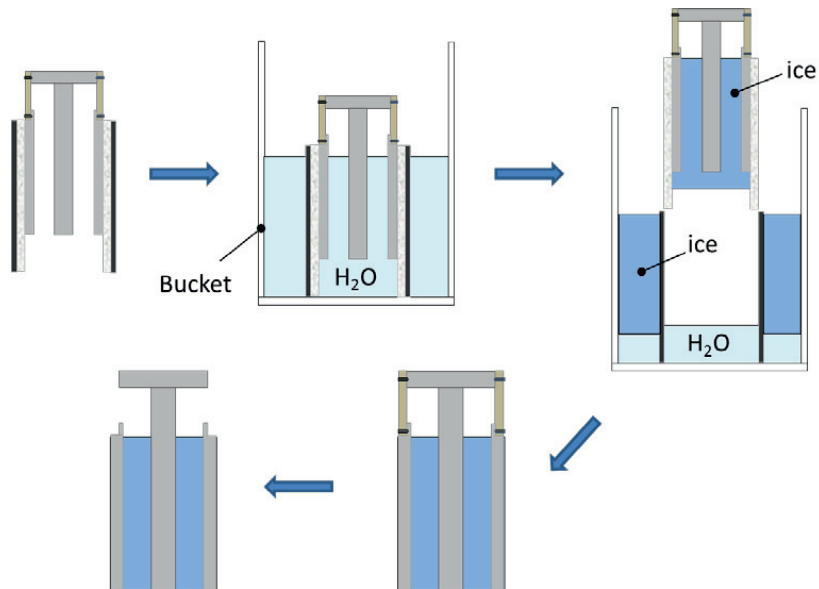


Figure 4.11. Summary of the sample preparation procedure for the “piston slide tests” (using freshwater ice).

Two types of tests, “Type I” and “Type II”, were performed. During the “Type I” tests, the KNEKKIS was programmed to maintain a constant piston (for the samples containing a piston) or ice (for the samples without a piston) displacement rate ranging from  $1.7 \times 10^{-6} \text{ m s}^{-1}$  to  $0.83 \times 10^{-3} \text{ m s}^{-1}$ . During the “Type II” tests, the KNEKKIS was programmed to maintain a constant load on the piston ranging from 1.2 kN to 32.5 kN. The applied load  $F_{\text{app}}$  varied in the samples with different roughnesses and was set to 25%, 50%, 75% or 90% of the first peak load  $F_{1\text{st peak}}$  measured in the “Type I” tests at a constant displacement rate of  $0.83 \times 10^{-4} \text{ m s}^{-1}$  for samples with the corresponding roughness. Summaries of the “Type I” and “Type II” tests are presented in Table 4.2 and Table 4.3, respectively.

Table 4.2. Summary of the “Type I” tests.

Test	Ice type	Salinity (ppt)	Displacement rate ( $\text{m s}^{-1}$ )	Temperature ( $^{\circ}\text{C}$ )	Samples	No. of tests
Piston slide	Salty	13.7	$1.67 \times 10^{-5}$ – $6.67 \times 10^{-5}$	-10, -15	Sr, Mr, Hr	9
Ice slide	Salty	$16.1 \pm 1.5$	$1.67 \times 10^{-5}$ – $2.0 \times 10^{-4}$	-10, -15	Sr, Mr, Hr	21
Piston slide	Freshwater	0	$1.67 \times 10^{-6}$ – $0.83 \times 10^{-3}$	-5, -10, -15, -20, -25	Sr, Mr, Hr, NHr, TBr	176
Ice slide	Freshwater	0	$1.67 \times 10^{-5}$ – $0.83 \times 10^{-4}$	-10, -15	Sr, Mr, Hr, NHr, TBr	19

Table 4.3. Summary of the “Type II” tests.

Test	Ice type	$F_{\text{app}} / F_{1\text{st peak}}$ (%) <sup>*</sup>	Temperature ( $^{\circ}\text{C}$ )	Samples	No. of tests
Piston slide	Freshwater	25	-15	NHr, TBr	2
Piston slide	Freshwater	50	-15	Sr, Mr, Hr, NHr, TBr	11
Piston slide	Freshwater	75	-15	Sr, Mr, Hr, NHr, TBr	10
Piston slide	Freshwater	90	-15	Sr, Mr, Hr, NHr, TBr	15

\*  $F_{\text{app}}$  is the applied load and  $F_{1\text{st peak}}$  is the first peak load obtained during the tests performed at a constant displacement rate ( $0.83 \times 10^{-4} \text{ m s}^{-1}$ ).  $F_{\text{app}}$  and  $F_{1\text{st peak}}$  differ in samples with different roughnesses.

## 4.3 Results and analysis

### 4.3.1 “Type I” tests

The “Type I” tests included “ice slide tests” and “piston slide tests” performed at a constant displacement rate. The ice slid relative to the hollow cylinder in the “ice slide tests”, while the piston slid relative to the ice in the “piston slide tests” (Figure 4.1). Samples containing freshwater ice and salty ice were used in the tests.

#### Ice slide tests

The “ice slide tests” were performed mainly on samples Sr, Mr and Hr. The results of the two tests performed on samples NHr and TBr, filled with freshwater ice, showed that the first peak load corresponding to the initiation of relative sliding between the ice and the cylinder exceeded the capacity of the load cell (50 kN). Figure 4.12 shows examples of the dependences between the load and displacement obtained in the tests on freshwater ice and salty ice ( $16.1 \pm 1.5$  ppt) samples. The load oscillations were registered in the tests on samples Mr and Hr. No load oscillations were detected in the tests on sample Sr (the sample with the lowest roughness). The measured loads were

significantly higher in the samples filled with freshwater ice than in those filled with salty ice, and the load in the tests on sample Sr filled with salty ice did not exceed 0.1 kN, which was comparable to the measurement accuracy. This result indicated that a different load cell with more appropriate accuracy should be used in future tests. The significantly lower force levels measured in the tests with salty ice could be explained by the presence of brine that may have acted as a lubricant in the ice-steel interface.

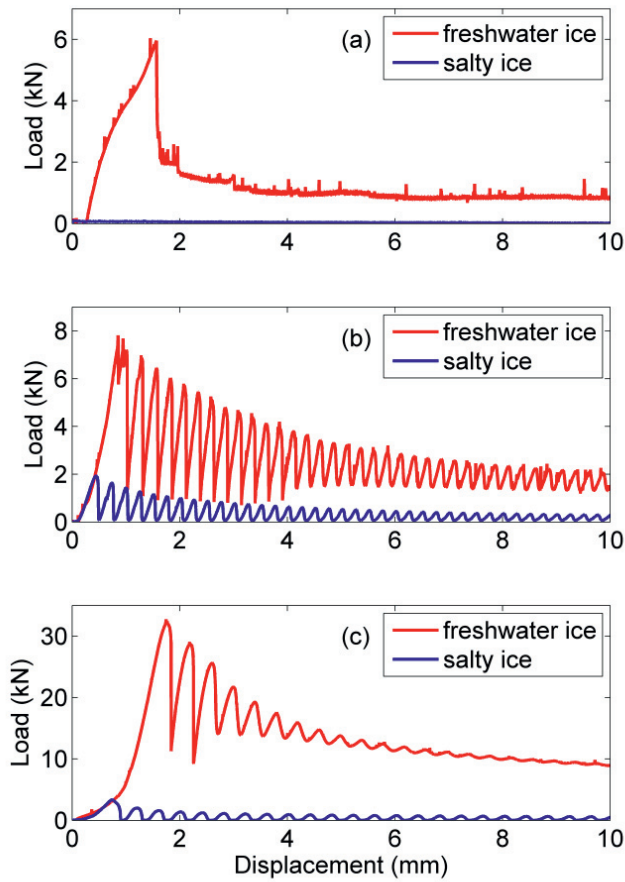


Figure 4.12. Load versus displacement profiles obtained during the “ice slide tests” of the following samples: (a) Sr, (b) Mr and (c) Hr. The displacement rate and temperature were  $1.67 \times 10^{-5} \text{ m s}^{-1}$  and  $-15^\circ\text{C}$ , respectively. Samples with freshwater ice and salty ice ( $16.1 \pm 1.5 \text{ ppt}$ ) were used in the tests.

Figure 4.13 shows the surface of the freshwater ice observed in sample Mr after testing. The ice surface was covered by asperities with similar shapes to those on the inner

cylinder surface. Similar observations were made in the tests performed on Hr samples filled with freshwater ice and salty ice. Unfortunately, the ice surface roughness could not be measured with the same roughness measuring instrument used to characterise the steel surfaces because the stylus tip, made of diamond and having a radius of 2  $\mu\text{m}$ , produced scratches on the ice surface. Therefore, another technique should be used to characterise ice surfaces after such tests. One option would be to produce a replica of the ice surface using a synthetic rubber compound and then use a laser optical roughness measurement device to determine the surface roughness.



Figure 4.13. Ice surface after testing of sample Mr filled with freshwater ice.

#### Piston slide tests

Examples of the load-displacement profiles obtained for samples Sr, Mr, Hr, NHr and TBr filled with freshwater ice are shown in Figure 4.14. Similar dependences were observed in the tests performed on samples filled with salty ice, although lower load values were observed. The shape of the load curves obtained in the tests on samples Mr and Hr, shown in Figure 4.14(b)-(c), is different from the shape obtained during the tests on samples NHr and TBr, presented in Figure 4.14(d)-(e). The load dropped to almost zero after reaching its local maximum repeatedly in the tests on samples Mr and Hr, and the amplitude of the load oscillations associated with the mean load was large in these cases. The load did not reach zero in the tests on samples NHr and TBr, and the load oscillations had relatively small amplitudes and decreased with time.

The tests, performed over a wide range of displacement rates (between  $1.67 \times 10^{-6} \text{ m s}^{-1}$  and  $0.83 \times 10^{-3} \text{ m s}^{-1}$ ) and temperatures (between  $-5^\circ\text{C}$  and  $-25^\circ\text{C}$ ), revealed that

periodic load oscillations could always be observed for samples Mr, Hr and NHR. Both oscillating and monotonic loads were recorded during the tests on samples TBr and Sr, and there was a tendency for the piston to slide without load oscillations at higher temperatures ( $-5^{\circ}\text{C}$ ) and lower displacement rates ( $< 0.83 \times 10^{-5} \text{ m s}^{-1}$ ) in the tests on sample Sr. Both oscillating and monotonic loads were observed in the tests performed at lower temperatures and higher displacement rates. Both types of load curves were observed in the tests on sample TBr over the entire range of displacement rates and temperatures.

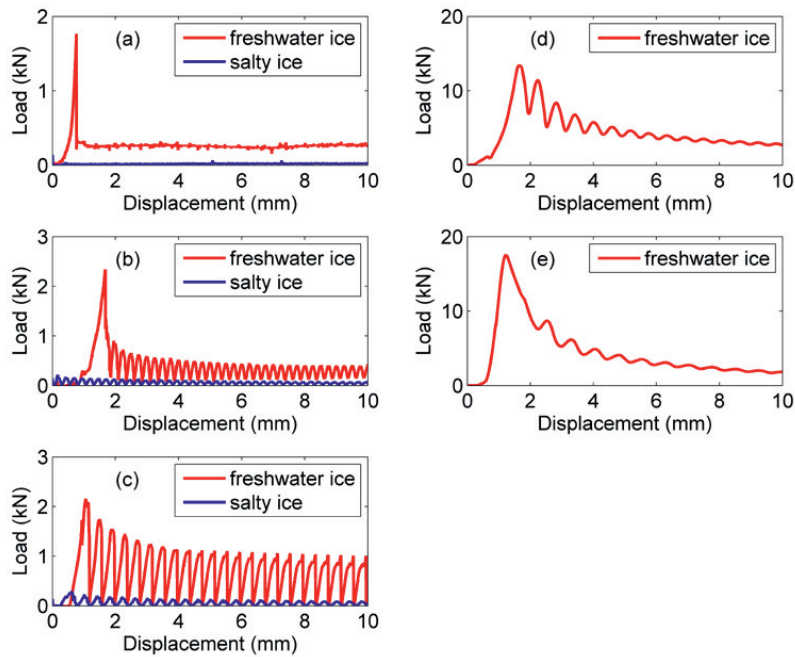


Figure 4.14. Load versus displacement profiles obtained during the “piston slide tests” of the following samples: (a) Sr, (b) Mr, (c) Hr, (d) NHR and (e) TBr. The displacement rate and temperature in the tests performed on freshwater ice were  $0.83 \times 10^{-4} \text{ m s}^{-1}$  and  $-5^{\circ}\text{C}$ , respectively, and the displacement rate and temperature in the tests performed on salty ice were  $0.66 \times 10^{-4} \text{ m s}^{-1}$  and  $-10^{\circ}\text{C}$ , respectively. The salinity of the salty ice was 13.7 ppt.

Figure 4.15 shows the samples after testing. Ice particles were observed on the piston surfaces after the tests on samples NHR and TBr. Furthermore, the ice in the annulus between the piston and the cylinder was significantly damaged and showed multiple cracks. Significantly fewer cracks were observed in the ice in samples Sr, Mr and Hr after testing. Visual inspection of the piston surfaces of these samples did not reveal any ice particles in the surface cavities.

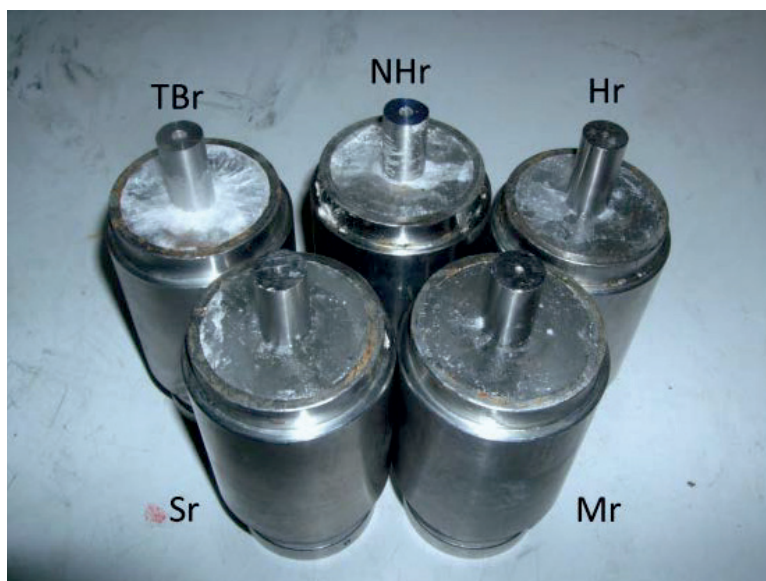


Figure 4.15. Samples after “piston slide tests”.

Fast Fourier transformation was used to calculate the displacement of the piston corresponding to one period of load oscillations. Figure 4.16 shows the dependence of the displacement as a function of the displacement rate for samples Mr, Hr, NHr and TBr. The horizontal lines in Figure 4.16 indicate the profile pitches  $S_m$  for the samples measured with the roughness profilometer (see Figure 4.3).

A similar analysis performed for the tests on sample Sr did not reveal dominant piston displacement corresponding to one load period. Figure 4.17 shows profiles of the load versus piston displacement for sample Sr at the same displacement rate of  $0.83 \times 10^{-4} \text{ m s}^{-1}$ , but at different test temperatures. Steady-state piston sliding was observed in the tests at  $-5^\circ\text{C}$ , and load oscillations were registered at  $-10^\circ\text{C}$ . The displacement of the piston corresponding to one load period varied with time and decreased from the initial value of 0.14 mm to 0.015 mm. In the test performed at  $-25^\circ\text{C}$ , the observed stick-slip motion suddenly transformed into steady-state sliding beyond a displacement of 4.2 mm.



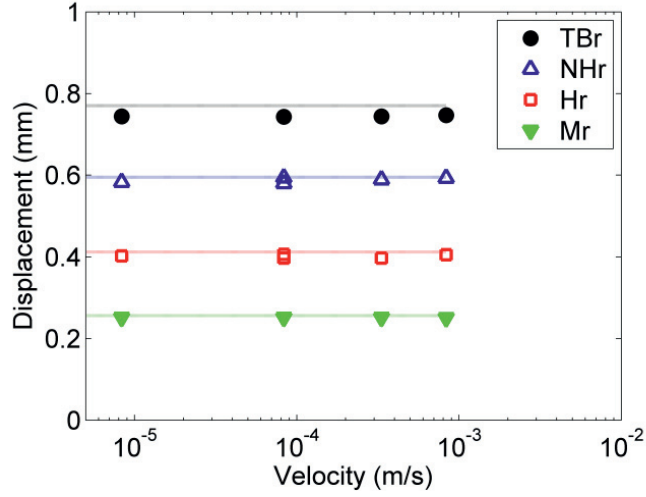


Figure 4.16. Displacement of the piston corresponding to one period of load oscillation versus the displacement rate. The horizontal lines indicate the profile pitches  $S_m$  measured with the profilometer.

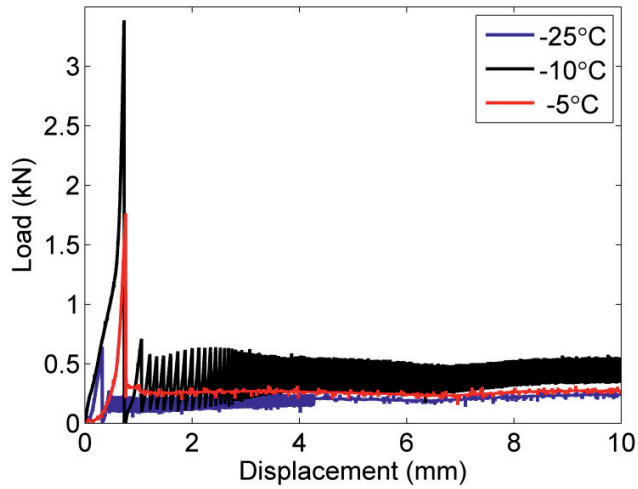


Figure 4.17. Load versus displacement profiles obtained from the piston slide tests. The displacement rate was  $0.83 \times 10^{-4} \text{ m s}^{-1}$ , and the tests were performed at three different temperatures:  $-25^\circ\text{C}$ ,  $-10^\circ\text{C}$  and  $-5^\circ\text{C}$ .

### 4.3.2 “Type II” tests

Only “piston slide” samples (Figure 4.1) filled with freshwater ice were used in the “Type II” tests. The applied (programmed) load ( $F_{app}$ ) varied among the tests performed on the different samples and ranged between 25 and 90% from the mean first peak load ( $F_{1st\ peak}$ ), which was measured at a constant displacement rate of  $0.83 \times 10^{-4} \text{ m s}^{-1}$  for each corresponding sample in the “Type I” tests. Figure 4.18 shows typical temporal variations in the load and displacement observed in the “Type II” tests. Two distinctive phases were observed in each individual test. In the first phase, the actual load did not lead to a relative displacement between the ice and the piston and remained constant (Figure 4.18(a)). The duration of the first phase was named the onset time. Relative motion was observed in the second phase, and the actual load dropped below the programmed value and began to oscillate. At the beginning of the second phase, the displacement changed with time, similar to the behaviour of a step function (Figure 4.18(b)). The “steps” became smoother with time and finally disappeared, and the piston started to slide at a constant rate.

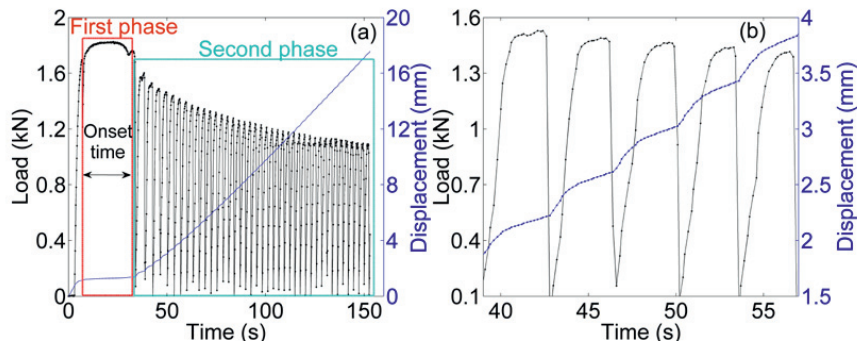


Figure 4.18. Temporal variations in the actual load and displacement during the “Type II” test on sample Hr: (a) entire data record and (b) data for the time period between 39 s and 57 s. The test temperature was  $-15^{\circ}\text{C}$ , and  $F_{app} / F_{1st\ peak} = 75\%$ .

Figure 4.19 shows the temporal variation of the actual load and the displacement in the tests on NHr for different programmed loads. The onset time decreased with an increase in the programmed load. The dependence of the onset time on the programmed load for different samples is presented in Figure 4.20. Similar constant load test results were previously obtained by Nanetti et al. (2008) for Sr, Mr and Hr samples filled with salty ice (the salinity ranged between 3.0 and 8.1 ppt). However, Nanetti et al. (2008) applied significantly lower loads ranging between 0.2 kN and 0.6 kN, to the samples.

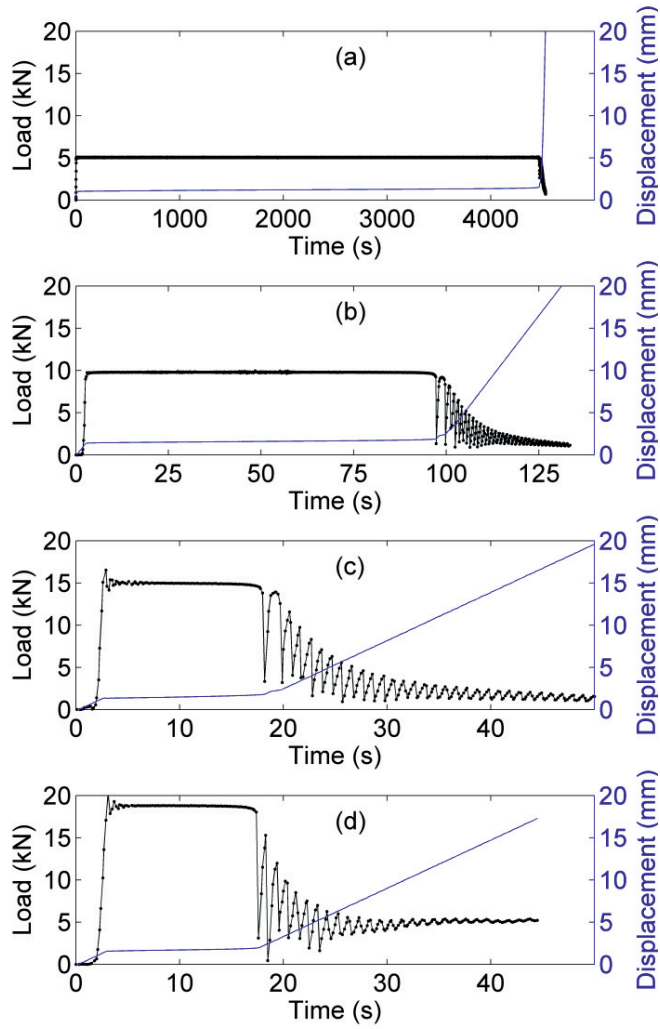


Figure 4.19. Temporal variations in the actual load and displacement observed in the tests on sample NHr at different programmed loads  $F_{app} / F_{1st\ peak}$ : (a) 25%; (b) 50%; (c) 75%; and (d) 90%. The test temperature was  $-15^{\circ}\text{C}$ .

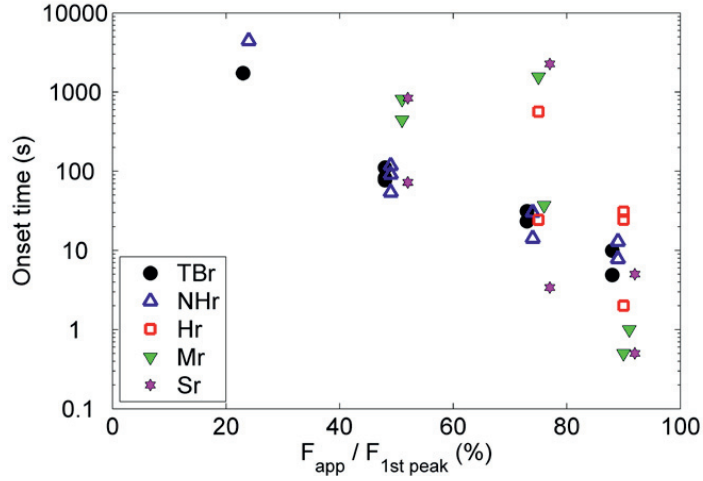


Figure 4.20. Onset time versus programmed (applied) load in tests of different samples. The tests were performed at  $-15^{\circ}\text{C}$ .

During the second phase, the piston moved relative to the ice, and the actual load ceased to be constant and dropped below the programmed value. The piston did not move at a constant speed. Rather, its motion depended on the programmed load. The speed of the piston (displacement rate) was calculated by taking the derivative of the measured displacement with respect to time. Examples of the dependences between the load and displacement rate in the tests on samples Mr and Hr are shown in Figure 4.21.

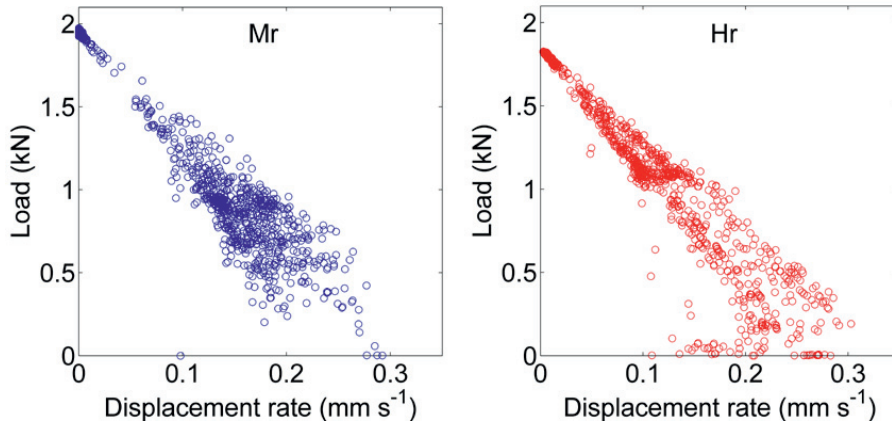


Figure 4.21 Load versus displacement rate in the “Type II” tests on samples Mr and Hr. The test temperature was  $-15^{\circ}\text{C}$ , and  $F_{\text{app}} / F_{1\text{st peak}}$  was 50% and 75% in the tests on samples Mr and Hr, respectively.

Similar load – displacement rate dependences were observed in the tests performed on samples exhibiting different surface roughnesses at lower programmed loads.  $F_{\text{app}}/F_{1\text{st peak}} = 25\%$  in the tests on samples NHr and TBr. At higher applied loads, the piston started to move at a constant displacement rate almost immediately after the sliding was initiated, and such behaviour was explained by the structural features of the compression rig. When the displacement rate was high, the rig could not maintain the programmed load, so the actual load dropped, and the piston accelerated. The influence of the periodical roughness caused a gradual increase in the resistance, deceleration of the piston motion and an increase in the actual load of the rig on the piston. Figure 4.21 shows the existence of a critical displacement rate  $v_0 \approx 0.3 \text{ mm s}^{-1}$ , at which the rig could not provide a load and the actual load dropped to zero.

Knowledge of the normal load would allow us to determine the effect of velocity on the friction coefficient. Ice asperities are deformed during sliding, so the normal load changes, as does the dependence on the displacement and rate. It is likely that the ice asperities are gradually smoothed out, which is the reason why a decrease in peak load was observed during the tests.

#### 4.4 Mathematical model

During testing, the piston (in the “piston slide tests”) and ice (in the “ice slide tests”) were loaded in the downward direction  $x$  by the pushing force ( $F_x$ ) from the rig and the gravity force ( $mg$ ). The resistance force ( $R$ ) due to the interaction between the ice and steel was directed upward and included friction and asperity deformation components (Figure 4.23). The momentum balance in the system can be written as follows:

$$ma = F_x + mg - R, \quad (4.1)$$

where  $a = d^2x/dt^2$  is the piston/ice acceleration and  $m$  is the piston/ice mass. The weight of the piston/ice can be neglected in Eq. (4.1) because  $mg \ll F$ .

The dependence of the resistance on the piston/ice displacement  $x$  can be determined from the tests with a constant displacement rate (“Type I” tests). In this case, the acceleration  $a$  is equal to 0, and the measured force is therefore equal to the resistance. The resistance measured in the “Type I” tests is fit with the function

$$R_f(x) = \frac{p_1}{x+s} \left[ \sin \left( \frac{2\pi}{S_m} x + q_1 \right) + q_2 \right] + R_0, \quad (4.2)$$

where  $p_1$ ,  $s$ ,  $q_1$ ,  $q_2$  and  $R_0$  are the fit coefficients,  $S_m$  is the profile pitch and  $x$  is the piston/ice displacement. The term  $p_1/(x+s)$  describes the reduction of the resistance due to ice abrasion at the contact boundary with the steel surface, while the coefficient  $R_0$  is equal to the resistance when the ice asperities are deleted due to ice abrasion. The

coefficients  $q_1$  and  $q_2$  are used to adjust the phase and reference level of the experimental data, respectively, to the fit.

It is assumed that the applied load in the “Type II” experiments is a linear function of the piston/ice speed  $v = dx/dt$  (Figure 4.21):

$$F_{x,II} = F_0(1 - v/v_0), \quad (4.3)$$

where  $F_0$  is the initial value of the programmed (applied) load and  $v_0$  is the speed when the force drops to zero due to the rig’s inertial properties.

The ice creep effects in the “Type II” experiments are very different from those in the “Type I” experiments because of the varying displacement rate. We approximate the resistance in the “Type II” experiments using the formula

$$R_{II}(x) = kR_I(x), \quad (4.4)$$

where the coefficient  $k$  accounts for the influence of ice creep effects. Because the mean actual load in the “Type I” tests was higher than that in the “Type II” tests, we expect that the coefficient  $k < 1$  (see Table 4.4 and Table 4.5).

From Eqs. (4.1)-(4.3), we obtain

$$ma = F_{x,II} - R_{II}. \quad (4.5)$$

Solving the ordinary differential equation (4.5), we obtain the temporal variation of the piston/ice displacement as a function of time in the “Type II” tests.

The data from the “piston slide tests” on samples Mr and Hr were used to validate the model. The resistance  $R_I(x)$  was calculated from the “Type I” tests performed at a constant displacement rate of  $0.167 \text{ mm s}^{-1}$ . The fit parameters and mean forces  $\langle F \rangle_I$  during the tests are presented in Table 4.4.

Table 4.4. Fit coefficients in the resistance formula (4.2) obtained from the “Type I” tests performed at a displacement rate of  $0.167 \text{ mm s}^{-1}$ . The tests were carried out at  $-18^\circ\text{C}$ .  $\langle F \rangle_I$  is the mean force during the entire test.

Sample	$p_1$	$s$	$q_1$	$q_2$	$R_0$	$\langle F \rangle_I$ (kN)
Mr	-5.76	6.7	5.38	0.66	1.84	1.62
Hr	-20.6	14.0	-0.44	-0.29	1.21	1.41

From the “Type II” tests, we determined  $F_{x,II}$  as a linear function of the piston/ice displacement rate. The fit parameters  $F_0$  and  $v_0$  were obtained from the tests on samples Mr and Hr and are presented in Table 4.5. Next, we calculated the displacement, solving equation (4.5) with an adjusted coefficient  $k$ , and compared the simulation results with the displacements measured in the tests.

Figure 4.22 shows the displacements measured in the “Type II” tests and calculated using equation (4.5). The model was able to predict only the second phase of the tests, and the origin of the time axes corresponded to the beginning of the second phase. The coefficient  $k$  was chosen as 0.75 and 0.525 for the numerical tests of samples Mr and Hr, respectively.

Table 4.5. Fit coefficients in the force – displacement rate dependence obtained in the “Type II” tests. The tests were performed at  $-15^\circ\text{C}$ .  $\langle v \rangle$  and  $\langle F \rangle_{II}$  are the mean displacement rate and force during the second phase of the “Type II” tests, respectively.

Sample	$F_0$ (kN)	$v_0$ (mm s $^{-1}$ )	$\langle v \rangle$ (mm s $^{-1}$ )	$\langle F \rangle_{II}$ (kN)
Mr	1.95	0.289	0.158	0.87
Hr	1.8	0.278	0.138	0.90

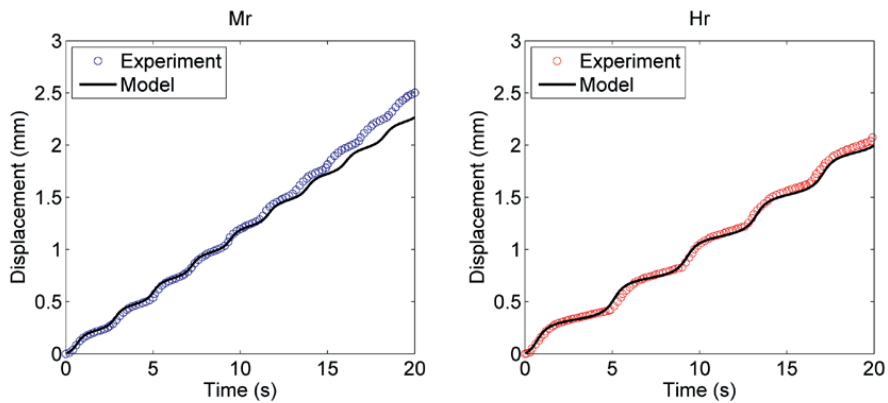


Figure 4.22. Displacements measured in the “Type II” tests and simulated displacements versus time for samples Mr and Hr.

## 4.5 Discussion

The initial objective of the tests was to measure the friction coefficient between ice and steel for different surface roughnesses. The normal load at the ice-steel interface must be known to calculate the friction coefficient. Two measuring techniques were employed to measure this normal load: 1) the use of tactile sensors glued onto the inner surface of the hollow cylinder and 2) the use of an FBG sensor frozen in the ice near the interface. Neither technique allowed us to measure the normal pressure at the interface. Therefore, further work on effective methods for measuring the pressure should be pursued.

### Estimates of the pressure concentration between ice and steel

The ice asperities observed on the ice surface after the ice slide tests performed on samples Mr and Hr (Figure 4.14), and the absence of ice particles on the piston surfaces after the piston slide tests performed samples Sr, Mr and Hr (Figure 4.16), indicated that the ice asperities, which were in contact with the piston/cylinder, were not fully worn by the harder steel asperities. Therefore, elastic deformations of the ice asperities could have had an influence on the formation of the load oscillations observed during the tests. The peak loads during stick-slip occurred when the steel surface roughness peaks were in contact with the ice roughness peaks. The decrease in the load amplitude and its mean value (Figure 4.12 and Figure 4.14) were likely related to the gradual decrease in ice surface roughness. The formation of a melted water film at the ice-steel interface (Bowden and Hughes, 1939) and/or shear in the softened ice asperities due to friction heating (Akkok et al., 1987) may have been responsible for the decrease in ice surface roughness.

The upper limit of the contact pressure between ice and steel can be estimated using the Hertz contact problem. A schematic of the interaction between ice and steel asperities during an “ice slide test” is shown in Figure 4.23. Let us consider the cross-section of a sample to be the plane  $(x, y)$ , where the  $x$  axis coincides with the axis of the cylinder and the  $y$  axis is perpendicular to the  $x$  axis (Figure 4.23). In the plane  $(x, y)$ , the ice and steel roughness profiles are periodic, with equal periods  $S_m$ , and the heights of the ice and steel asperities are  $2a$  and  $2A$ , respectively. In this study, we assumed that the height of the ice asperities decreased from an initial value of  $2A$  to  $2a$  due to their abrasion on the steel surface. The local minima of the measured load  $F_x$  occur when the ice surface cavities are in contact with the steel roughness peaks (solid lines in Figure 4.23). When the ice is displaced relative to the cylinder in the  $x$  direction, the ice asperities deform. The maximum deformation occurs when the ice and steel roughness peaks are in contact. In this case, the normal displacement of the ice surface (in the  $y$  direction) relative to the unstrained ice surface (dashed line in Figure 4.23) is equal to  $\delta_n = 2a$ . The mean pressure arising from the contact between the ice and steel asperities can be estimated as follows. Because the cylinder’s inner radius is much larger than the mean pitch profile  $S_m$ , the asperities of the ice and cylinder surfaces can be approximated locally as annular cylindrical surfaces, and the interaction between them can be approximated as the interaction between ice and steel cylinders with radii  $R_1$  and



$R_2$  (Figure 4.23). The running force between two parallel, infinitely long elastic cylinders with radii  $R_1$  and  $R_2$  compressed along their generators is determined as follows (Landau and Lifshitz, 1987):

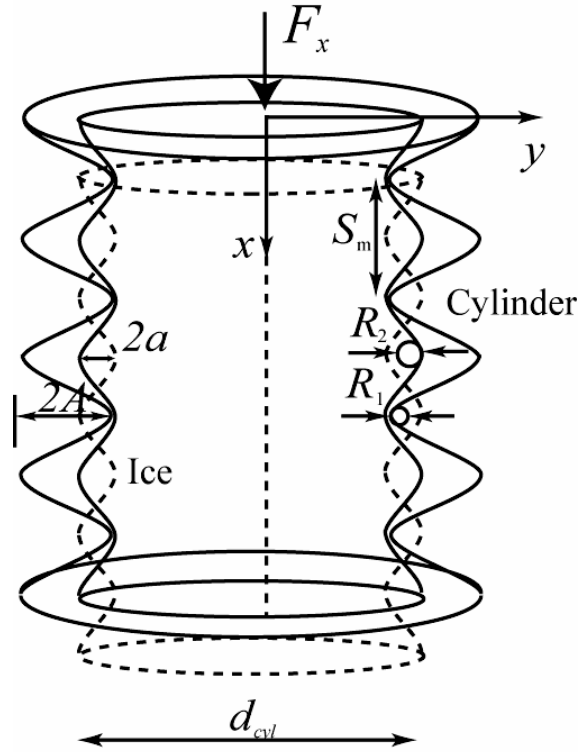


Figure 4.23. Scheme of the interaction between ice and steel asperities in an “ice slide test”.

$$f_n = \frac{3\pi}{8D} \delta_n, \quad (4.6)$$

where  $\delta_n$  is the relative displacement of the cylinders,  $D = \frac{3}{4} \left[ \frac{(1-\nu_1^2)}{E_1} + \frac{(1-\nu_2^2)}{E_2} \right]$  and  $\nu_1$ ,  $E_1$  and  $\nu_2$ ,  $E_2$  are the Poisson's ratio and Young's modulus of steel and ice, respectively. The mean pressure between two compressed cylinders is

$$p_{\max} = \frac{f_n}{2w}, \quad (4.7)$$

where  $w$  is the half-width of the contact. The relative cylinder displacement and contact width are related by the equation  $\delta_n = w^2 B$ , where  $B = 1/2 \cdot (R_1^{-1} + R_2^{-1})$  and  $R_1$  and  $R_2$  are the cylinder radii. The running force  $f_n$  can be calculated using the pushing force  $F_x$  measured during testing as follows:

$$f_n = \frac{F_x}{\mu L / S_m \pi d} \quad (4.8)$$

where  $\mu$  is the friction coefficient between ice and steel,  $L$  is the height of the hollow cylinder,  $S_m$  is the mean profile pitch (periodicity of roughness) and  $d$  is the inner diameter of the cylinder or piston. The displacement  $\delta_n$ , and therefore the amplitude of the ice surface roughness  $a$ , can be calculated using Eq. (4.6) in conjunction with Eq. (4.8). The ice and steel roughness profiles in the  $x$  direction can be approximated by sine functions with a wavenumber  $k = 2\pi / S_m$  and the amplitudes  $a$  and  $A$  (corresponding to the half-height of the steel surface asperities), respectively. Therefore,  $R_1$  and  $R_2$  are defined by the expressions  $R_1^{-1} = Ak^2$  and  $R_2^{-1} = ak^2$ . To estimate the contact pressure, we use the friction coefficient between ice and steel  $\mu = 0.2$  and the Young's moduli and Poisson's ratios of steel ( $E_1 = 200$  GPa and  $\nu_1 = 0.3$ , respectively) and ice ( $E_2 = 9$  GPa and  $\nu_2 = 0.3$ , respectively). The contact pressure  $p_{\max}$  and corresponding contact areas  $S_{\text{cont}} = \pi d \cdot 2w$  in the "ice slide" and "piston slide" tests performed on samples Sr, Mr and Hr are presented in Table 4.6. The contact pressures in the "ice slide tests" were higher than those in the "piston slide tests". This result could be attributed to the difference in the steel surface roughness depths  $R_z$ , which were higher for the cylinder surfaces.

Table 4.6. Upper limits of the contact pressure ( $p_{\max}$ ) between the ice and steel asperities and corresponding contact areas ( $S_{\text{cont}}$ ) in the "ice slide" and "piston slide" tests performed on samples Sr, Mr and Hr.

Sample	"Piston slide tests"		"Ice slide tests"	
	$p_{\max}$ (MPa)	$S_{\text{cont}}$ (m <sup>2</sup> )	$p_{\max}$ (MPa)	$S_{\text{cont}}$ (m <sup>2</sup> )
Sr	34	$3.4 \times 10^{-8}$	33	$1.2 \times 10^{-7}$
Mr	57	$2.6 \times 10^{-7}$	97	$0.9 \times 10^{-6}$
Hr	99	$7 \times 10^{-7}$	239	$2.6 \times 10^{-6}$

The values obtained for the local pressure were somewhat higher than those reported in the literature during ice indentation (Gagnon, 2008; Johnston et al., 1998; Jordaan, 2001; Kim et al., 2012; Sodhi, 2001; Timco and Frederking, 1995). The main reason for the discrepancy was related to our simplifying assumptions about the pure elastic behaviour of the ice and small ice asperity deformations during their interaction with steel asperities. Nevertheless, the ice's dominant elastic behaviour during impact was reported previously by Maeno (1988). If a piece of ice is dropped on the floor, it will be broken in many pieces (Maeno, 1988). However, under very strong impact, an ice ball

may bounce off the floor like a tennis ball. Kuniaki and Maeno performed tests where small ice balls with a diameter of 1.5 mm were dropped on a flat ice surface at a temperature of  $-15^{\circ}\text{C}$  (Maeno, 1988). The authors found that the coefficient of reflection, which is the ratio between the ice ball velocity after and before the impact, was equal to 0.8. When the ice balls had an ideal spherical shape and for impact velocities less than  $1 \text{ m s}^{-1}$ , the reflectivity coefficient rose to 0.9. According to Maeno (1988), the reflection coefficient for elastic materials such as ivory and marble at similar velocities of impact is 0.8. The reflection coefficients for brass and steel are the same and equal to 0.5, and for lead, the reflection coefficient is equal to 0.3. Very high values of the reflection coefficient in the tests with ice balls indicate that ice exhibits significant elastic behaviour.

The maximum contact pressure that appears in the contact during the impact of an ice ball with a flat ice surface is estimated using the explicit solution of the contact problem between an elastic sphere of radius  $R$  and an elastic half space.

In the lowest position of the ice ball, the elastic energy of the system ( $U$ ) is equal to the kinetic energy of the ball before the collision ( $K$ ). According to Landau and Lifshitz (1987), the elastic energy of the elastic system is defined as follows:

$$U = \frac{4}{15} \frac{E}{(1-\nu^2)} \frac{a^5}{R^2}, \quad (4.9)$$

where  $E$  and  $\nu$  are the elastic modulus and Poisson's ratio of ice;  $a$  is the radius of the contact zone; and  $R$  is the radius of the ice ball. The kinetic energy of the ball before the impact is

$$K = \frac{mv^2}{2}, \quad (4.10)$$

where  $m = 4/3 \cdot \pi R^3 \rho_i$  is the mass of the ice ball;  $R$  is the radius of the ball;  $\rho_i$  is the density of the ice; and  $v$  is the velocity of the ball before the impact. According to energy conservation,  $U$  is equal to  $K$ , and therefore the right side of Eq. (A-1) is equal to the right side of Eq. (A-2). Therefore, we can find the expression for the radius of the contact zone ( $a$ ). The mean pressure  $p$  over the contact zone is estimated with the formula

$$p = \frac{F}{\pi a^2}, \quad (4.11)$$

where  $F$  is the maximum contact force and is defined as follows (Landau and Lifshitz, 1987):

$$F = \frac{2E}{3(1-\nu^2)} \frac{a^3}{R}. \quad (4.12)$$

For the calculations, we will use the values presented by Maeno (1988). The ice ball diameter  $2R=1.5 \text{ mm}$ ;  $E=9 \text{ GPa}$ ;  $\nu=0.3$ ; and the ice density  $\rho_{ice} = 916 \text{ kg/m}^3$ . The calculations give a value for the mean contact pressure of  $p=124 \text{ MPa}$ , and the radius of the contact area  $a= 4.4 \cdot 10^{-5} \text{ m}$ . The pressure distribution in the contact zone is not uniform and depends on the distance from the centre of the contact ( $r$ ) as follows:

$$p(r) = p_0 \left( 1 - \frac{r^2}{a^2} \right)^{1/2}, \quad (4.13)$$

where  $p_0 = \frac{3F}{2\pi a^2}$  is the maximum contact pressure. Therefore, the estimate of the maximum pressure in the contact is  $p_0 = 186$  MPa. This value is close to the contact pressure between the ice and steel asperities obtained in our tests.

### Shear strength of ice

The ice asperities in samples NHr and TBr were sheared, and the cavities of the piston/cylinder surfaces were filled with ice particles (Figure 4.15). The shear strength of the ice was estimated by dividing the first peak load by the apparent ice-piston contact area. The estimate yielded an ice shear strength ranging between 3 and 11 MPa, and the obtained shear strength was somewhat higher than the value of 1100 kPa reported in the literature (Timco and Weeks, 2010). The higher values obtained from our tests could be explained by the formation of cracks inside the ice.

### Effect of roughness on ice-steel interaction

The frictional resistance between ice and steel observed in our tests was significantly dependent on the mean height of the steel irregularities, a result that was in agreement with the conclusions made by Saeki et al. (1986), who observed no correlation between the coefficients of friction and the test specimens' mean profile pitches. According to our test results, the profile pitch  $S_m$  governed the slip distance during stick-slip. It should be noted that Saeki et al. (1986) used steel surfaces with randomly oriented asperities, whereas the surfaces of our samples were carefully structured.

## **4.6 Summary**

This study performed new small-scale laboratory tests on ice-steel sliding. Both freshwater ice and salty ice were used in the tests, and the effects of sliding rate, temperature, applied load and surface roughness on the ice-steel interaction were investigated. The main findings are summarised as follows.

- Stick-slip was always observed in samples Mr, Hr and NHr, which had intermediate roughnesses (their arithmetic roughness  $R_a$  ranged between 2  $\mu\text{m}$  and 15  $\mu\text{m}$ ). Both steady-state sliding and stick-slip were observed in the tests performed on samples Sr and TBr, which showed the lowest ( $R_a = 0.31$   $\mu\text{m}$ ) and highest ( $R_a = 25.2$   $\mu\text{m}$ ) roughnesses, respectively.
- The relative piston-ice/ice-cylinder displacement, corresponding to one period of the load oscillations in the tests performed at a constant displacement rate, was found to be equal to the mean pitch profile  $S_m$  in all samples except Sr. The displacements remained the same in the tests performed at different displacement rates ranging between  $0.83 \times 10^{-5}$   $\text{m s}^{-1}$  and  $0.83 \times 10^{-3}$   $\text{m s}^{-1}$ .

- The ice surfaces of samples Mr and Hr after testing were covered by asperities that were similar in shape to those of the inner cylinder surfaces. These results revealed the existence of elastic deformations in the ice asperities when they moved relatively to the steel surface asperities.
- The loads measured in the experiments using fresh water ice samples were significantly higher than those measured in the experiments using saline ice samples ( $16.1 \pm 1.5$  ppt).
- The upper limit of ice pressure concentration on the steel surface estimated from the tests was approximately 239 MPa.



# Chapter 5

## 5 Vertical action on a pile frozen in level ice due to water level changes

### 5.1 Introduction

In cold regions, an ice sheet floating on the water surface may adfreeze to structures (Figure 5.1(a)). If the water level changes, a vertical ice force will be exerted on a pile by the bent level ice (Figure 5.1(b)). An upward force acting on the structure due to a rise in the water level under certain conditions may partially lift the structure off the base and/or damage it structurally (Kerr, 1985).

The problem of vertical ice action on structures due to water level changes has been considered in a number of papers (Christensen, 1986; Kerr, 1975; Matskevitch and Shkhinek, 1992; Terashima et al., 2006; Tryde, 1983; Zabilansky, 1985). However, a limited number of studies were performed in field conditions with sea ice (Christensen, 1986; Terashima et al., 2006).

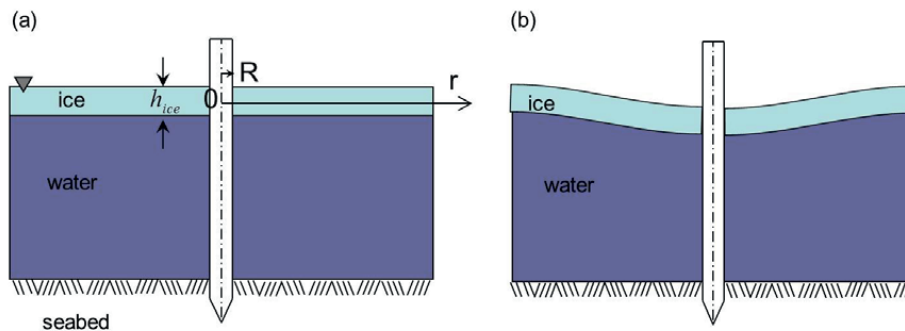


Figure 5.1. Vertical pile frozen in the level ice: (a) ice sheet does not exert vertical force on the pile; (b) ice bent due to changing water level uplifting the pile.

This chapter presents the results from field tests where isolated vertical piles frozen in level sea ice were pushed in a vertical direction. The first peak force, associated with the adhesion, was measured. Elastic plate theory (Timoshenko and Woinowsky-Krieger, 1959) was used to calculate the vertical force necessary to initiate ice-steel relative sliding.

## 5.2 Field experiments on the vertical forces exerted on metal piles frozen in level sea ice due to water level change

The goal of the tests was to measure the ice friction on a vertical pile frozen in sea ice. This experiment is a large-scale version of the tests performed in laboratory on stick-slip interaction between ice and stainless steel, as described in Chapter 4.

### 5.2.1 Experimental setup and procedure

Figure 5.2 shows the experimental setup. An isolated pile frozen in the level sea ice was pushed through the ice in a vertical direction by a hydraulic jack. The jack was placed between the top edge of the pile and a steel frame attached to the ice by two anchors. The pressure in the hydraulic jack was controlled by a monometer. Therefore, the load applied to the pile could be easily determined. Two sets of tests were performed with two different hydraulic jacks. The first set was performed with the hydraulic jack shown in Figure 5.2. The second set of tests was performed with the help of a borehole jack (BHJ) used as a jack, shown in Figure 5.3. By using the BHJ, we were able to measure and record the temporal evolution of the applied load (pressure in the BHJ) and the displacement.

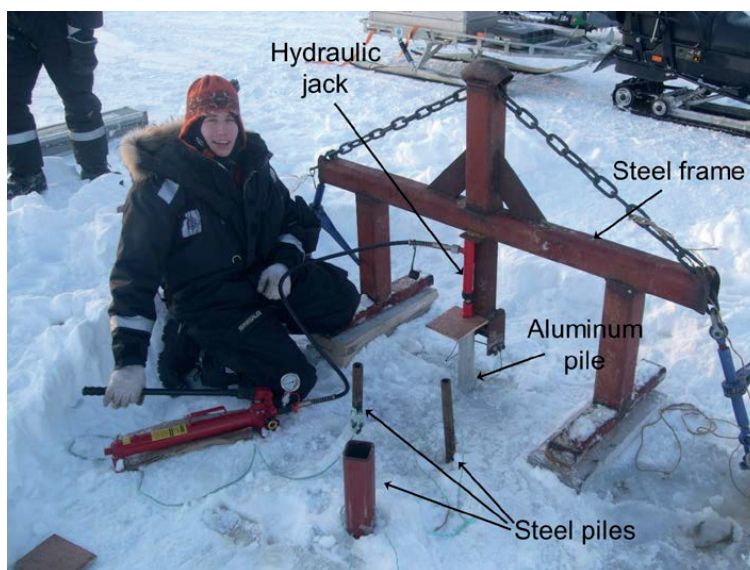


Figure 5.2. Experimental setup to push a vertical pile frozen in level ice.

Four piles with different dimensions and made of different materials were used in the tests (Figure 5.4). Three piles were made of steel and one of aluminium. One of the steel piles was painted, while the other two were slightly corroded.



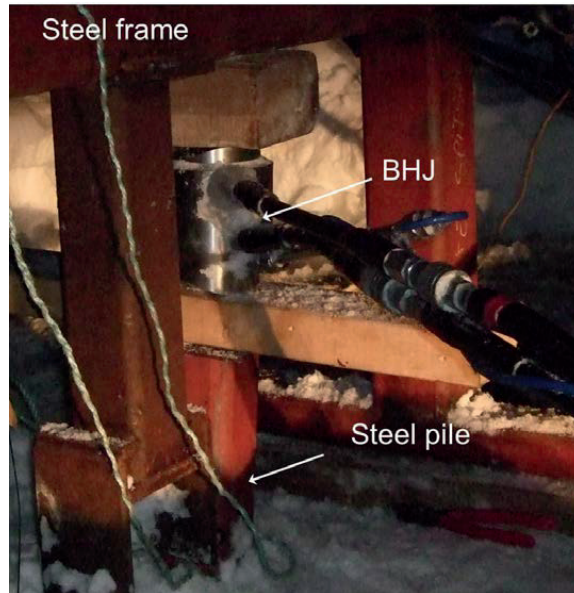



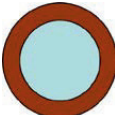
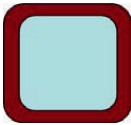
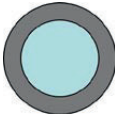
Figure 5.3. Pile pushed using a BHJ as a jack.



Figure 5.4. Ice piles used in the tests (left photo) and measurements of their roughness.

The fourth pile was made of aluminium. The surface roughness measurements were performed using a profilometer Surfest SJ301 (Figure 5.4). Table 5.1 gives details of the dimensions and roughnesses ( $R_a$ ) of the piles used in the tests.

Table 5.1. Shape, dimensions and surface roughness of the piles used in the tests.

Pile No.	Material	Coating	Shape	Ext. diameter (mm)	Int. diameter (mm)	$R_a$ ( $\mu\text{m}$ )
1	Steel	No. (slightly rusted)		35	25	11.1
2	Steel	No. (slightly rusted)		33	27	9.1
3	Steel	Painted		80	65	9.55
4	Aluminium	No		60	53	0.16

### Test procedure

We drilled four holes in the ice with diameters slightly larger than the diameter of the largest pile (no. 3). The holes were drilled in 50 cm thick level sea ice in Van Mijenfjord at Spitsbergen. All piles were longer than the thickness of the ice. Each pile was inserted in a hole in the ice so that the lower end of the pile was lower than the bottom of the level ice and did not touch seabed. The piles were secured with ropes to prevent their sinking before they could be frozen into the ice. Two different sets of tests were performed. In the first set, ice formed between the piles and the surrounding level ice over 44 hours at low air temperature ( $T_{air} < -10^\circ\text{C}$ ). As mentioned above, the hydraulic jack shown in Figure 5.2 was used in this set of tests. In the second set of tests, the piles were left to refreeze in the surrounding level ice for one week. No significant increase in the level ice thickness was observed. Nevertheless, it is likely that thicker ice was formed in the vicinity of the ice-pile interface. In this set of tests, the piles were pushed downwards using BHI as a jack.

## 5.2.2 Results and analysis

### *First set*

The first measured peak load (pressure in jack) corresponds to the initiation of the ice-pile relative sliding and is governed by the adhesion strength in shear. Table 5.2 presents the results from this set of tests. The pile made of aluminium went through the ice at a significantly lower applied force than the steel piles. This result could be explained by the differences in adhesion and surface roughness. In the test with pile 1, with corroded steel surfaces, the first peak load was higher than in the test with pile 4, which had a painted surface. Due to misalignment, steel pile no. 2 was bent during the test, and its ice-pile relative sliding was not observed.

Table 5.2. Peaks forces measured in the first set of experiments. In the table “Pressure” is the pressure in the jack.

Pile No.	Material	Pressure (bar)	Force (kN)	Adhesion strength (kPa)
1	Steel	450	17	309
2	Steel	200*	7.6	-
3	Steel	300	11.4	76
4	Aluminium	< 50	< 1.9	< 20

\* Due to misalignment, the pile was bent instead of sliding through the ice.

### *Second set*

In the second set of tests, piles no. 1, 3 and 4 were used (Table 5.1). The piles were left to refreeze in the surrounding level ice during a time period of one week. In this set of tests, BHJ was used. The pressure of the BHJ was increased to push the vertical pile downwards through the ice. At first, the adhesion at the ice-pile interface resisted the vertical force. At a particular moment, the pressure of the BHJ was high enough to push the pile a small distance downwards. The slip-phase stopped when the ice resistance around the perimeter of the pile was rebuilt again, and then the pile was stuck again. During the complete test, this cycle of stick-slip behaviour repeated itself several times. Figure 5.5 shows the temporal variations of the forces and displacements in the tests with piles no. 1, 3 and 4, respectively.

In the tests with piles no. 1 and 4 (steel and aluminium piles with circular cross-sections), the vertical force applied to the piles reached a certain value necessary to initiate ice-pile relative sliding, then remained almost constant. The values of the applied forces in both tests were almost the same. Nevertheless, due to the difference in the contact area between the steel and aluminium piles, the shear stress was lower in the tests with the aluminium pile. The shear corresponding to the initiation of the ice-pile relative sliding was 348 kPa and 168 kPa for the steel and aluminium piles, respectively. In the tests with the pile with a square cross-section, the shear was 140 kPa. In the test with pile no. 3 (steel pile with square cross-section), the pressure in the BHJ (and, therefore, applied to the pile as a downward force) increased more or less

linearly as the pile was pushed downwards at a constant rate. A possible reason for the increase in the force is the presence of the adfrozen ice on the part of the pile surface that was initially slightly above the level of the ice surface.

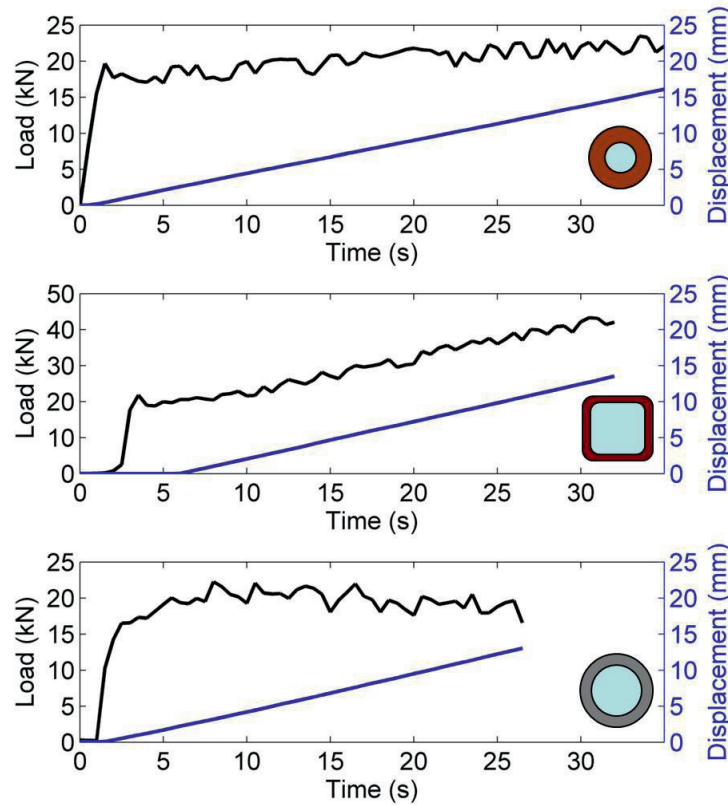


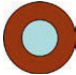


Figure 5.5. Temporal variations of vertical force and pile displacement in the second set of tests for piles no. 1, 3 and 4. Piles were pushed downwards using a BHJ.

In all three tests, the vertical displacement showed a linear trend. However, the visual observations clearly showed stick-slip behaviour during ice-pile relative sliding. Slight oscillations of the vertical force can be observed in Figure 5.5. Due to a low sampling frequency of 2 Hz, it was difficult to capture the details of the stick-slip behaviour. However, the origin of the stick-slip is closely related to the internal mechanism of the BHJ. The piston of the BHJ is extracted due to an increase in the oil pressure. As the force necessary to initiate the movement of the pile is reached, the pile slides downwards for a certain distance, accompanied by a drop in pressure. The pile stops, then slides again as soon as the necessary force (pressure in the BHJ) builds up again, and then the process repeats.

### 5.2.3 Discussion

The comparison of the results obtained in the two test sets is presented in Table 5.3. The shear was higher in the second set of tests for all samples. However, the increase in the tests with pile no. 1 was not as significant as in the tests with piles no. 3 and 4. The difference in the adhesion strength in shear in the two sets of tests is most likely related to the difference in the ice salinity adhered to a pile. In the 1<sup>st</sup> set of tests, the sea water between the pile and the surrounding level ice froze for a period of 44 hours, while in the 2<sup>nd</sup> set of tests, the freezing time was 173 hours. The air temperature during the whole period was stable and did not exceed -10°C. The brine drainage (which is a very slow process) in the ice adjacent to the pile made the ice fresher in the second set of tests, and therefore it had a higher adhesion strength in shear (Makkonen, 2012).

Table 5.3. Comparison of the results obtained in the two different sets of tests. The first set was performed after the piles had been exposed to freezing in the level ice during 44 hours. In the second set of tests, the freezing time was around one week (173 hours). The air temperature during this period was consistently below -10°C.

Pile No.	Shape	Adhesion strength (kPa) 1 <sup>st</sup> set	Adhesion strength (kPa) 2 <sup>nd</sup> set
1		309	348
3		76	140
4		< 20	53

The values for the adhesion strength in shear obtained in our tests were lower than the values reported by Haehnel and Mulherin (1998). The discrepancy could be explained by the fact that Haehnel and Mulherin (1998) used distilled water in their lab tests. Another possible reason is the difference in surface roughnesses.

### 5.3 Calculation of the vertical forces

#### *Governing equation of the elastic plate*

Let us consider an isolated pile surrounded by an infinite elastic thin ice sheet (Figure 5.1). Elastic plate theory (Timoshenko and Woinowsky-Krieger, 1959) is used to calculate the uplifting force. The problem illustrated in Figure 5.1 can be reformulated: an absolutely rigid cylindrical insert with radius  $R$  is frozen in the infinitely large floating ice sheet, as shown in Figure 5.6. When a force  $F$  is applied to the insert, the ice sheet may bend. The deflection of the ice sheet from its initial position  $w(r)$  is a function of the distance from the centre of the pile. The maximum deflection at the ice-

insert interface corresponds to the water level change in the initial formulation of our problem.

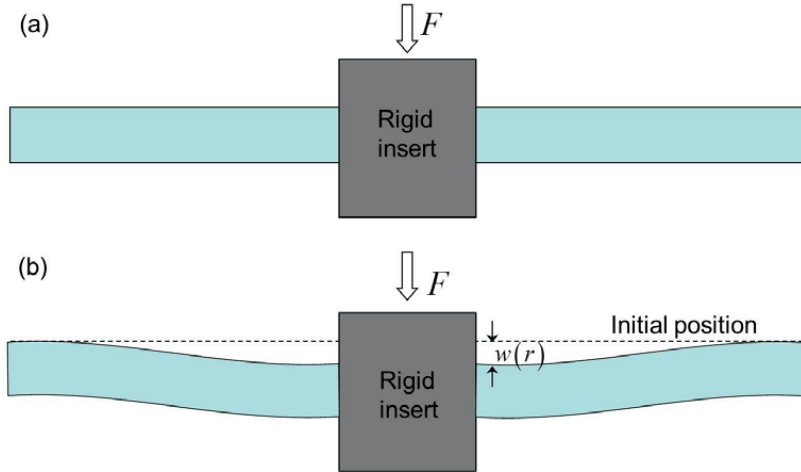


Figure 5.6. Equivalent problem to the ice-pile interaction when the water level is changing.

In polar coordinates, the linear equation for the small deflection of a thin, elastic plate floating on the water surface is (Squire et al., 1996):

$$D \frac{1}{r} \frac{d}{dr} \left\{ r \frac{d}{dr} \left[ \frac{1}{r} \frac{d}{dr} \left( r \frac{dw}{dr} \right) \right] \right\} + \rho g w = 0, \quad (5.1)$$

where  $D$  is the flexural stiffness of the ice plate,  $w$  is the deflection in the vertical direction;  $\rho$  is the water density;  $g$  is the acceleration due to gravity; and  $r$  is the distance from the centre of the plate. Eq. (5.1) can be written in the form:

$$D \left( \frac{d^2}{dr^2} + \frac{1}{r} \frac{d}{dr} \right) \left( \frac{d^2 w}{dr^2} + \frac{1}{r} \frac{dw}{dr} \right) + \rho g w = 0. \quad (5.2)$$

Plate stiffness is related to the Young's modulus  $E$ , Poisson's ration  $\nu$  and the plate thickness  $h$  with the formula:

$$D = \frac{Eh^3}{12(1-\nu^2)}. \quad (5.3)$$

The general solution of Eq. (5.2) can be written in terms of Kelvin functions (Timoshenko and Woinowsky-Krieger, 1959):

$$w(r) = C_1 \operatorname{kei}\left(\frac{r}{l}\right) + C_2 \operatorname{ker}\left(\frac{r}{l}\right) + C_3 \operatorname{ber}\left(\frac{r}{l}\right) + C_4 \operatorname{bei}\left(\frac{r}{l}\right), \quad (5.4)$$

where  $l = (D / \rho g)^{1/4}$  is a characteristic length, and  $C_1, C_2, C_3$  and  $C_4$  are constants that should be determined from the boundary conditions. Kelvin functions are related to the Bessel functions of the first  $I_0$  and second  $K_0$  order from the complex argument by the expressions:

$$I_0(x\sqrt{\pm i}) = \operatorname{ber} x \pm i \operatorname{bei} x; \quad K_0(x\sqrt{\pm i}) = \operatorname{ker} x \pm i \operatorname{kei} x, \quad (5.5)$$

where  $x$  is variable.

The deflection (5.4) should have a finite value when  $r \rightarrow \infty$ . Therefore, we can conclude that  $C_3 = C_4 = 0$ , as the functions  $\operatorname{ber}\left(\frac{r}{l}\right)$  and  $\operatorname{bei}\left(\frac{r}{l}\right)$  are going to infinity when  $r$  increases. Thus, solution (5.4) becomes:

$$w(r) = C_1 \operatorname{kei}\left(\frac{r}{l}\right) + C_2 \operatorname{ker}\left(\frac{r}{l}\right). \quad (5.6)$$

#### Boundary conditions

At the initial moment of time, the ice is frozen to the insert. Therefore, the normal section adjacent to the insert has zero rotation:

$$\left. \frac{dw}{dr} \right|_{r=R} = 0. \quad (5.7)$$

The cutting force on the interface reads

$$Q|_{r=R} = D \frac{d}{dr} \left[ \frac{1}{r} \frac{d}{dr} \left( r \frac{dw}{dr} \right) \right] \Big|_{r=R} = \frac{F}{2\pi R}, \quad (5.8)$$

where  $F$  is the total force acting on the insert.

#### Solutions

Substituting boundary conditions Eq. (5.7) and (5.8) into the solution Eq. (5.6), we will obtain the deflection of the ice sheet as a function of the radial coordinate  $r$  and applied to the insert force  $F$  (which corresponds to the uplifting force).

The bending moments per unit length in the ice sheet can be defined as follows:

$$\begin{aligned} M_r &= -D \left( \frac{d^2 w}{dr^2} + \frac{\nu}{r} \frac{dw}{dr} \right) \\ M_\theta &= -D \left( \frac{1}{r} \frac{dw}{dr} + \nu \frac{d^2 w}{dr^2} \right) \end{aligned} \quad (5.9)$$

where  $\nu$  is the Poisson ratio of ice.

Figure 5.7 shows the distribution of the bending moments per unit length. The values for the parameters used for the calculation are presented in Table 5.4. The flexural

strength of the level sea ice and Young's modulus were obtained by Karulina et al. (2013) for the same location where our field experiments on pushing the piles through the ice (presented in the previous section) were performed.

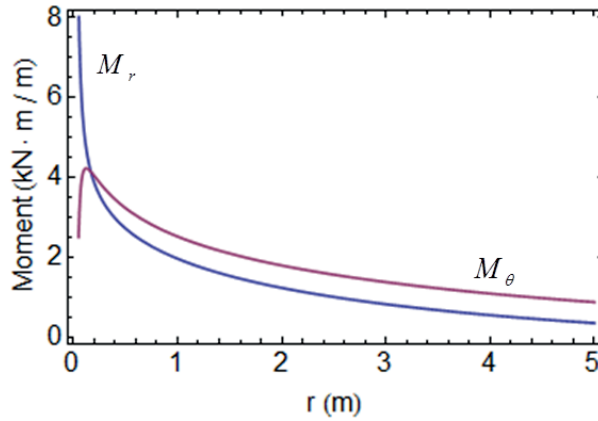


Figure 5.7. Bending moments per unit length along the radial coordinate,  $r$ .

Figure 5.7 shows that the maximal radial moment is in the ice-pile interface. Therefore, it is clear that the failure will occur either along the ice-pile interface or in the ice in the vicinity of the interface.

Table 5.4. Values for the parameters used to estimate bending moments.

Symbol	Description	Value
$R$	pile radius	0.05 m
$h_{ice}$	ice thickness	0.5 m
$\rho$	sea water density	1024 kg/m <sup>3</sup>
$E$	Young's modulus	2.38 GPa
$\nu$	Poisson's ration	0.3
$\sigma_f$	Flexural strength of ice	200 kPa

The maximum moment is related to the maximal stress in the ice plate (equal to the tension stress on the plate surface)

$$M_{\max} = \sigma_{\max} \cdot h_{ice}^2 / 6, \quad (5.10)$$

where  $\sigma_{\max}$  is the failure stress in the ice plate, which is the lowest between the flexural strength of ice  $\sigma_f$  and the adhesion strength. Using solution Eq. (5.6) with boundary conditions Eqs. (5.7)-(5.8), and combining Eq. (5.9) with Eq. (5.10), we obtain the solution for the vertical force  $F$ .



Figure 5.8 shows the uplifting force acting on the pile versus the pile radius for three ice thicknesses ( $h_{ice}$ ): 0.3 m, 0.5 m and 0.8 m. Here, we assumed that failure occurs in the ice in the vicinity of the ice-pile interface. The values obtained for the uplifting force are lower than the values measured in our field test. The possible reason for the discrepancy is the wrong choice of the values for the maximal failure stress ( $\sigma_{max}$ ) and/or Young's modulus ( $E$ ).

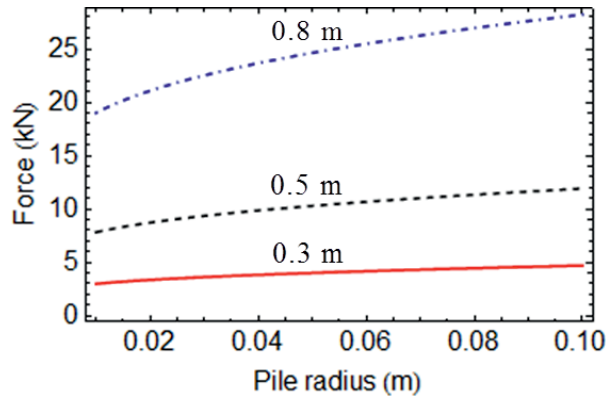


Figure 5.8. Uplifting force on the pile at the initial failure at the ice-pile interface versus the pile radius for three ice thicknesses ( $h_{ice}$ ): 0.3 m, 0.5 m and 0.8 m.

The corresponding deflections of the ice plate near the ice-pile interface are shown in Figure 5.9. The values obtained for the pile displacement before the relative sliding begin have a similar order of magnitude to the values measured in the field tests.

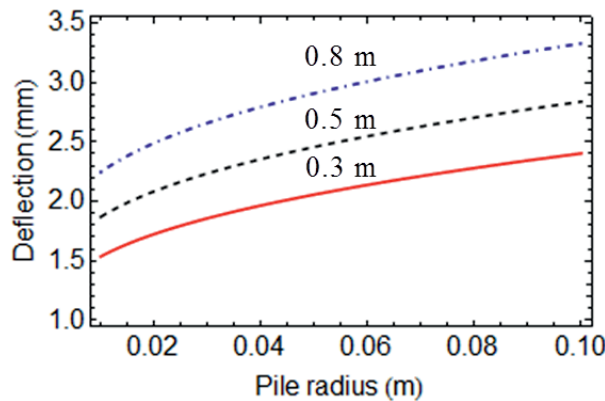


Figure 5.9. Deflection of the ice plate at the failure initiated at the ice-pile interface versus pile radius for three ice thicknesses ( $h_{ice}$ ): 0.3 m, 0.5 m and 0.8 m.

#### 5.4 Concluding remarks

Several field tests were performed to study the vertical forces exerted due to water level change on isolated ice piles frozen into the level ice. It was found that the adhesion strength in shear between the ice and the pile with a corroded steel surface was significantly higher than in tests with coated steel piles and aluminium piles.

Elastic plate theory was used to estimate the uplifting forces acting on the pile due to changes in the water level. The calculations of the uplifting forces were somewhat simplified. We did not take into account variations of the Young's modulus across the level ice thickness, and the viscous behaviour of the ice was neglected.

In cold regions where significant tidal variation takes place, ice accretes around the piles and on the vertical walls (Figure 5.1).



Figure 5.10. Ice accretion on the vertical piles (left) and vertical walls (right).

Løset and Marchenko (2009) studied the formation of ice bustles on vertical piles and concluded that their formation relates to the difference in heat conductivity of the pile and the water and the cooling of the piles below the temperature of the surrounding water. The thickness of the ice formations accreted on the piles and vertical wall surfaces is higher than the thickness of the surrounding level ice. The diameter of the ice bustles can be significantly larger than the diameter of the pile itself, leading to higher vertical and horizontal loads. A freeze bond may form between the ice bustle and the surrounding level sea ice. If the water level is changed, the freeze bond strength determines the maximal force that acts on the pile. In the areas with very small tides or without them, the ice formed around the vertical pile also does not have homogeneous thickness. Due to differences in the thermal conductivity of the pile and the water, an ice cone will be formed around the pile (Matskevitch and Shkhinek, 1992). Therefore, if the water level changes, it is likely that the maximum force will act on the pile when the ice reaches its bending strength at a certain distance from the pile's surface.

We believe that more data from field tests and further modelling are needed to increase our knowledge about this phenomenon.

# Chapter 6

## 6 Conclusions and recommendations for further work

The thesis presents the results of ice friction studies in the field and in small-scale laboratory tests. In addition, the field tests were performed to study the vertical ice forces exerted on isolated piles frozen in the level sea ice. Therefore, the work can be divided into three parts.

The first part presents new data and analysis of the coefficient of friction of first year sea ice sliding against itself and against corroded steel under field conditions in the Barents Sea and the fjords of Spitsbergen.

The second part is devoted to a small-scale laboratory study on the ‘geometrical’ stick-slip interaction between ice and stainless steel. The main focus here was to study the effect of the steel surface roughness on the ice-steel interaction.

The third part presents the results and analysis of the field experiments of the vertical ice forces exerted on isolated vertical piles frozen in the level sea ice due to water level changes. Elastic plate theory is used for the theoretical calculation of the maximum vertical force exerted on the piles.

The major conclusions and recommendations for further work are given below for each part separately.

### 6.1 Field tests on the friction of sea ice against sea ice and steel

#### Conclusions

A number of field tests were performed on the friction of sea ice against sea ice. The effects of the sliding velocity, air and ice track temperatures, normal load, presence of sea water in the interface, and ice grain orientation with respect to the sliding direction on the friction coefficient are highlighted. The findings can be summarised as follows:

- 1) Ice surface roughness is an important parameter that determines the value of the friction coefficient. Repeated sliding over the same track led to surface polishing and consequently reduced roughness, thus decreasing the kinetic friction coefficient from 0.48 to 0.05 in the most extreme case.
- 2) The velocity dependence of the kinetic friction coefficient predicted by the existing friction models does not work when sliding occurs between natural ice surfaces. In this case, the friction coefficient was found to be independent of the sliding velocity ( $6 \text{ mm s}^{-1}$  to  $105 \text{ mm s}^{-1}$ ). As the contacting surfaces became smoother, the kinetic friction coefficient started to depend on the velocity, as predicted by existing ice friction models.

- 3) The frictional force (both static and dynamic) was linearly related to the normal load.
- 4) The presence of sea water in the sliding interface has very little effect on the static and kinetic friction coefficients.
- 5) The static friction coefficient increases logarithmically with the hold time, from approximately 0.6 at 5 s to 1.26 at 960 s.

The possible implications of this work are as follows:

- The data can be used to calculate ice loads on offshore structures and to model ridge build-up and rafting processes.
- The field and full-scale data should be of value for the calibration and validation of friction models necessary for engineering applications.

#### *Recommendations for further work*

One of the main directions for improving current work is the development of a friction model that adequately describes the dependences observed in field conditions. Such a model will be of use to engineers and scientists in modelling ice-ice and ice-structure interaction.

More careful study should be performed on the dependence of the friction coefficient on the run number. The surface roughnesses of the sliding block and ice track should be measured after each run, and the correlation between the friction coefficient values and the surface roughness should be checked.

The real contact area and contact spot distribution should be measured. Tactile sensors may be used for this purpose.

There are a number of potential improvements in the setup that will lead to improvements in the field data quality. Some of these are listed below:

- To study stick-slip during field tests and for more precise measurements of the static friction coefficient, an acquisition system with a sampling frequency up to 1 kHz should be used.
- The acceleration and instantaneous velocity of the ice block should be measured during the initiation of the sliding and its stopping. It could be performed using an accelerometer installed on the top of the sliding ice block.
- A new setup should be designed to study the ice friction on very rough natural surfaces of first-year and multi-year sea ice.
- Tests on an inclined plane can be used to study static and kinetic friction first in the laboratory and then in the field.

## 6.2 Geometrical stick-slip between ice and steel

### Conclusions

New small-scale laboratory tests on ice-steel sliding were performed. Both freshwater ice and salty ice were used in the tests. The main results can be summarised as follows.

- Stick-slip was always observed in samples Mr, Hr and NHr, which had intermediate roughnesses (their arithmetic roughness  $R_a$  ranged between 2  $\mu\text{m}$  and 15  $\mu\text{m}$ ). Both steady-state sliding and stick-slip were observed in the tests performed on samples Sr and TBr, which showed the lowest ( $R_a = 0.31 \mu\text{m}$ ) and highest ( $R_a = 25.2 \mu\text{m}$ ) roughnesses, respectively.
- The relative piston-ice/ice-cylinder displacement, corresponding to one period of the load oscillations in the tests performed at a constant displacement rate, was found to be equal to the mean pitch profile  $S_m$  in all samples except Sr. The displacements remained the same in the tests performed at different displacement rates ranging between  $0.83 \times 10^{-5} \text{ m s}^{-1}$  and  $0.83 \times 10^{-3} \text{ m s}^{-1}$ .
- The ice surfaces of samples Mr and Hr after testing were covered by asperities that were similar in shape to those of the inner cylinder surfaces. These results revealed the existence of elastic deformations in the ice asperities when they moved relatively to the steel surface asperities.
- The loads measured in the experiments using fresh water ice samples were significantly higher than those measured in the experiments using saline ice samples ( $16.1 \pm 1.5 \text{ ppt}$ ).
- The upper limit of ice pressure concentration on the steel surface estimated from the tests was approximately 239 MP

The results of this work and further investigations may be useful in achieving increased understanding of ice-induced vibrations..

### Recommendations for further work

The current work can be greatly extended and improved to better understand the processes occurring during ice-steel interaction. The main proposals for future work on this topic are listed below:

- One of the results from this work is that freshwater ice and saline ice interact with steel in a similar qualitative manner. Therefore, it is recommended to use only fresh water ice in future tests to exclude the more complex effects of salt;
- An ice surface having surface asperities similar to the asperities on the inner cylinder surface should be characterised in terms of roughness. The replica of the ice surface will give necessary information.

- Measurements of the normal load in the ice-steel interface would make it possible to calculate the friction coefficient.
- Measurements of the temperature in the ice-steel interface during sliding will be beneficial for better understanding of the processes occurring during the interaction.
- Samples made of other construction materials, coatings, roughness, dimensions and geometries may be of interest to study.

### **6.3 Vertical action on a pile frozen in the level sea ice due to water level changes**

#### Conclusions

The work performed in this part can be extended to increase our knowledge of the studied phenomenon. The major results from this study are listed below:

- The maximal vertical force exerted on the pile frozen in the ice due to water level change is limited either by the adhesion strength between the ice and the pile or by the flexural strength of ice in the vicinity of the ice-pile interface. In the tests we observed, that the failure occurred on the ice-pile interface.
- The adhesion strength between the ice and the pile with a corroded steel surface was higher than between the ice and coated steel or between the ice and the aluminium pile.
- The time the pile was allowed to freeze in the level ice affected the maximum vertical load. We believe that this difference is related to the brine drainage in the ice formed from the sea ice in the space between the pile and the surrounding level ice.
- The vertical ice force calculated using elastic plate theory predicts a lower value than the one obtained in the tests. The reason for the discrepancy might be the simplifications made in the calculations (constant Young's modulus across the ice thickness) and the choice of value for the maximal stress that leads to the ice-pile bond failure.

#### Recommendations for further work

There are many opportunities and for future work and further questions that could and should be studied. The main points are listed below:

- More detailed experimental field and laboratory studies should be performed. The effect of the radius, material and shape of the pile surface should be studied.
- Artificial surface roughness with a helical shape, similar to the roughnesses produced on the piston and cylinder surfaces in our lab tests (Chapter 4), could be created on the pile surface. The effect of the surface roughness on the

maximal vertical force should be studied. It will be interesting to compare the results of such experiments with the results obtained in the laboratory.

- In the field tests, the pile can be pushed downwards at a constant rate, and the effect of the rate can be studied.
- Tests with a constant pushing normal load will be of benefit.
- Similar tests can be performed with piles surrounded by ice bustles.
- For the theoretical calculation of the ice forces acting on a pile, the viscous properties of ice and the variation of the Young's modulus across the ice thickness should be taken into account.





---

## References

- 19906, I.F., 2010. Petroleum and natural gas industries - Arctic offshore structures. ISO, Geneva, pp. 465.
- Akkok, M., Ettles, C.M.M. and Calabrese, S.J., 1987. Parameters affecting the kinetic friction of ice. *Journal of Tribology*, 109(3): 552-561.
- Barnes, P., Tabor, D. and Walker, J., 1971. The friction and creep of polycrystalline ice. *Proceedings of the Royal Society of London. A. Mathematical and Physical Sciences*, 324(1557): 127-155.
- Bäurle, L., 2006. Sliding friction of polyethylene on snow and ice, Swiss Federal Institute of Technology Zurich, 107 pp.
- Baurle, L., Kaempfer, T.U., Szabo, D. and Spencer, N.D., 2007. Sliding friction of polyethylene on snow and ice: Contact area and modeling. *Cold Regions Science and Technology*, 47(3): 276-289.
- Bowden, F. and Hughes, T., 1939. The mechanism of sliding on ice and snow. *Proceedings of the Royal Society of London. Series A. Mathematical and Physical Sciences*, 172(949): 280-298.
- Bowden, F.P. and Tabor, D., 2001. *The friction and lubrication of solids*, 1. Oxford University Press.
- Butkovich, T.R., 1958. Hardness of single ice crystals. *American Mineralogist*, 43(1-2): 48-57.
- Calabrese, S.J., Buxton, R. and Marsh, G., 1980. Frictional characteristics of materials sliding against ice. *Lubrication Engineering*, 36(5): 283-289.
- Christensen, F.T., 1986. Interaction between floating ice sheets and vertical structures due to water level fluctuations, Technical university of Denmark, Lyngby, 246 pp.
- Croasdale, K. and Cammaert, A., 1994. An improved method for the calculation of ice loads on sloping structures in first-year ice. *Power Technology and Engineering*, 28(3): 174-179.
- Dieterich, J.H., 1978. Time-dependent friction and the mechanics of stick-slip. *Pure and applied geophysics*, 116(4): 790-806.
- Dowson, D., 1998. *History of tribology*. Wiley.
- Evans, D.C.B., Nye, J.F. and Cheeseman, K.J., 1976. The kinetic friction of ice. *Proceedings of the Royal Society of London, Series A (Mathematical and Physical Sciences)*, 347(1651): 493-512.
- Forland, K.A. and Tatinclaux, J.C.P., 1985. Kinetic friction coefficient of ice. CRREL Report 85-6, CRREL, Hanover, N.H., United States.
- Fortt, A.L. and Schulson, E.M., 2007. The resistance to sliding along Coulombic shear faults in ice. *Acta Materialia*, 55(7): 2253-2264.

## References

---

- Fortt, A.L. and Schulson, E.M., 2009. Velocity-dependent friction on Coulombic shear faults in ice. *Acta Materialia*, 57(15): 4382-90.
- Fortt, A.L. and Schulson, E.M., 2011. Frictional sliding across Coulombic faults in first-year sea ice: A comparison with freshwater ice. *Journal of Geophysical Research C: Oceans*, 116(11).
- Frederking, R. and Barker, A., 2002. Friction of Sea Ice on Steel for Condition of Varying Speeds, Proceedings of the 12th International Offshore and Polar Engineering Conference., Kitakyushu, Japan, pp. 766-771.
- Gagnon, R., 2008. Analysis of data from bergy bit impacts using a novel hull-mounted external Impact Panel. *Cold Regions Science and Technology*, 52(1): 50-66.
- Gavrilo, V.P., 1984. Frictional characteristics of sea ice. In: L.P. Timokhov (Editor), *Dynamics of ice cover*. Balkema (Russian Translations Series 25), pp. 111-117.
- Goldshtein, R.V. and Epifanov, E.V., 2012. Adhesive strength of glaze-ice accretion on elements of metal structures. *Vestnik NGU. Series: Mathematics, mechanic, informatics*, 12(4): 22-40 (in russian).
- Gu, J.C., Rice, J.R., Ruina, A.L. and Tse, S.T., 1984. Slip motion and stability of a single degree of freedom elastic system with rate and state dependent friction. *Journal of the Mechanics and Physics of Solids*, 32(3): 167-196.
- Haehnel, R.B. and Mulherin, N.D., 1998. The bond strength of an ice–solid interface loaded in shear., *Ice in Surface Waters*, Proceedings of the 14th International Symposium on Ice, Potsdam, New York, USA, pp. 597-604.
- Hatton, D.C., Sammonds, P.R. and Feltham, D.L., 2009. Ice internal friction: Standard theoretical perspectives on friction codified, adapted for the unusual rheology of ice, and unified. *Philosophical Magazine*, 89(31): 2771-2799.
- Hobbs, P.V., 2010. *Ice physics*. Oxford University Press, Oxford New York.
- Hopkins, M.A., Hibler, W.D. and Flato, G.M., 1991. On the numerical simulation of the sea ice ridging process. *Journal of Geophysical Research: Oceans*, 96(C3): 4809-4820.
- Hopkins, M.A. and Tuhkuri, J., 1999. Compression of floating ice fields. *Journal of Geophysical Research*, 104(C7): 15815-25.
- Ionov, B.P. and Gramuzov, E.M., 2001. *Ships propulsion in the ice (Ledovaya hodkost' sudov)*. Sudostroenie, St.-Petersburg.
- Johnston, M.E., Croasdale, K.R. and Jordaan, I.J., 1998. Localized pressures during ice–structure interaction: relevance to design criteria. *Cold Regions Science and Technology*, 27(2): 105-117.
- Jordaan, I.J., 2001. Mechanics of ice–structure interaction. *Engineering Fracture Mechanics*, 68(17–18): 1923-1960.
- Karulina, M., Karulin, E. and Marchenko, A., 2013. Field investigations of first year ice mechanical properties in north-west Barents sea, Proceedings of the 22nd International Conference on Port and Ocean Engineering under Arctic Conditions, Espoo, Finland, pp. POAC13-049.

## References

---

- Kennedy, F.E., Schulson, E.M. and Jones, D.E., 2000. The friction of ice on ice at low sliding velocities. *Philosophical Magazine A: Physics of Condensed Matter, Structure, Defects and Mechanical Properties*, 80(5): 1093-1110.
- Kerr, A., 1975. Ice forces on structures due to a change of the water level, *Proceedings of the 3rd IAHR International Symposium on Ice*, pp. 419-427.
- Kerr, A.D., 1985. Analysis of floating ice covers with partial flooding. *Cold Regions Science and Technology*, 10(2): 117-123.
- Kietzig, A.-M., Hatzikiriakos, S.G. and Englezos, P., 2010. Physics of ice friction. *Journal of Applied Physics*, 107(8).
- Kietzig, A.M., Hatzikiriakos, S.G. and Englezos, P., 2009. Ice friction: the effects of surface roughness, structure, and hydrophobicity. *Journal of Applied Physics*, 106(2): 024303 (7 pp.).
- Kim, E., Golding, N., Schulson, E.M., Løset, S. and Renshaw, C.E., 2012. Mechanisms governing failure of ice beneath a spherically-shaped indenter. *Cold Regions Science and Technology*, 78(0): 46-63.
- Kragelsky, I.V., 1968. *Friction and Wear*. Mashinostroenie, Moskva.
- Landau, L.D. and Lifshitz, E.M., 1987. *Theory of elasticity*. Moskva "Nauka", 248 pp.
- Lishman, B. and Sammonds, P., 2013. Memory in sea ice friction, *Proceedings of the 22nd International Conference on Port and Ocean Engineering under Arctic Conditions*, Espo, Finland.
- Lishman, B., Sammonds, P. and Feltham, D., 2011. A rate and state friction law for saline ice. *Journal of Geophysical Research*, 116(C5).
- Lishman, B., Sammonds, P., Feltham, D. and Wilchinsky, A., 2009. The rate- and state-dependence of sea ice friction, *Proceedings of the 20th International Conference on Port and Ocean Engineering under Arctic Conditions*, Lulea, Sweden, pp. POAC09-66.
- Lishman, B., Sammonds, P.R. and Feltham, D.L., 2013. Critical slip and time dependence in sea ice friction. *Cold Regions Science and Technology*, 90–91(0): 9-13.
- Liukkonen, S., 1988. Friction panel, measurements in full-scale and model-scale icebreaking thip tests, *Proceedings of the 7th International Conference on Offshore Mechanics and Arctic Engineering*. American Society of Mechanical Engineers, Houston, USA, pp. 255-262.
- Liukkonen, S., 1992. Theoretical approach to physical modelling of kinetic friction between ice and ship, *Proceedings of the 11th International Conference on Offshore Mechanics and Arctic Engineering*. American Society of Mechanical Engineers, pp. 213-213.
- Løset, S. and Marchenko, A., 2009. Field studies and numerical simulations of ice bustles on vertical piles. *Cold Regions Science and Technology*, 58(1–2): 15-28.
- Løset, S., Shkhinek, K.N., Gudmestad, O.T. and Høyland, K.V., 2006. *Actions from ice on Arctic Offshore and Coastal Structures*. LAN, St. Petersburg, 272 pp.

## References

---

- Maeno, N., 1988. Science of ice. "Mir", Moskva, 231 pp.
- Maeno, N. and Arakawa, M., 2004. Adhesion shear theory of ice friction at low sliding velocities, combined with ice sintering. *Journal of Applied Physics*, 95(1): 134-9.
- Maeno, N., Arakawa, M., Yasutome, A., Mizukami, N. and Kanazawa, S., 2003. Ice-ice friction measurements, and water lubrication and adhesion-shear mechanisms. *Canadian Journal of Physics*, 81(1-2): 241-249.
- Makkonen, L., 2012. A thermodynamic model of sliding friction. *AIP Advances*, 2(1): 012179-9.
- Makkonen, L. and Tikanmaki, M., 2013. Modelling the friction of ice. *Cold Regions Science and Technology*: submitted.
- Marchenko, A. and Makshtas, A., 2005. A dynamic model of ice ridge buildup. *Cold Regions Science and Technology*, 41(3): 175-188.
- Marmo, B.A., Blackford, J.R. and Jeffree, C.E., 2005. Ice friction, wear features and their dependence on sliding velocity and temperature. *Journal of Glaciology*, 51(174): 391-398.
- Matskevitch, D.G. and Shkhinek, K.N., 1992. Ice Action onto Multilegged Structures Due to Change of Water Level. *International Journal of Offshore and Polar Engineering*, 2(3): 222-227.
- Nakazawa, N., Terashima, T., Saeki, H. and Ono, T., 1993. Factors influencing the coefficient of friction between sea ice and various materials, *Proceedings of the 12th International conference on Port and Ocean Engineering under Arctic Conditions, Hamburg*, pp. 97-105.
- Nanetti, M., Marchenko, A. and Høyland, K.V., 2008. Experimental study on friction between saline ice and steel, *Proceedings of the 19th IAHR International Symposium on Ice, Vancouver, British Columbia, Canada*, pp. 1131-1146.
- Oksanen, P., 1983. Friction and adhesion of ice. 12350621.
- Oksanen, P. and Keinonen, J., 1982. Mechanism of friction of ice. *Wear*, 78(3): 315-324.
- Olsson, H., Åström, K.J., Canudas de Wit, C., Gäfvert, M. and Lischinsky, P., 1998. Friction models and friction compensation. *European journal of control*, 4: 176-195.
- Paavilainen, J., Tuhkuri, J. and Polojärvi, A., 2011. 2D numerical simulations of ice rubble formation process against an inclined structure. *Cold Regions Science and Technology*, 68(1-2): 20-34.
- Palmer, A. and Croasdale, K., 2013. Arctic offhosre engineering. World Scientific Publishing Co. Pte. Ltd., Singapore.
- Persson, B.N.J., 2000. Sliding friction: Physical Principles and Applications. Springer-Verlag Berlin Heidelberg New York.

## References

---

- Polojärvi, A. and Tuhkuri, J., 2013. On modeling cohesive ridge keel punch through tests with a combined finite-discrete element method. *Cold Regions Science and Technology*, 85(0): 191-205.
- Popov, V.L., 2010. *Contact mechanics and friction: physical principles and applications*. Springer.
- Pritchard, R.S., Knoke, G.S. and Echert, D.C.S., 2012. Sliding friction of sea ice blocks. *Cold Regions Science and Technology*, 76-77: 8-16.
- Rabinowicz, E., 1995. *Friction and wear of materials*. Wiley-Interscience.
- Repetto-Llamazares, A.H.V., Høyland, K.V. and Kim, E., 2011. Experimental studies on shear failure of freeze-bonds in saline ice:: Part II: Ice-ice friction after failure and failure energy. *Cold Regions Science and Technology*, 65(3): 298-307.
- Rist, M.A., 1997. High-Stress Ice Fracture and Friction. *The Journal of Physical Chemistry B*, 101(32): 6263-6266.
- Ruina, A., 1983. Slip instability and state variable friction laws. *Journal of Geophysical Research*, 88(10): 359-10.
- Ryvlin, A.Y., 1973. Experimental study of ice friction. *Proceedings of the Arctic and Antarctic Research Institute*, 309: 186-199.
- Saeki, H., Ono, T., Nakazawa, N., Sakai, M. and Tanaka, S., 1986. Coefficient of friction between sea ice and various materials used in offshore structures. *Journal of Energy Resources Technology, Transactions of the ASME*, 108(1): 65-71.
- Sammonds, P., Hatton, D., Feltham, D. and Taylor, P., 2005. Experimental study of sliding friction and stick-slip on faults in floating ice sheets, *Proceedings of the 18th International Conference on Port and Ocean Engineering under Arctic Conditions*, pp. 303-312.
- Sammonds, P.R., Murrell, S.A.F. and Rist, M.A., 1998. Fracture of multiyear sea ice. *Journal of Geophysical Research C: Oceans*, 103(C10): 21,795-21,815.
- Schulson, E.M. and Duval, P., 2009. *Creep and fracture of ice*. Cambridge University Press, Cambridge, UK, New York;
- Schulson, E.M. and Fortt, A.L., 2012. Friction of ice on ice. *Journal of Geophysical Research: Solid Earth*, 117(B12): B12204.
- Schulson, E.M. and Fortt, A.L., 2013. Static strengthening of frictional surfaces of ice. *Acta Materialia*, 61(5): 1616-1623.
- Sodhi, D.S., 2001. Crushing failure during ice-structure interaction. *Engineering Fracture Mechanics*, 68(17-18): 1889-1921.
- Squire, V.A., Hosking, R.J., Kerr, A.D. and Langhorne, P.J., 1996. *Moving loads on ice plates. Solid mechanics and its applications*, 45. Kluwer Academic Pub, The Netherlands.

## References

---

- Sukhorukov, S., Määttänen, M. and Løset, S., 2012. Field experiments on the friction coefficient of sea ice on sea ice, Proceedings of the 21st IAHR International symposium on ice, Dalian, China, pp. 65-77.
- Tabata, T. and Tusima, K., 1981. Friction Measurements of Sea Ice on some Plastics and Coatings, The Sixth International Conference on Port and Ocean Engineering under Arctic Conditions, Quebec, Canada, pp. 526-535.
- Tabor, D., 1959. Junction Growth in Metallic Friction: The Role of Combined Stresses and Surface Contamination. Proceedings of the Royal Society of London. Series A, Mathematical and Physical Sciences, 251(1266): 378-393.
- Tatinclaux, J.C., 1989. Effect of normal pressure on kinetic friction coefficient: myth or reality?, Proceedings of the 22nd American Towing Tank Conference, St. John's, Newfoundland, pp. 127-134.
- Tatinclaux, J.C. and Murdey, D., 1985. Field tests of the kinetic friction coefficient of sea ice. CRREL Report 85-17, Hanover, N.H., United States.
- Terashima, T., Nakazawa, N., Kioka, S., Usami, N. and Saeki, H., 2006. Vertical Ice Forces on Pile Structures Under Water Level Changes, Proceedings of the 18th IAHR International Symposium on Ice Sapporo, Japan, pp. 145-152.
- Tikanmäki, M., Makkonen, L. and Kurkela, J., 2011. Friction modelling in ice crushing simulation, Proceedings of the 21st International Conference on Port and Ocean Engineering under Arctic Conditions, Montreal, Canada.
- Timco, G.W. and Frederking, R.M.W., 1995. Experimental Investigations of the Behavior of Ice at the Contact Zone. In: A.P.S. Selvadurai and M.J. Boulon (Editors), Studies in Applied Mechanics. Elsevier, pp. 35-55.
- Timco, G.W. and Weeks, W.F., 2010. A review of the engineering properties of sea ice. Cold Regions Science and Technology, 60(2): 107-129.
- Timoshenko, S. and Woinowsky-Krieger, S., 1959. Theory of plates and shells. McGraw-Hill, New York.
- Tryde, P., 1983. Report on vertical ice lifting of piles in a number of Danish marinas with a description of the lifting mechanism, Proceedings of the 7th International Conference on Port and Ocean Engineering under Arctic Conditions, Helsinki, Finland, pp. 920-929.
- Tusima, K. and Tabata, T., 1979. Friction measurements of sea ice on flat plates of metals, plastics and coatings, Proceedings of the 5th International Conference on Port and Ocean Engineering under Arctic Conditions, Trondheim, Norway, pp. 741-755.
- Valanto, P., 2001. The Resistance of Ships in Level Ice. SNAME Transactions, 109: 53-83.
- Weeks, W.F., 2010. On sea ice. University of Alaska Press, Fairbanks, Alaska, 664 pp.
- Zabilansky, L.J., 1985. Real-time measurements of uplifting ice forces, Proceedings of the 31st International Instrumentation Symposium. Instrument Society of America (ISA), San Diego, California, pp. 253-259.